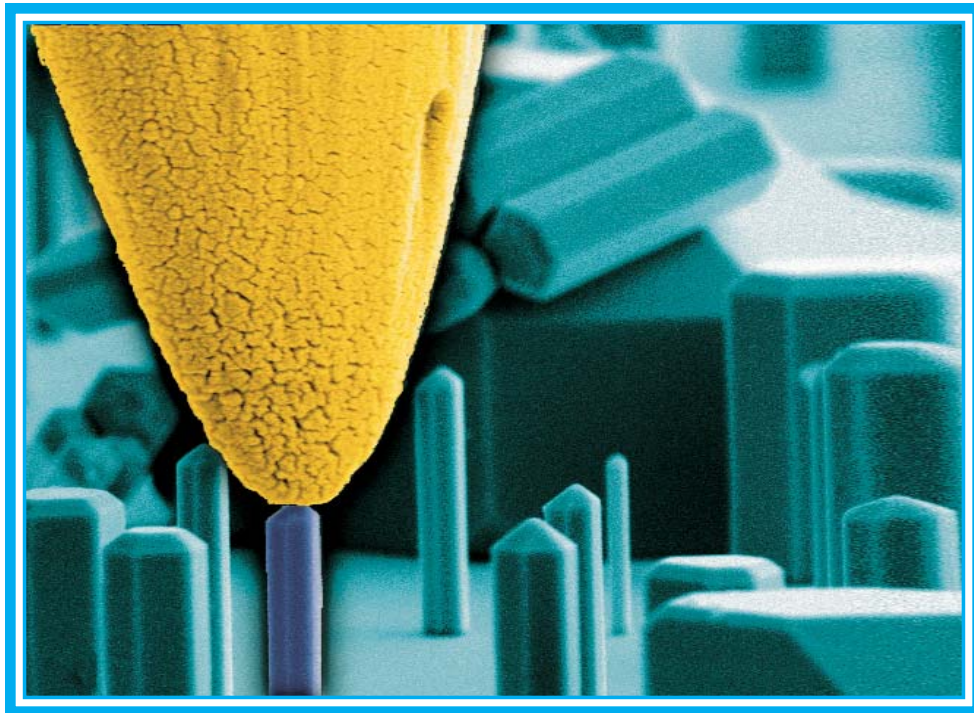*Physical, Chemical, and Nano Sciences Center*

# Research Briefs

*2007*

**Sandia National Laboratories**
**Albuquerque, New Mexico**

*A Multiprogram Laboratory*

**Cover Page:  "False-colored SEM image of a gold-coated tungsten probe contacting a GaN rod for electrical characterization.  Each rod can be individually addressed."  (See page 33.)**

# Message from the Director

The Physical, Chemical, and Nano Sciences Center creates new scientific knowledge in support of Sandia's mission areas – nuclear weapons; energy, resources, and nonproliferation; defense systems and assessments; and homeland security and defense. We provide science-based solutions in support of Sandia's broad national security mission. We also perform focused long-term research in areas that are most likely to have impact on future Sandia missions and national security, particularly in the physical, chemical, and nano sciences. This volume highlights representative research in our areas of emphasis, including Science for Sandia's National Security Mission [including the Qualification Alternatives to the Sandia Pulsed Reactor (QASPR) Program]; Nanoscience and Nanotechnology [including the Center for Integrated Nanotechnologies (CINT)]; Compound Semiconductor Materials and Devices, with special emphasis on Nitride Semiconductors; and a sampling of our other work in the Physical and Chemical Sciences.

The activities of the Physical, Chemical, and Nano Sciences Center are supported by a diverse set of funding sources that reflect the broad impact of our work, both scientifically and programmatically. The research described in this volume illustrates the importance of a strong science base in the physical, chemical, and nano sciences for the success of the Department of Energy's missions. Throughout this work, we have benefited immeasurably from our partnerships with colleagues across the labs, in universities, and in industry. We gratefully acknowledge their collaboration.

We appreciate your interest in our work and welcome your comments and inquiries.

**Julia M. Phillips**
*Director*

# Table of Contents

## Science for Sandia's National Security Mission

## Nanoscience and Nanotechnology

# Table of Contents Cont'd

## Compound Semiconductor Materials and Devices

## Physical and Chemical Sciences

# Table of Contents Cont'd

# Science for Sandia's National Security Mission

# *Qualification Alternatives to the Sandia Pulsed Reactor (QASPR) Program  Science in Sandia's Physical, Chemical, & Nano Sciences Center (PCNSC):  Overview*

## *by* **S. M. Myers**

**M**otivation—QASPR is developing means to certify electronic systems exposed to intense bursts of MeV neutrons without using the Sandia Pulsed Reactor (SPR), which was de-commissioned in Sept. 06. Testing in still-available irradiation facilities will be combined with new, science-based modeling to predict device and circuit performance under general conditions of interest. The most immediate concern is carrier recombination at neutron dis-placement damage in Si bipolar-junction transistors (BJTs). Such carrier loss is offset by additional device currents that, in turn, reduce gain (Fig. 1).  The gain reduction is often large–from ~200 to <1 during SPR-cavity irradia-tions–and varies on the scale of microseconds to seconds after the pulse due to defect annealing.

Such science-based prediction is a challenge requiring new advances in irradiation methods, diffusion-reaction modeling, defect physics, and device characterization. These QASPR develop-ments are occurring largely within Sandia's PCNSC, and engaging a variety of experimen-tal and theoretical expertise within the Center. Recent progress is detailed in the following Briefs.

**A**ccomplishment—The Ion Beam Laboratory (IBL) within Sandia's PCNSC is currently unique in producing SPR-level defect concen-trations at multi-µm depths in pulses as short as 10 µs. Ed Bielejec and George Vizkelethy have developed new capabilities within the IBL and have performed extensive experiments charac-terizing the ion damage in Si and its influence on BJT gain.  As a result of their efforts, IBL is currently among the three primary irradiation facilities to be used in QASPR qualification procedures [along with Sandia's Annular Core Research Reactor (ACRR) for longer neutron pulses and the MEDUSA LINAC at Hill AFB, Utah, for pulsed-electron-beam ionization].

Bill Wampler and Sam Myers have developed the defect physics used in QASPR modeling based on the open literature and ongoing experimental and theoretical studies at Sandia. Sam has written a code to model defect evolution within the submicrometer recoil cascades produced by neutrons.  Further, he has developed a device-model code that Bill has used extensively to test physics and prototype qualification procedures.

Normand Modine and Alan Wright are applying density-functional theory (DFT) to fundamental defect properties needed for QASPR modeling but inaccessible to experiment, such as the band-gap levels and diffusivities of the Si self-interstitial.  Pursuant to the robust fidelity required for system qualification, they have pushed DFT to new levels of rigor and accuracy through in-depth studies of convergence.

Robert Fleming, with consultants Carl Seager and David Lang, has used deep-level transient spectroscopy (DLTS) to characterize neutron and ion damage in QASPR devices and correlate specific features with device gain degradation. Further, Robert, *et al*., have made fundamental advances in understanding the novel features of neutron damage arising from defect clustering within recoil cascades.

Bas Vaandrager has utilized construction analy-sis, secondary ion mass spectrometry (SIMS), spreading-resistance, and electron beam induced current (EBIC) to achieve device characteriza-tions sufficiently accurate to reproduce pre-irradiation device properties with slight parameter adjustments. This contrasts with the extensive empiricism typically used in device modeling but problematic for science-based treatments.
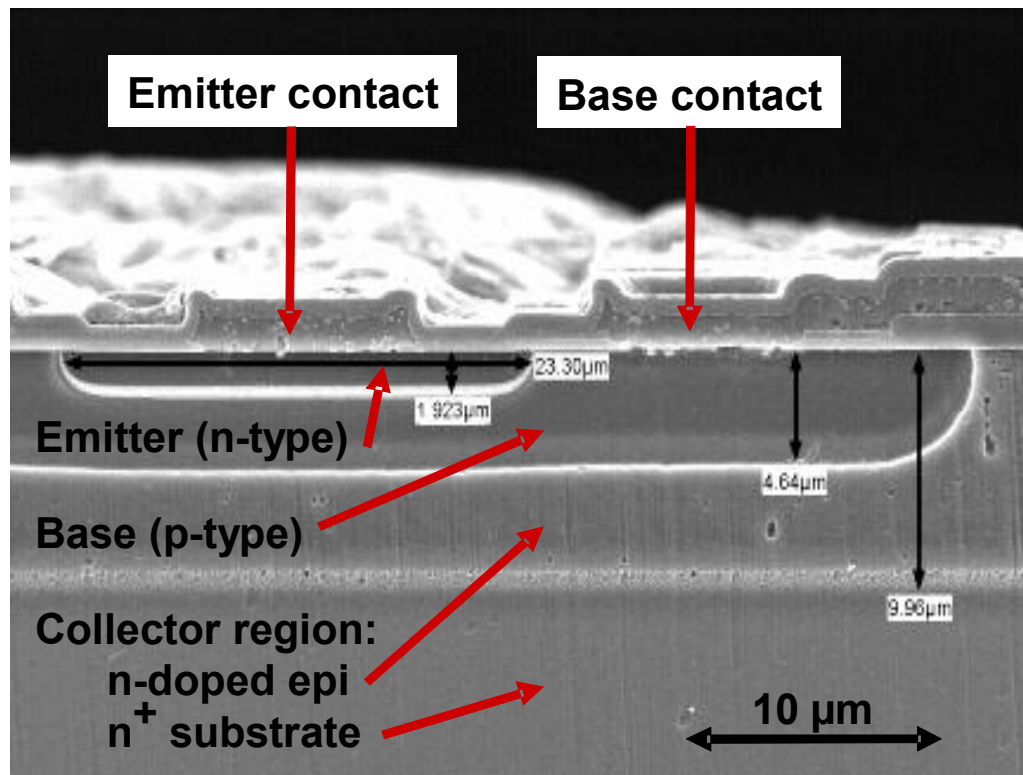
**Figure 1**. Cross-section of a vertically layered n-p-n bipolar-junction transistor (Microsemi 2N2222) used in QASPR studies of neutron-induced gain reduction. Displacement damage in the vicinity of the emitter-base junction, and secondarily in the underlying base, catalyzes carrier recombination that is offset by increased flow of conduction – electrons from the emitter and holes from the base. The resulting device currents reduce gain by more than two orders of magnitude in the case of SPR irradiation.

# Gain Changes in Silicon Bipolar Transistors Due to Atomic Displacements:  Theory and Experiment

## *by* W. R. Wampler and S. M. Myers

**M**otivation—Irradiation of semiconductor devices by energetic neutrons or ions produces vacancies and interstitials which migrate and annihilate or react to form more stable defect complexes. These defects capture electrons and holes which increase carrier recombination and decrease the gain of a bipolar junction transistor (BJT).  Thus, irradiation by a brief pulse causes a decrease in gain, which partially recovers with time after the pulse. We have developed a defect physics model to simulate these effects, which is based on known defects in silicon. This model is used in CHARON, a multi-dimensional diffusion-reaction device simulation code, to capture effects of radiation damage on device operation for the Qualification Alternatives to the Sandia Pulsed Reactor (QASPR) project.  The fidelity of the model is a central issue for QASPR, since this influences the accuracy of predictions.

**A**ccomplishment—We are undertaking model development, calibration, and validation by comparing simulations with measurements of gain versus time after a pulse for 2N2222 npn transistors irradiated with neutrons in SPRIII (Sandia Pulsed Reactor) and ACRR (Annular Core Research Reactor), and with silicon ions at the Sandia IBL (Ion Beam Laboratory). The model uses dopant profiles from secondary ion mass spectrometry (SIMS) measurements scaled to give measured gain. The calibrated model agrees closely with experiment as shown in  Fig. 1 which plots the normalized inverse gain modified to reduce nonlinear dependence on irradiation dose. The simulation shown in Fig. 1 utilizes a one dimensional device model developed by one of us (Myers) as a platform for defect physics model development which agrees with CHARON. Between one millisecond and one second, the RMS deviation between the model and SPR cavity data is less than 1%. Model calibration is necessary because many of the defect properties are known only approximately.  The parameter values (vacancy diffusivity and carrier capture cross sections) needed to achieve agreement with experiment

are within their range of uncertainty. In the model, the principle physical process causing transient gain recovery is the diffusion of vacancies and their reaction with phosphorus dopants to form the vacancy phosphorous (VP) complexes near the base emitter junction. This is consistent with the presence of VP in this region of the device observed by deep-level transient spectroscopy (DLTS). As Fig. 1 shows, the time dependence of the transient gain change is nearly the same for irradiation by neutrons or by silicon ions for which the damage peak is at the emitter base junction (4.5 MeV for the Microsemi 2N2222).  Model simulations have been compared with experiments over a broad range of conditions, including irradiation by neutrons and ions, wide ranges of damage levels and device currents, and both npn and pnp silicon BJTs. In general, the model gives the correct trends, though the extent of quantitative agreement varies and is still under investigation.

The magnitude of the gain change depends on the defect concentration. Figure 2 shows measured inverse gain change at one second after the pulse, modified to reduce non-linear dependence at high defect concentrations, plotted versus Frenkel pair concentration calculated using MARLOWE[1] and the measured irradiation doses. The modified inverse gain change varies linearly with defect concentration for each facility, but we see small offsets between the various irradiation facilities.

**S**ignificance—This work demonstrates that the device model used in QASPR can accurately simulate gain changes in silicon BJTs. This enables a critical test of the QASPR process in which the gain change from irradiation in SPR will be predicted for a device which differs from the one used in model development. This test will use the model together with measurements of transient gain change from irradiation with short ion pulses at the IBL and long time gain change from neutron irradiation in ACRR.
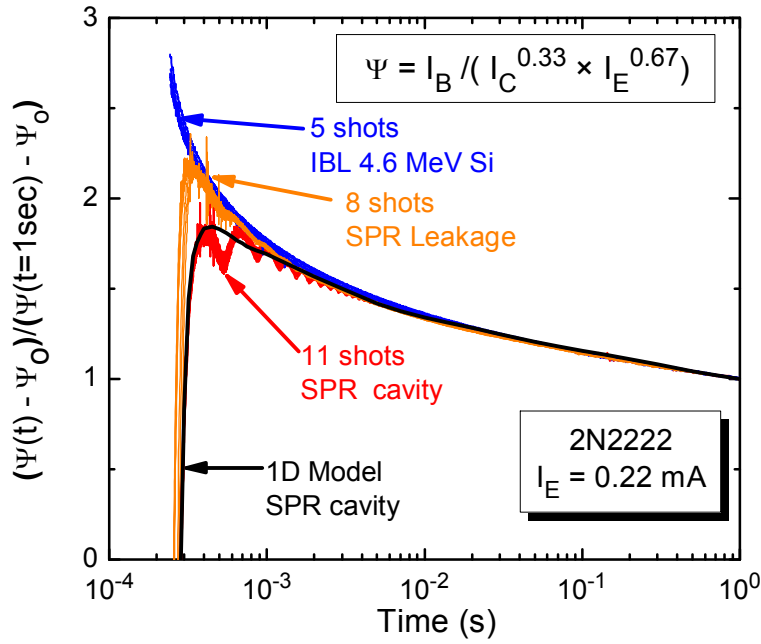
**Figure 1**. Inverse gain change normalized to the value at one second. The plotted quantity $\Psi$ includes a correction to remove nonlinear transient response at high damage mainly from the constant emitter current configuration used in the experiment. At low damage $I_C \approx I_E$ and $\Psi \approx I_B/I_C$. The calibrated model (black) agrees closely with data from neutron irradiation in SPR central cavity (red) and with data from irradiation with 4.5 MeV ions (blue). For this plot, the origin of the time scale is chosen to put the center of the pulse at 0.2 millisecond. $\Psi_o$ is the inverse gain of the device prior to irradiation.
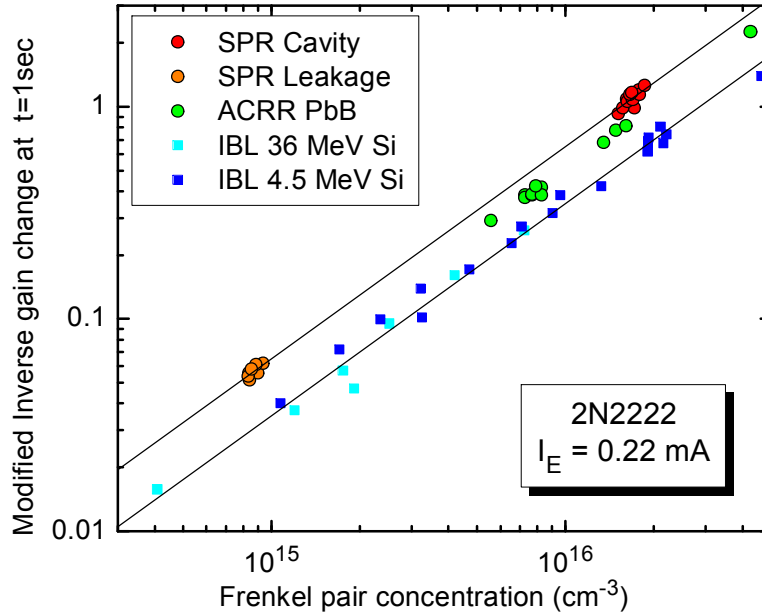


**Figure 2**. Inverse gain change one second after the pulse, modified to reduce non-linear dependence at high defect concentrations, plotted versus Frenkel pair concentration calculated using MARLOWE with measured irradiation doses. Black lines indicate linear dependence on defect concentration.

# High Precision Quantum Mechanics Calculations for Silicon Defects

## *by* A. F. Wright and N. A. Modine

**M**otivation—The QASPR (Qualification Alternatives to the Sandia Pulsed Reactor) program has the challenging task of developing a capability to accurately model gain degrada-tion and recovery in semiconductor devices following intense neutron irradiation, with the goal of using this capability to help qualify nuclear weapons. A foundational element of this modeling effort is density-functional-theory (DFT) calculations for the energy levels and migration enthalpies of the primary defects produced by the irradiation and the secondary defects produced by reactions of these defects with each other and with impurities or dopants. The importance of the QASPR program to the Laboratory motivated us to utilize Sandia's large-scale computers to overcome substantial obstacles that limited the precision of previous calculations for defects in semiconductors.

**A**ccomplishment—We developed a method for eliminating the supercell size dependences that plagued all previous DFT calculations for defects in semiconductors and applied this method to obtain high precision results for the energy levels and migration enthalpies of the two primary defects in silicon: the Si vacancy and the self-interstitial. After describing the new method, we report a few of the results obtained for the Si vacancy.

Periodic boundary conditions are widely used in DFT calculations for defects in silicon. They yield an efficient computational scheme, but also introduce spurious electrostatic and strain interactions between the defect and its periodic replicas. These interactions can influence the defect atomic configuration and formation enthalpy, and ultimately cause the results to depend on the size of the supercell. This dependence is especially pronounced for charged defects, but is also present even for neutral defects. To eliminate this dependence, we computed defect formation enthalpies in supercells containing nominally 216, 512, and 1000 atoms, and fit these results to a physically reasonable formula to obtain the formation enthalpy in an infinite sized cell corresponding to an isolated defect. We did this not only for the local energy minimum configurations (LEMCs) (see Fig. 1), but also for the saddle point configurations (SPCs) which are traversed by a migrating defect. By subtracting the LEMC value from the SPC value, we obtained the migration enthalpy. Furthermore, we obtained the electronic energy levels in the band gap from differences in the LEMC formation en-thalpies.

The configurations found for the Si vacancy LEMCs were in agreement with results from experiments, and the energy levels near the bottom of the gap were within 20 meV of the experimental results (see Fig. 2 - experimental results are not available for the two levels higher in the gap). The Si vacancy migration enthalpies were within the range of measured values except for the -1 charge state, for which there is only one measured value. (There is no measured value for the +1 charge state.)

**S**ignificance—The rigor and precision of these DFT calculations are advancing understanding of defect physics and are providing confidence in the QASPR program and its ability to serve as an alternative methodology for qualifying nuclear weapons.
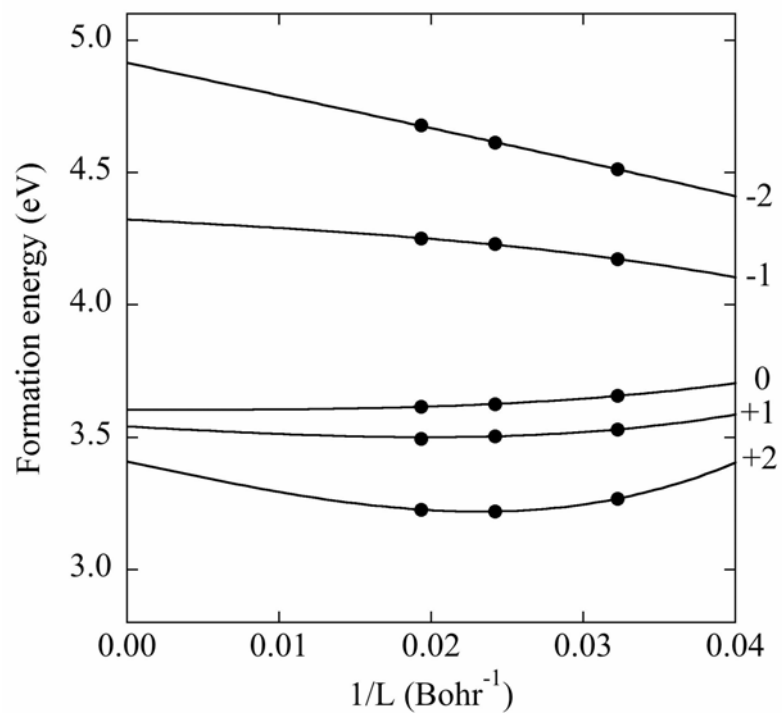
---

**Figure 1.** Plots of Si vacancy LEMC formation enthalpies versus the inverse of the length of the supercell. The filled circles are computed values, and the lines are fits.
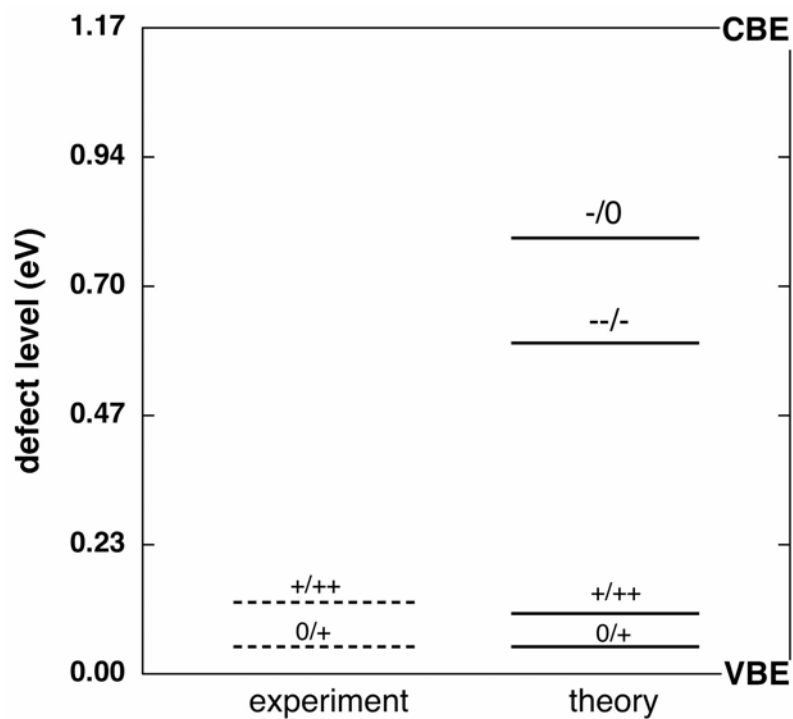


**Figure 2.** Experimental and theoretical Si vacancy energy levels.

# *Neutron and Ion Induced Defects in Silicon in a Complex Damage Environment*

## *by* R. M. Fleming

**M**otivation—The Qualification Alternatives to the Sandia Pulsed Reactor (QASPR) program seeks to build a physics-based model of neutron damage in materials that begins with an atomistic description of damage and ends with a prediction of the performance of a complex circuit. The beginning of this process is an understanding of the science of defect formation and defect reactions. We have been seeking this understanding using deep level transient spectroscopy (DLTS) measurements from npn and pnp transistors following neutron and ion irradiation. These radiation sources are known to produce damage cascades rather than uniform point defects. The challenge here is to apply knowledge from a mature field (silicon radiation defects) to a complex problem (interacting defects in damage cascades). We have found that interacting defects produce a number of unexpected phenomena including changes in the electrical characteristics of the defects and changes in defect formation chemistry.

**A**ccomplishment—Following ion and neutron irradiation we have made DLTS measurements on the collectors of npn transistors ($N_D \sim 10^{15}$ cm$^{-3}$) and the bases of pnp transistors ($N_D \sim 10^{17}$ cm$^{-3}$). We have applied a simple model[1] whereby clusters of defects raise the local energy levels of defects relative to the Fermi level and slow the rate of electron capture into these defects. We use a realistic simulation of the spatial and size distribution of these defect clusters and show that the model predictions agree very well with measurements of electron capture into the di-vacancy ($V_2$) defect between 300 and 500 K in the npn collector. Moreover, annealing studies used together with the model show that a well-known, but unexplained asymmetry in the DLTS spectrum after neutron damage in n-type silicon must result from interacting $V_2$ defects within the damage cascade. Damage cascades and asymmetric DLTS spectra occur only when the transistor are damaged by neutrons or ions at the end of range. When point defects are created uniformly (electron damage or early in the ion track), no interacting $V_2$ defects are produced. The result is symmetric DLTS spectrum with a larger vacancy oxygen (VO) defect signature.

In the highly doped pnp base, the reaction chemistry is different. All DLTS spectra are similar, regardless of whether damage cascades are present. The dominant defect is vacancy phosphorus (VP) after all types of damage.

**S**ignificance—This is the first quantitative model of band bending and slowed electron capture effect in neutron damaged silicon. The quantitative agreement of the model with the data has allowed us to prove that the large, unexplained DLTS peak near the single charge state of $V_2$ arises from the spatial region of damage cascade. The logical conclusion is that it comes from an enhanced number of $V_2$ defects located within strained regions of the lattice. These experiments are of interest to QASPR because they quantify the degree of clustering in agreement with more sophisticated QASPR models. They also show that in the transistor base, where defects directly affect the transistor gain, the dominant defect remains VP with few of the interacting $V_2$ defects.

[1] R. M. Fleming, C. H. Seager, D. V. Lang, P. J. Cooper, E. Bielejec, and J. M. Campbell, J. Appl. Phys. **102**, 043711 (2007).

---

**Contact:** Robert M. Fleming, Semiconductor Material & Device Sciences, Dept. 1123
Phone: (505) 284-8460, Fax: (505) 844-1197, E-mail: rmflemi@sandia.gov
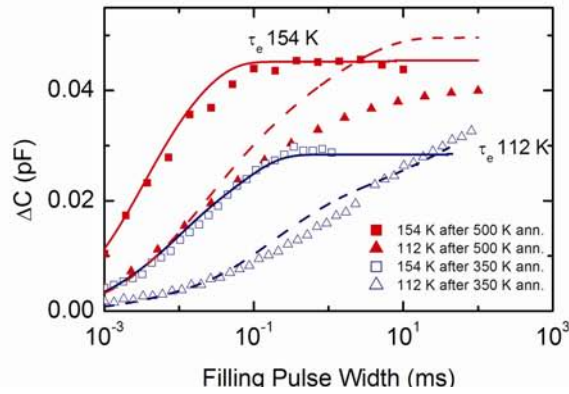
**Figure 1**. DLTS signal as a function of the filling pulse width shows a stretch out characteristic of electrostatic defect interactions and band bending. After annealing at 500K (solid symbols) there is less stretch out. Lines are fits to a model described above.
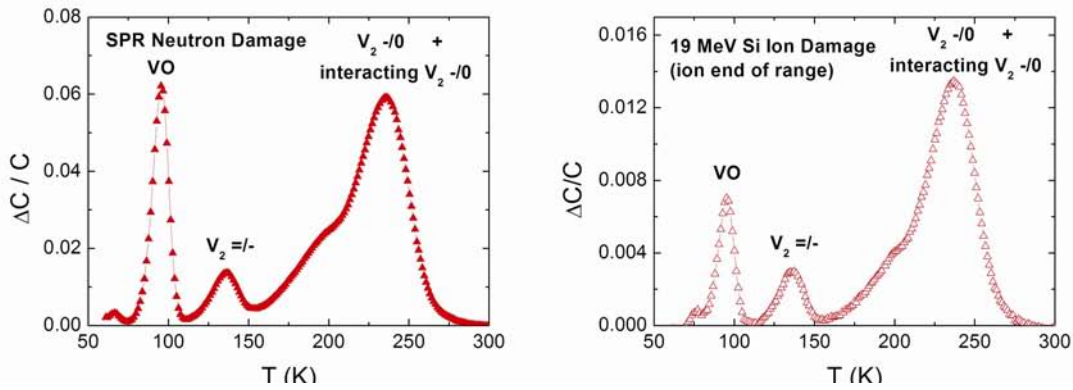


**Figure 2**. Neutrons and ions at end of range show asymmetric $V_2$ DLTS at 125 and 235K due to contributions from interaction $V_2$ defects within damage cascades.
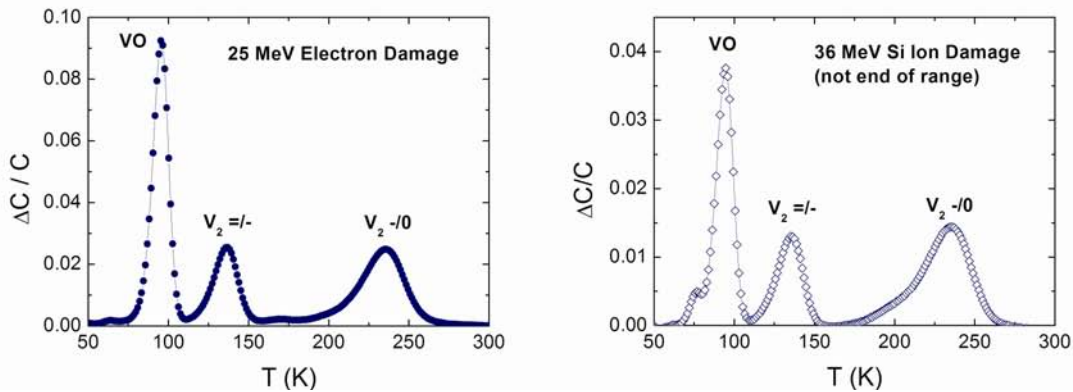


**Figure 3**. Electrons and ions before end of range show symmetric V2 DLTS and 125 and 235K and no defect clustering effects.

# *Annealing Factor as a Metric for Comparison between SPR-III and Ion Beam Laboratory (IBL)*

*by* **E. S. Bielejec, G. Vizkelethy, D. B. King, and B. L. Doyle**

**M**otivation—While the Messenger-Spratt late-time inverse gain degradation[1] is an excellent metric for late-time comparisons among the damage produced by Qualification Alternatives to the Sandia Pulsed Reactor (QASPR) program facilities, many qualification conditions require an understanding of early-time transient annealing results. The annealing factor, defined below, is one example of a metric that is used to capture the early-time transient behavior:

$$AF(t) = \frac{\dfrac{1}{G(t)} - \dfrac{1}{G_0}}{\dfrac{1}{G_\infty} - \dfrac{1}{G_0}} \ .$$

G(t) is time-varying gain measured during and immediately after the irradiation, $G_0$ is the initial gain, and $G_\infty$ is the final ASTM gain (after annealing at 80 ºC for 2 hours). The annealing factor is the ratio of damage at any time to the final stable damage population and is proportional to the effective defect density during the annealing period.

**A**ccomplishment—Here we demonstrate the ability to match the temporal profile and the damage creation rate of Sandia Pulsed Reactor (SPR-III) irradiations using the Si irradiations in the Ion Beam Laboratory (IBL). We will compare a maximum SPR cavity pulse (~4E14 n/cm$^2$) and a minimum cavity pulse (~1E14 n/cm$^2$) to comparable Si irradiations. Simulating damage creation rates of a maximum cavity SPR-III pulse requires the use of 4.5 MeV Si (directly targeting, in depth, the base-emitter

junction). We cannot produce enough damage in a single 100 µs pulse using the 36 MeV Si (uniform damage over the active region of the device) beam to match these conditions. For minimum cavity pulse irradiations we can simulate SPR-III using either the 4.5 MeV or the 36 MeV Si beams.

Figure 1 compares a maximum cavity SPR-III pulse and a 4.5 MeV Si irradiation, both with 0.22 mA emitter currents. In both cases the duration of the pulse is ~100 µs. The 4.5 MeV Si irradiation condition is chosen based on its 1 MeV silicon equivalent neutron fluence (effectively the late-time ASTM gain values of the two irradiations are the same). We plot the annealing factor as a function of time after the irradiation, shifting the time base so that the peak of the irradiation occurs at t = 0. In Fig. 2 we show a comparison between a minimum cavity SPR-III pulse and a 36 MeV Si irradiation both with 9 mA emitter current. The SPR-III pulse width is ~800 µs, and the transient annealing is masked by late-time gamma/neutron radiation from the reactor. In this example we have not shifted the time base between the two facilities. We conclude that the two facilities produce nearly identical annealing rates.

**S**ignificance—We have shown that we can match both the temporal profile and damage creation rate of SPR-III irradiations using 4.5 and 36 MeV Si shots in the IBL for both 0.22 and 9 mA emitter currents. This is critical for the long-term success of the QASPR process, as different device geometries and over-layers will require a variety of ion/energy combinations to simulate the fast burst reactor environment.

---

[1] G. C. Messenger and M. S. Ash, *The Effects of Radiation on Electronic Systems*. (Van Nostrand Reinhold, New York, 1986)

**Contact:** Edward S. Bielejec, Radiation-Solid Interactions, Dept. 1111
Phone: (505) 284-9256, Fax: (505) 844-7775, E-mail: esbiele@sandia.gov

**Figure 1**. Comparison of a 4.5 MeV Si irradiation (red) and a SPR-III maximum cavity pulse (black), where $G_0$ is the pre-irradiation gain and $G_{astm}$ is the final gain after ASTM (80 ℃ for 2 hr) anneal. This figure displays excellent agreement between the early-time transient annealing between IBL and SPR-III for times $\geq \sim$ 1E-3 s.
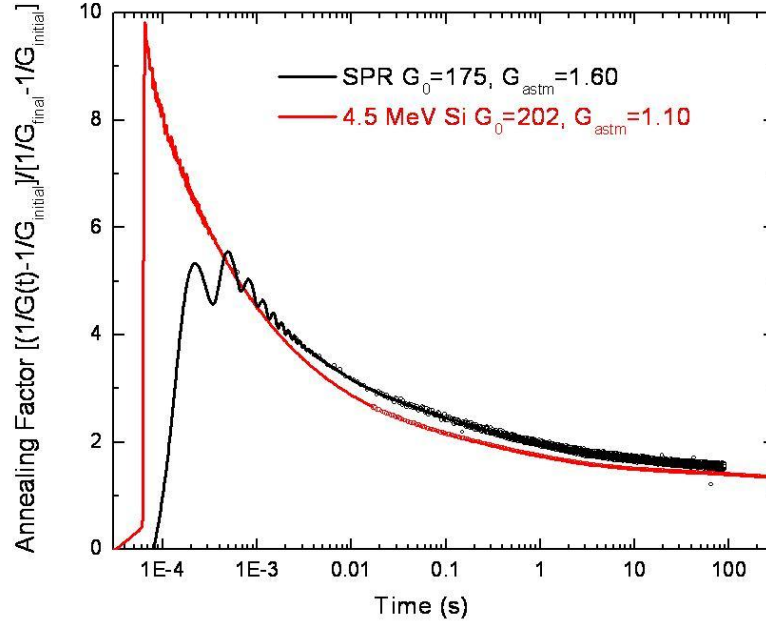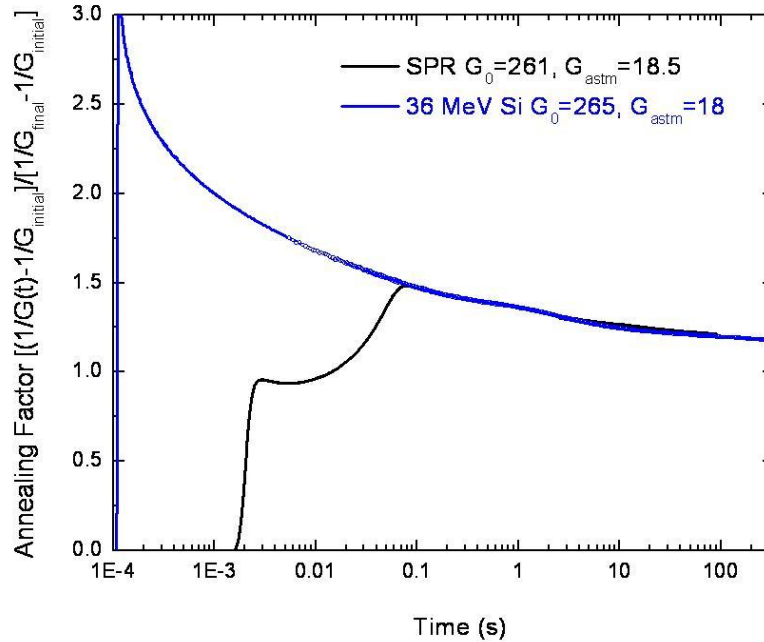


**Figure 2**. Comparison of a 36 MeV Si irradiation (blue) and a SPR-III minimum cavity pulse (black), where $G_0$ is the pre-irradiation gain and $G_{astm}$ is the final gain after ASTM (80 ℃ for 2 hr) anneal. There is excellent agreement for times $\geq \sim$ 0.1 s after the late-time gamma/neutron radiation from SPR-III dies away.

## *Initial Temperature Effects on Shock-Driven Power Supplies*

### *by* R. E. Setchell, S. T. Montgomery, M. U. Anderson, and D. E. Cox

**M**otivation—Shock-induced depoling of the lead zirconate/titanate ferroelectric ceramic PZT 95/5-2Nb is utilized in pulsed power supplies. Detonation of a small explosive charge produces a shock wave propagating initially through alumina-filled epoxy (ALOX) encapsulant and subsequently through PZT 95/5-2Nb elements. Operational temperatures can vary from approximately -55 to 75 °C, and power supply output decreases substantially with increasing temperature over this range. A challenge for device design is to meet minimum output requirements at the highest temperatures while avoiding high-voltage breakdowns due to excess output at the lowest temperatures. Numerical simulations of this temperature dependence have been frustrated because the contributing roles of temperature effects in ALOX alone and in PZT 95/5-2Nb alone had not been carefully studied.

**A**ccomplishment—Using a capability we established for conducting shock wave experiments over the temperature range of interest, we have investigated initial temperature effects on the shock properties of ALOX and PZT 95/5-2Nb separately. In PZT 95/5-2Nb, density changes over this temperature range are very small. Past experiments under short-circuit load conditions have shown that depoling currents are insensitive to initial temperature changes. Dielectric properties of ferroelectric ceramics, however, are known to be temperature dependent. When shock-induced depoling occurs under high field conditions, a portion of the depoling current is retained on the sample electrodes to account for sample capacitance. The retained current is "lost" in terms of delivery to an external circuit. Figure 1 shows the experimental configuration we have used to examine initial temperature effects on dielectric

properties during shock propagation. Two small PZT elements are contained within a target assembly, and depoling of one element provides a current to charge a circuit consisting of the other PZT element in parallel with a load resistor. Figure 2 shows results obtained in experiments at different initial temperatures. These results quantify how the capacitance of PZT 95/5-2Nb increases significantly with increasing temperature. This effect alone will result in decreased power supply output at higher temperatures. Figure 3 shows the experimental configuration we have used to investigate initial temperature effects on shock properties in ALOX. Density changes in this material over this temperature range are also very small. Laser interferometry (VISAR) is used to record transmitted wave profiles in experiments conducted using fixed impact conditions and target dimensions. Figure 4 shows results obtained in experiments at different initial temperatures using a baseline ALOX containing 43% by volume alumina. Shock speeds and peak stresses (calculated from measured conditions) decrease significantly with increasing temperature. These effects, primarily due to temperature-sensitive epoxy properties, will also result in decreased output from power supplies at higher temperatures.

**S**ignificance—Temperature-dependent output is an important issue in the design of shock-driven power supplies. We are providing the first detailed insights into initial temperature effects on the separate shock properties of ALOX and PZT 95/5-2Nb. By incorporating realistic temperature dependencies in dynamic material models, numerical simulations of power supply operation will be able to consider temperature effects while examining design parameters and margins.
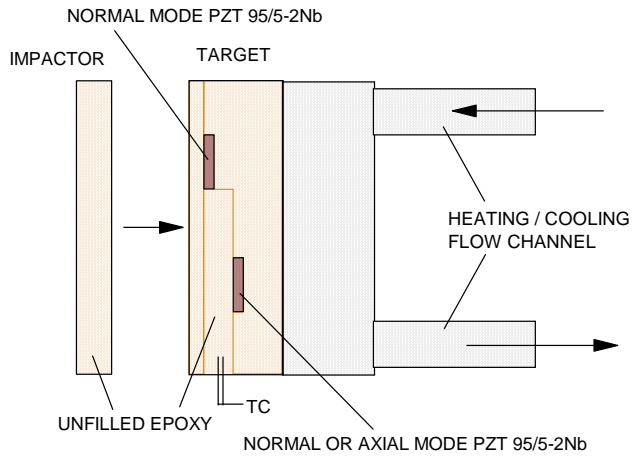
**Figure 1.** Configuration used for gas-gun experiments to investigate initial temperature effects on the dielectric properties of PZT 95/5-2Nb. Target temperatures are monitored using embedded thermocouples (indicated by "TC" in this figure).
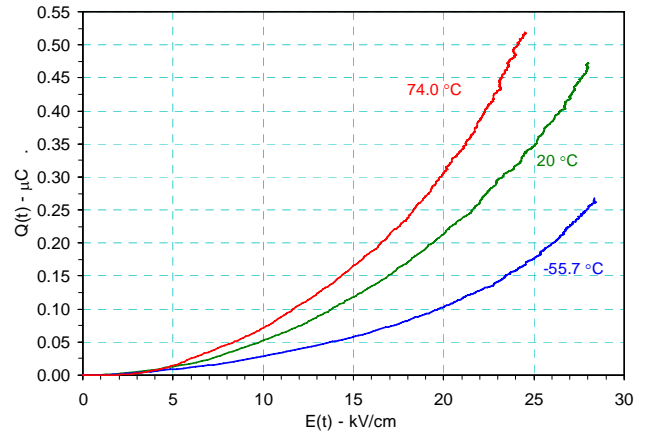
**Figure 2.** Charging of a poled PZT 95/5-2Nb sample in parallel with a load resistor by shock depoling of an adjacent PZT 95/5-2Nb sample. The displacement charge at a given time is plotted versus the electric field present at the same time. The time duration for the generation of each curve was 0.5 μs.
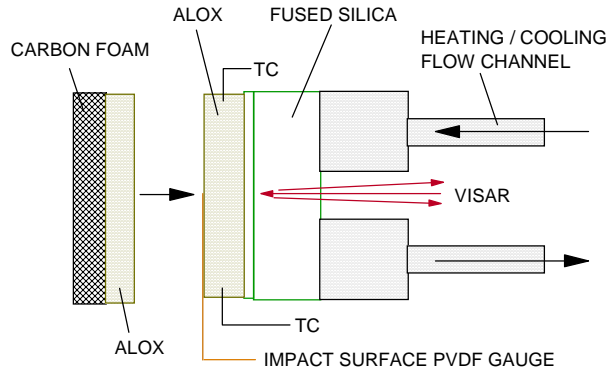




**Figure 3.** Configuration used for experiments to determine initial temperature effects on the shock compression and release properties of ALOX encapsulants.
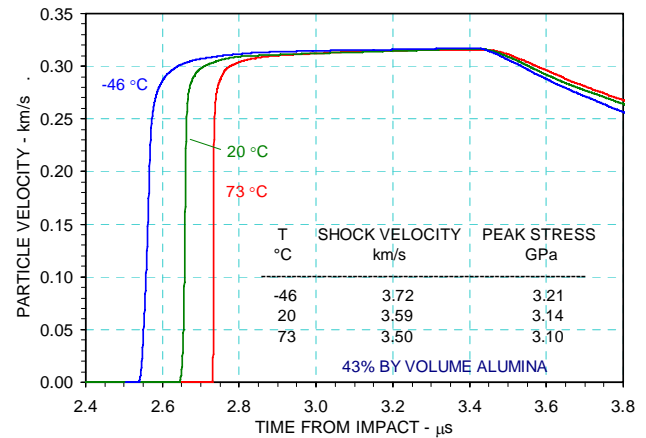
**Figure 4.** Transmitted wave profiles in baseline ALOX recorded in experiments conducted at different initial temperatures. Impact conditions and sample dimensions were the same in each experiment.

# Ion-Imaging Plasma Diagnostics

*by* **E. V. Barnat and P. A. Miller**

**M**otivation—Sandia is developing the 3-D unstructured-mesh plasma code "Aleph". The code will provide unprecedented capabilities for modeling plasma and charged-particle flows inside neutron tubes, a nuclear weapons component. This will greatly improve Sandia's computational capabilities for design and manufacturing of neutron tubes. In parallel with this code work, we are developing novel plasma diagnostic techniques and conducting experimental tests for code validation. The diagnostics and tests do not simulate details of neutron tubes but are designed to isolate key pieces of plasma physics that the code must be able to treat accurately for eventual success.

**A**ccomplishment—A plasma "sheath" is a region in which plasma properties change abruptly with spatial position. Plasma sheaths have been studied for decades, and their properties under different plasma conditions continue to be scientifically interesting and computationally challenging. The initial focus of our experimental studies is the extraction of an ion beam from quasi-neutral plasma. This effort tests the ability of the code to treat flowing, field-free plasma, its interaction with surfaces, and the transition in a sheath from plasma to a high-electric-field region in which an ion beam forms.

Figure 1 shows schematically the geometry of our experiment and the plasma and ion-beam behavior. We generated flowing plasma using a pulsed vacuum arc. That plasma expanded in a field-free region and was incident normally on a flat metal surface containing a 1-mm-wide rectangular slit (~12 mm long). Figure 1 shows a schematic view across the 1-mm slit. An acceleration electrode was located 5 mm away from the slit. The application of negative high voltage to the acceleration electrode caused extraction of an ion beam from the flowing plasma.

We used two different diagnostic techniques to characterize the ion beam. One diagnostic technique consisted of a linear array of Langmuir probes embedded in the acceleration electrode and oriented perpendicular to the slit. The probes were biased to collect ions and thus measured the ion current density distribution across the slit as a function of time. Figure 2 shows a photograph of the acceleration electrode with the embedded probes and sample data.

The other diagnostic technique yielded 2-D images of the ion beam distribution across the entire surface of the acceleration electrode. For this technique, the acceleration electrode consisted of a fine metal mesh and a biased phosphor screen 2 mm behind the mesh. Ion impact on the mesh generated secondary electrons that were accelerated to the phosphor screen. Electron impact on the phosphor generated a visible-light image of the spatial distribution of ions that was captured by a gated ICCD (intensified charge-coupled device) camera. Sample images for three different focusing conditions are shown in Fig. 3.

**S**ignificance—Diagnostic techniques that we developed are being used for validation of Sandia's new plasma code Aleph. We are comparing the observed and predicted dynamics of ion beam formation and propagation. This addresses sensitive and critical physics for the code. Successful validation will give confidence in use of the code for design and manufacturing of neutron tubes.
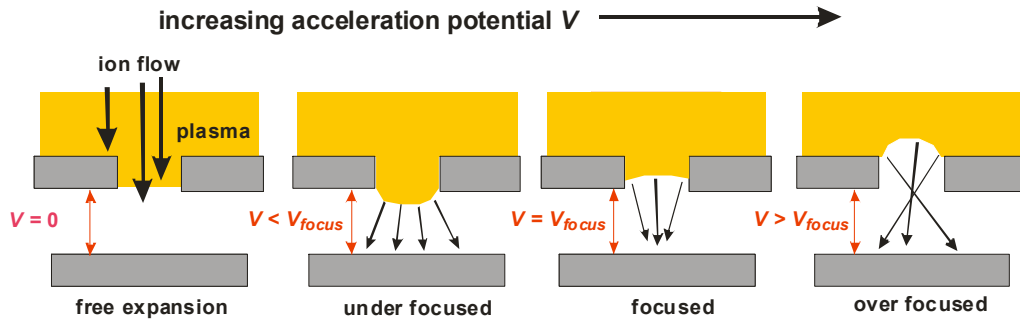
**Figure 1**. Plasma (yellow) flows downward towards a 1-mm-wide slit in an electrode. A potential *V* is applied to an ion-extraction electrode (bottom of each picture), accelerating ions through the hole and repelling electrons. A "meniscus" forms at the transition from plasma to ion beam. The shape of the meniscus depends on the plasma density, velocity, electron temperature, and *V*. The shape of the meniscus is inferred from the distribution of ion current on the extraction electrode.
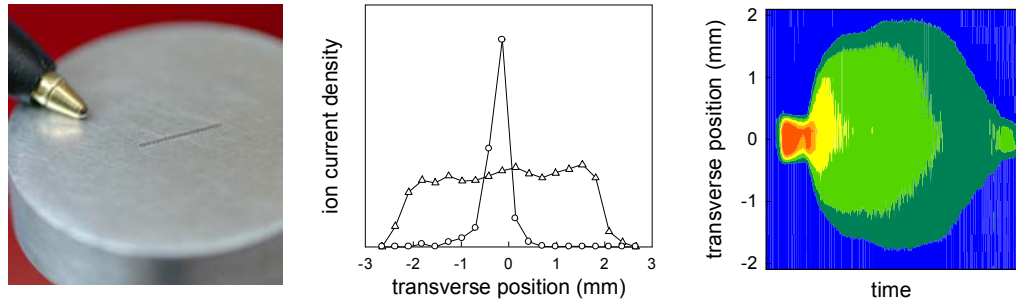


**Figure 2**. A linear array of ¼-mm-diameter Langmuir probes embedded in the 25-mm extraction electrode (left) measures ion current density. Sample data (middle) shows ion current density $J_i$ measured using 20 probes at two different times (different focusing conditions). Right graph ($J_i$ vs. position and time) shows dynamic focusing and defocusing during a single pulse.
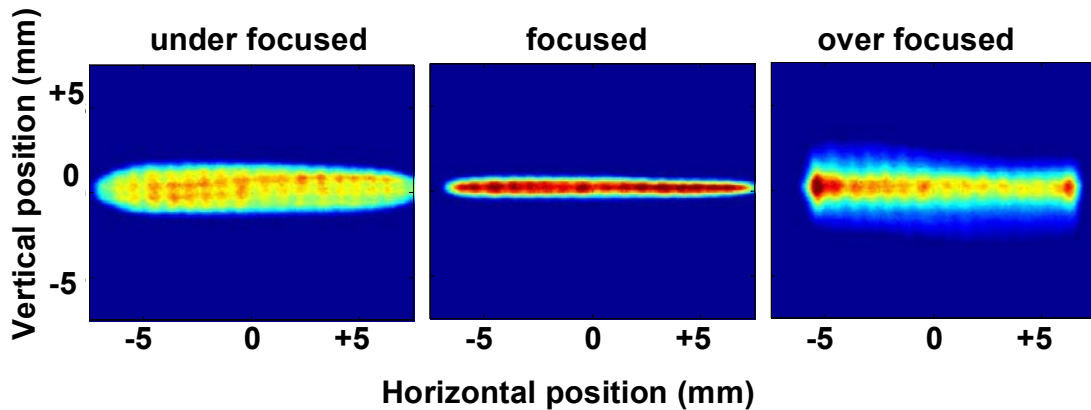


**Figure 3**. Data from the ion imaging diagnostic technique showing 2-D images of ions impacting the extraction electrode under three different focusing conditions. The images are snapshots at the same time for three different accelerating voltages.

# Interfacial Force Microscope (IFM) Application to MicroElectroMechanical (MEMS) Metrology

*by* **J. E. Houston**

**M**otivation—One of the weaknesses facing Sandia's MEMS-development effort involves the inability to accurately characterize the normally in-plane forces generated by the active elements, as well as how these forces progress through the chain of coupling components. At present, no technique is available for making such measurements. We are presently developing such a capability designed around the Sandia-developed Interfacial Force Microscope (IFM), which has the capability to obtain quantitative data of both normal and lateral forces at selective sites within a MEMS device. One particularly appealing candidate for such measurements involves a passive, bistable spring-element device being developed at Sandia.

**A**ccomplishment—Preliminary IFM demonstration measurements on a bistable MEMS device presently under the advanced stages of development are very encouraging, although the present model of the IFM is not ideally suited for this application and cannot be considered to be a true metrological instrument. Initial data were obtained on components similar to the one illustrated in Fig. 1a. Here, a shuttle is suspended by uniquely designed non-linear springs, which cause the device to be bistable, requiring a certain level of lateral force to cause the shuttle to change "state". The instability presents a particularly difficult problem for any force-measuring device. However, because of the inherent stability of the IFM concept, such measurements are possible on Sandia test units of this device. To implement the analysis, the IFM tip is optically located, for example, in the center of the T-bar end of the shuttle, illustrated

in Fig. 1b, and the component is moved against the tip while recording the lateral force vs. the displacement. This process proceeds until the point of instability, at which the shuttle suddenly "snaps" to its second stable position leaving the sensor behind under zero force. The tip is then located in the center of the "tab" on the other end of the shuttle and translated in the reverse direction. The two results are then matched at the point at which the forces suddenly go to zero. The result is shown in Fig. 2 (red) along with the modeling prediction (blue). Error bars indicate the confidence levels for the modeling and sensor calibration. Note that the instability occurs at the point at which the force slope changes sign, NOT at the maximum and minimum points.

**S**ignificance—For the first time, using IFM, we have shown that direct measurements of MEMS structures are available for comparison with finite element model predictions. This is an important step towards achieving model validation by directly measuring key parameters used in modeling and mechanism design. The overall observed force-displacement curve shapes are similar to simulation curves, but the critical parameter, i.e. the point of instability, is not the same, and the discrepancy remains even if the IFM result is scaled to have the same overall magnitude. At this point the designers believe that this discrepancy is due to residual stresses remaining in the device after fabrication. This IFM metrology has the potential for providing feedback data useful for design compensation of processing problems, ensuring that design criteria are acceptably met for all components distributed on the wafer.

**Contact:** Jack E. Houston, Surface & Interface Sciences, Dept. 1133
Phone: (505) 844-8939, Fax: (505) 844-5470, E-mail: jehoust@sandia.gov
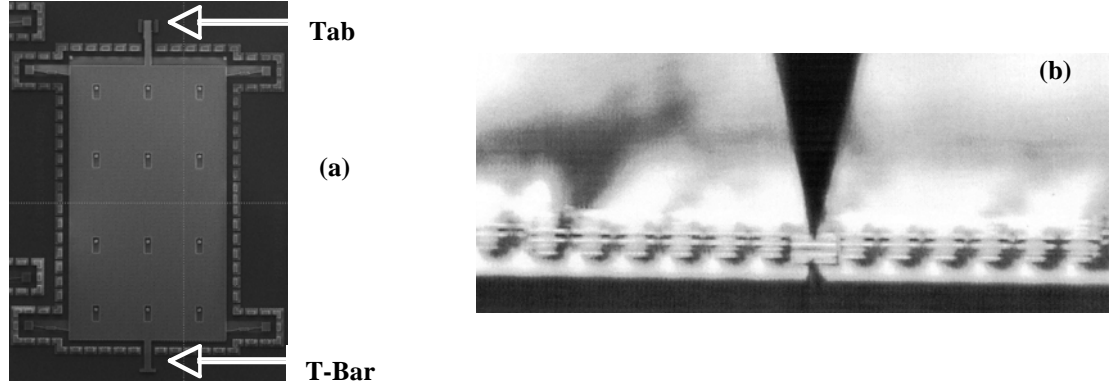
**Figure 1**. (a) A SEM image of the bistable MEMS component. The central shuttle is supported by nonlinear springs on each corner and is mechanically accessed by a "T-Bar" on the bottom and a "Tab" on the top. (b) A micrograph of the device viewed edge on from the bottom showing the IFM tip located in the center of the T-Bar in preparation for the displacement of the device downward to make contact with the tip.
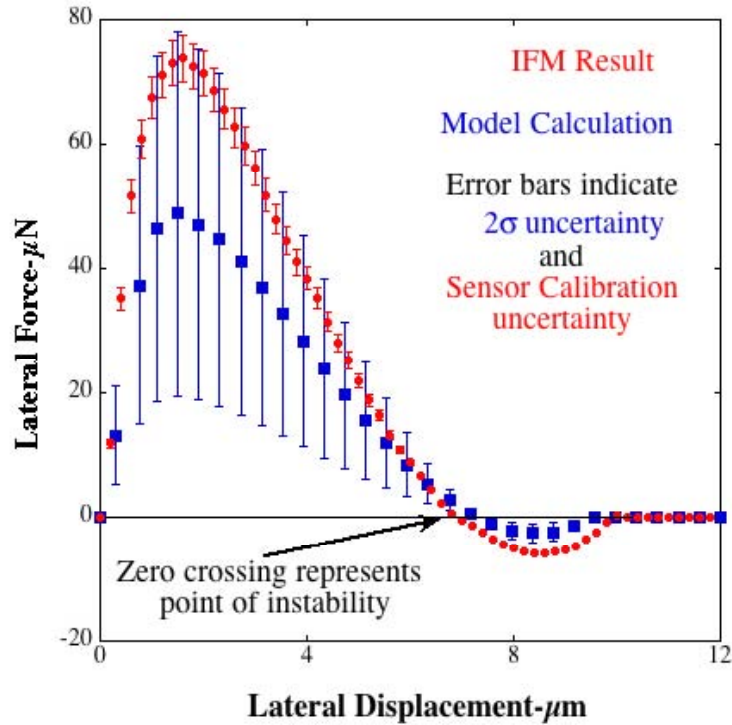


**Figure 2**. IFM results, shown in red, along with the model predictions in blue. The error bars indicate the confidence level of the modeling and the calibration of the IFM sensor. The IFM results are within the error bars for model but differ in scaling. However, even if the scaling is compensated, there still remains a significant discrepancy between the measured and predicted values for the instability point, i.e., where the slope of the two curves changes sign. This value represents the critical parameter in qualifying device performance.

# *ARES Upgrade: Time-resolved Spectral Measurements of Bio-aerosols*

*by* **P. J. Hargis, R. L. Schmitt, S. M. Sickafoose, M. W. Smith, T. A. Ashlock, M. Johnson, K. Sandquist, K. S. Rawlinson, D. Baiocchi, C. Boney, J. Daniels, C. Hrncir, B. Keeler, M. Pedroncelli, I. Shokair, and J. Grossman**

**M**otivation—Ares is a van-based UV laser-induced fluorescence (LIF) light direction and ranging (LIDAR) technology designed to detect biological agent clouds at up to 5 km. The original implementation utilized an intensified charge-couple device (ICCD) for time-gated spectrally dispersed fluorescence detection. While the system did have integrated cloud location and tracking, it was not able to separately collect dispersed fluorescence simultaneously from two different clouds and identify the individual clouds. In order to increase Ares' utility and provide the ability to measure spectra from different clouds within the same field-of-view separately, a multi-anode photomultiplier tube (MAPMT) was selected to replace the ICCD.

**A**ccomplishment—Over the last year, the Ares system has undergone a dramatic overhaul, including the redesign of electrical and mechanical systems, as well as the development of new control and analysis hardware and software in order to accommodate the new MAPMT detector.

The multidisciplinary Ares upgrade team included electrical, optical, mechanical, and software engineers from multiple organizations, led by members of the Lasers, Optics, & Remote Sensing Department.

The MAPMT detector collects the dispersed fluorescence over 32 spectral channels in time bins of 10 ns, which is equivalent to a spatial resolution of 1.5 meters away from Ares over a total distance of up to 5.1 km.

The testing and integration of the new detector required laboratory measurements of the sensitivity, responsiveness, and signal-to-noise of the detector to various levels of illumination, as well as a performance assessment of the new electronics.

Following reconstruction, the new and improved Ares was relocated to the sled track in order for the full system to be tested under near field test conditions. These tests permitted debugging and characterization of the entire Ares system. Real deployment occurred in late August 2007.

These extensive upgrade efforts culminated in a two-and-a-half week field test at Dugway Proving Ground, Dugway, Utah as part of the Joint Biological Stand-off Detection System (JBSDS) Increment II test. During this field test, bioaerosols including bioagent simulants and typical interferents were released at two different facilities, and time-resolved laser-induced fluorescence was measured with Ares. One facility was a controlled breeze tunnel and one was an open-air release area. In both cases, the improved Ares was able to effectively collect the dispersed fluorescence from the various bio-releases. The interpretation and analysis of the data is ongoing and will provide a quantitative measurement of the new detector system.

**S**ignificance—The ability to interrogate and identify multiple clouds, in real time, at multiple distances relative to the point of observation is a critical component for defense either on the battlefield or for homeland security. Ares is an easily fieldable research instrument capable of the detection and identification of multiple bioaerosols at multiple distances in real time.

**Contact:** Shane M. Sickafoose; Lasers, Optics, & Remote Sensing, Dept. 1128
Phone: (505) 845-8362, Fax: (505) 844-5459, E-mail: smsicka@sandia.gov

**Figure 1**.  Ares instrument during deployment at Dugway Proving Ground, Utah in August 2007.
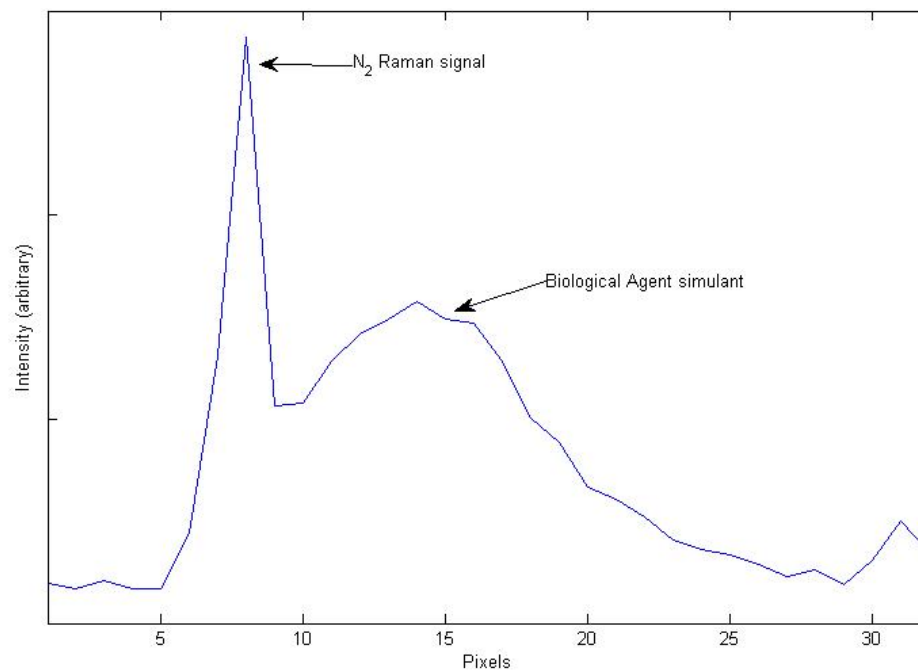


**Figure 2**.  Dispersed fluorescence spectrum of $N_2$ Raman line and biological agent simulant released at Dugway Proving Ground.

# Nanoscience and Nanotechnology

# Center for Integrated Nanotechnologies (CINT):   Overview

### *by* R. Q. Hwang

**Motivation**—The Center for Integrated Nanotechnologies (CINT) is a Department of Energy/Office of Science Nanoscale Science Research Center (NSRC) operating as a national user facility devoted to establishing the scientific principles that govern the design, performance, and integration of nanoscale materials.

CINT is one of five NSRCs throughout the U.S. that form an integrated national program, affiliated with major facilities at the DOE's National Laboratories, to cover the diverse aspects of nanoscience and technology. This complex aspires to become a cornerstone of the nation's nanotechnology revolution, contributing to DOE's principal missions in national defense, energy, and the environment while providing an invaluable resource for universities and industries.

Through its Core Facility in Albuquerque with gateways to both Los Alamos and Sandia National Laboratories, CINT provides open access to tools and expertise needed to explore the continuum from scientific discovery to the integration of nanostructures into the micro- and macro world.   This pathway involves the experimental and theoretical exploration of behavior, the development of a wide variety of synthesis and processing approaches, and an understanding of new performance regimes testing design and integration of nanoscale materials and structures. Integration itself is key to the exploitation of nanomaterials, and the scientific challenges that it poses are at the heart of CINT's mission.

Now in its first year of full operations, CINT is hosting users from more than 30 states and 10 foreign countries.  Recent progress is detailed in following Briefs which give a sense of the breadth of ongoing work in CINT.

**A**ccomplishment—Mike Lilly, John Reno, and co-workers are exploring the interactions of electrons and holes in closely spaced electron and hole two-dimensional sheets.   These experiments are possible only due to the extraordinarily high quality GaAs/AlGaAs material grown in CINT.

Normand Modine and collaborators from the University of Michigan have developed theoretical understanding of the observed multiple surface reconstructions in compound semiconductor alloys.  Their results demonstrate the influence of both atomic size mismatch and lattice mismatch strains on the resulting reconstructions.

Brian Swartzentruber has developed a nanomanipulator that can measure properties of as-grown nanostructures, as well as manipulate nanostructures to control their placement and build more complex configurations.

Gary Kellogg is using the low energy electron microscope available in CINT to study how chemical heterogeneity develops at surfaces. This work may shed light on approaches to mitigating the effect of electromigration on Cu interconnects in microelectronics.

Dale Huber is working with scientists at a local company in Albuquerque to develop magnetic nanoparticles that could be used in new diagnostic techniques for detecting disease.

Additional information on CINT is available at http://cint.lanl.gov/

**Contact:**   Robert Q. Hwang, Energy Sciences, Dept. 1130
            Phone:  (505) 844-5852, Fax:  (505) 284-7778, E-mail:  rqhwang@sandia.gov

**Figure 1**. The 96,000 ft$^2$ CINT Core Facility features state-of-the-art facilities for the synthesis, characterization, and integration of nanoscale materials and structures.



**Figure 2.** The CINT Core Facility capabilities include (clockwise from upper left): chemical synthesis; class 1000 cleanroom, molecular beam epitaxy growth of compound semiconductors; and transmission electron microscopy.

# Enhanced Interaction in Closely Spaced Electron-hole Bilayers

## *by* M. P. Lilly, J. A. Seamons, C. P. Morath, and J. L. Reno

**M**otivation—Bilayers of two-dimensional electron systems at zero magnetic field can be well described as individual layers that are weakly coupled. Simply changing the polarity of one of the layers to hole instead of electron leads to completely different physics at low temperature and low density. The ground state electron-hole bilayers (EHBLs) are expected to undergo a transition to strong coupling and ultimately a Bose-Einstein condensation. Our experiments use electrical transport techniques in GaAs heterostructures to explore the strong coupling of EHBLs.

**A**ccomplishment—We have fabricated electron-hole bilayers devices with separate electrical contact to each layer and performed transport measurements that reveal new physics in the strong coupling regime. A cross section of our devices is shown in Fig. 1a. The heterostructure is composed of 18 nm GaAs quantum wells where the 2D layers are formed (white), separated by undoped AlGaAs (gray) layers above, below, and between the quantum wells. The barrier between the wells is small so that the exciton energy is large, but not too small so that recombination rates are small. For the data described here, devices with 20 nm (sample A and B) and 30 nm (sample C) barriers are measured. The electrons and holes are pulled into the quantum wells from the contacts using electric fields generated by top and bottom gates. In addition, a voltage between the layers is required to overcome the GaAs bandgap and create the EHBL. The mobility of the electron and hole layers is shown in Fig. 1b. This demonstrates both the range of density (as low as $3 \times 10^{10}$ cm$^{-2}$) and high mobility ($>10^5$ cm$^2$/Vs) indicating low background disorder for each layer. While

device fabrication and operation are quite complicated, these structures achieve our main goals of variable density, high mobility, independent contacts, and narrow barriers.

Our main result is shown in Fig. 2. In an effort to study the coupling *between* the electron and hole layers, we drive a current in the electron layer and measure the voltage that develops in the hole layer. The result of this measurement, called Coulomb drag, is a drag resistivity ($\rho_{drag} \sim V_h/I_e$) that depends on scattering mechanisms and interaction between the layers, since no current is actually flowing in the hole layer where the voltage is measured. If the layers are independent, the drag resistivity would be zero. Scattering due to the charge of the carriers leads to weak coupling and a $T^2$ temperature dependence which can be seen above 0.8 K for the data in Fig. 2a. Strong coupling leads to an increase in the drag signal since electron and hole want to move together. Our drag data for both Samples A and B shows an upturn in the drag at the lowest temperature. The position of the upturn as a function of density is shown in Fig. 2b.

**S**ignificance—The increase in drag at low temperature indicates that the interaction between the electron and hole layers gets dramatically strong at low temperature for the narrow barrier devices. Because we do not directly measure coherence, it is difficult to conclusively identify this new regime as exciton condensation, but our results clearly indicate entry into a strong coupling regime, and explanations related to exciton formation, fluctuations above a critical temperature or actual condensation are likely.
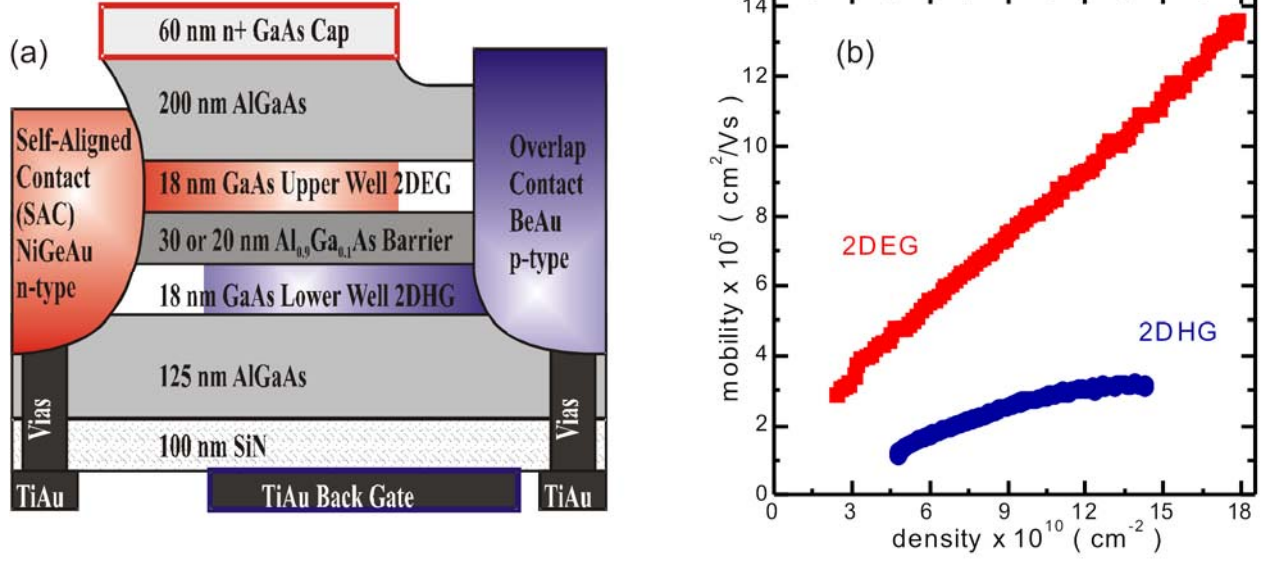
**Figure 1**. (a) Cross section of electron-hole bilayers device. Operation requires both top and back gate voltages, as well as a voltage between the electron and hole layers. (b) Mobility of electron and hole layers at T=0.3K for sample C. Carrier density in each layer can be independently controlled.
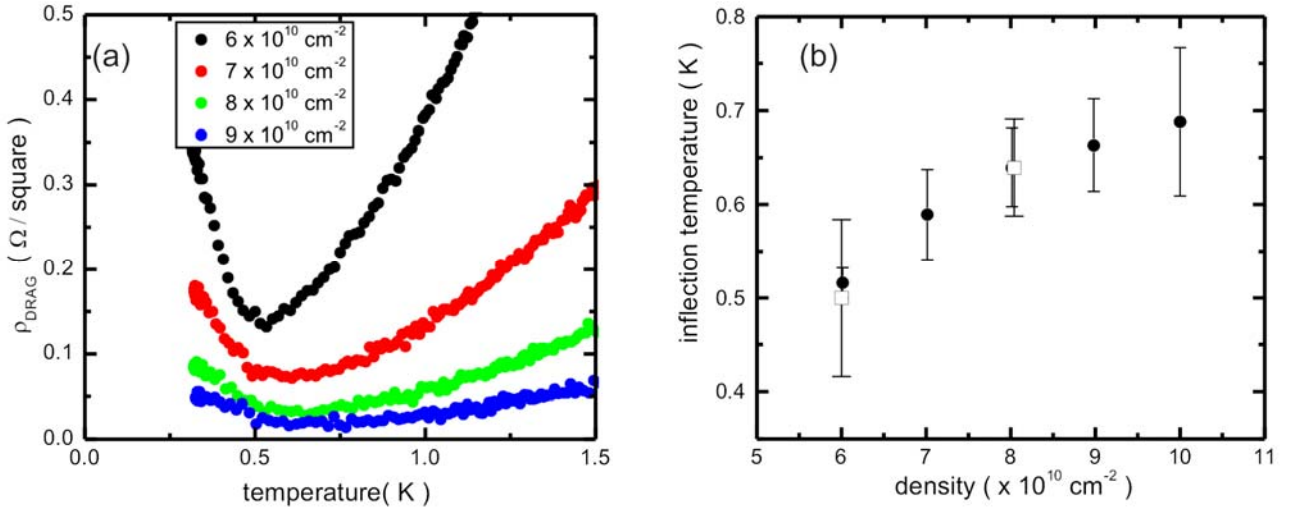


**Figure 2**. Coulomb drag results on sample A as a function of temperature for several matched densities (n=p) indicated in the legend. The $T^2$ behavior at high temperature is expected for independent 2D systems. The increase in drag at low temperature arises from strong coupling between the layers at low temperature. (b) The minimum in the drag resistivity for sample A (solid circles) and sample B (open squares) as a function of carrier density maps the transition from independent electrons and holes (upper left) to strongly coupled layers (lower right). The strong coupling region may indicate exciton condensation or it may signal the onset of condensate fluctuations above the critical temperature.

# *Strain Induced Surface Reconstructions of Compound Semiconductor Alloys*

*by* **N. A. Modine, J. E. Bickel\*, A. Van Der Ven\*, C. A. Pearson\*\*, and J. Mirecki Millunchick\***

**M**otivation—The nanoscale structure of crystalline surfaces is controlled by competing interactions between the constituent atoms. For example, compound semiconductor surfaces typically reconstruct in order to eliminate dangling bonds and reduce their surface energy. It is generally accepted that three principal factors influence the stable surface reconstruction: local chemistry, the electron counting rule, and local strain due to the displacement of atoms from their bulk positions. These factors readily explain the surface reconstructions present in binary III-V semiconductor systems. However, when alloying occurs, coexistence of nanoscale domains of multiple reconstructions and new reconstructions not observed for the binary systems suggest that other factors also contribute. We propose that global lattice mismatch strain and localized atomic size mismatch strain are additional factors that greatly influence the surface structure of compound semiconductor alloys.

**A**ccomplishment—InAs and GaAs both form stable surfaces of a single reconstructions varying from c(4x4) to $\beta2(2x4)$ to $\alpha2(2x4)$ to (4x2) as a function of chemical potential $\mu$. The ternary alloy InGaAs, however, shows multiple reconstructions for a single $\mu$. For example, on $In_{0.27}Ga_{0.73}As$/GaAs, a (4x3) reconstruction unique to the alloy system coexists with nanoscale domains of what appears to be an $\alpha2(2x4)$ reconstruction. Studies of the $\alpha2(2x4)$ show that the surface dimer, rather than being stochastically distributed between the two possible positions instead regularly alternates position 80% of the time. *Ab Initio* studies based on the Kohn-Sham Density Functional Theory show that localized strain due to ordering of indium atoms in the first subsurface layer induces an ordering of the surface dimers. These results demonstrate the important influence of atomic size mismatch strain on the surface reconstructions of alloyed compound semiconductor systems.

A coexistence of surface reconstructions also occurs when thin films of GaSb are grown on GaAs. The film develops by nucleating small islands of $\alpha(4x3)$. The center of these islands transform to the $\alpha2(2x4)$ reconstruction above the critical island size of $30\pm10nm^2$. The lattice mismatch of film and surface is 7%, and DFT simulations suggest this drives the surface coexistence. The $\alpha(4x3)$ is stable at the GaSb lattice parameter, whereas the $\alpha2(2x4)$ is stabilized at the GaAs lattice parameter. At the center of the island where the lattice parameter is constrained to that of the substrate, the $\alpha2(2x4)$ appears, whereas at the edge of the island where the lattice parameter can elastically relax, an $\alpha(4x3)$ reconstruction appears. This demonstrates the important influence of lattice mismatch strain on the surface reconstructions of alloyed compound semiconductor systems.

**S**ignificance—Surface reconstructions play an important role in the growth of thin films and devices, influencing the compositional and morphological structure of the grown material at the nanoscale. It is important to understand the surface structure in order to control the nanoscale structure of devices made of III-V semiconductors.

**\* University of Michigan, Ann Arbor**
**\*\* University of Michigan, Flint**
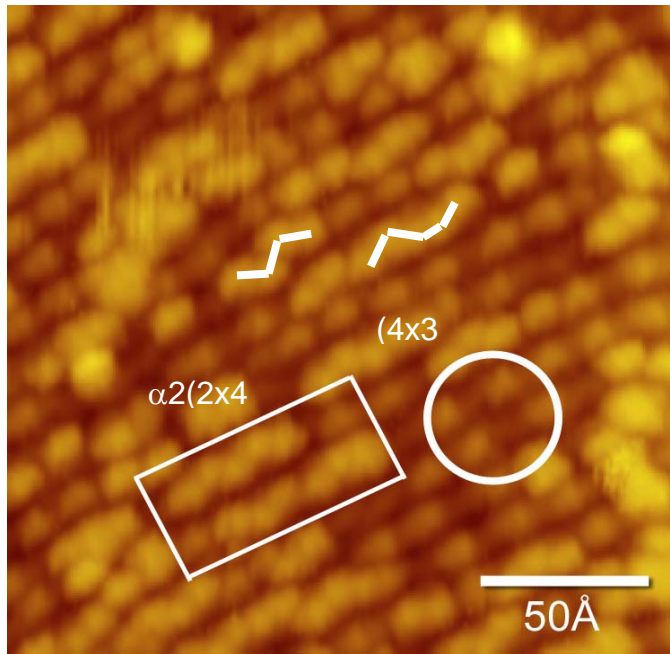
**Figure 1**. Scanning Tunneling Microscope (STM) image of a 25 monolayer film of $In_{0.27}Ga_{0.73}As$ grown on GaAs at 493°C. Nanoscale domains of α2(2x4) exist within a matrix of a (4x3) unique to the alloy system, and the alternation of the α2(2x4) surface dimer is apparent.
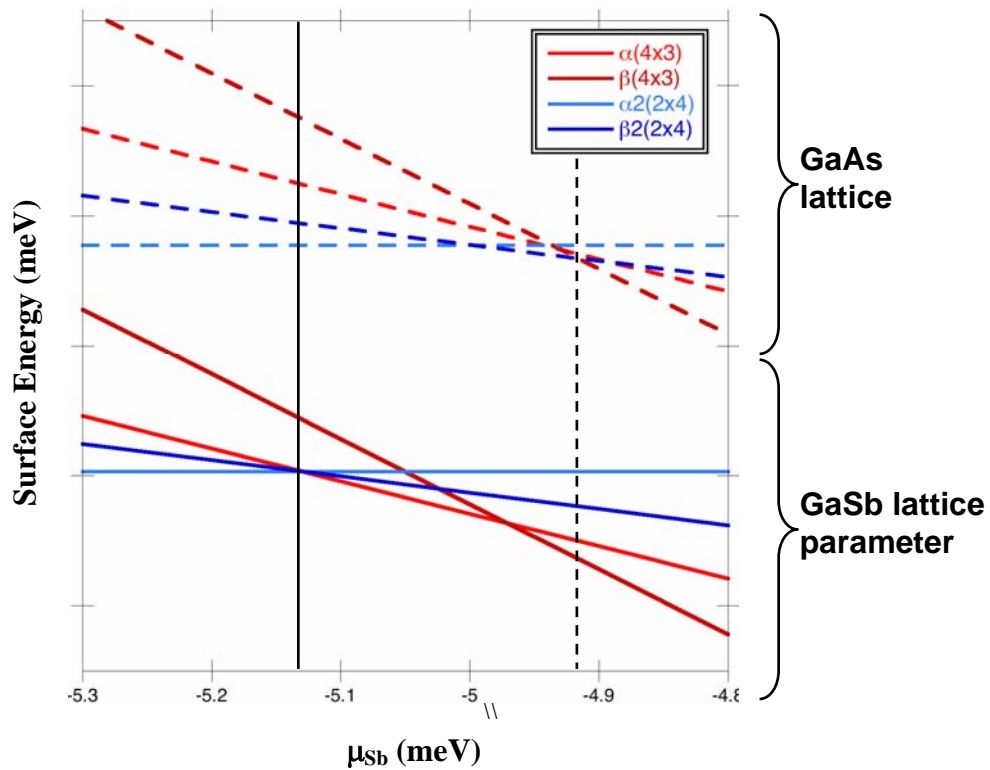


**Figure 2**. Surface energies of various reconstructions of GaSb calculated with the Density Functional Theory (DFT) as a function of chemical potential. Under growth conditions, the (4x3) is stable at the GaSb lattice parameter, while the (2x4) is stable at the GaAs lattice parameter.

# Nanomanipulator for Electronic Characterization and Top-Down Construction of Unique Nanostructures

## *by* B. S. Swartzentruber

**M**otivation—Nanostructures have properties that differ from bulk values due to their inherently small size and their high surface-to-bulk atom ratio. One stumbling block in the measurement of nanostructure material and electronic properties is the difficulty to position them precisely where they are needed. The problem is two-fold – imaging the nanostructures and their surroundings, and manipulating them on the nanometer length scale. Current methods for positioning rely on random deposition of nanostructures from solvents, gas phase, and vacuum growth techniques, followed by a post-mortem determination of their location. This methodology limits the throughput and the statistical accuracy of nanostructure property measurements.

**A**ccomplishment—To increase measurement throughput and develop a flexible manipulation framework, we built a scanning-probe-based nanomanipulator inside of a JEOL 6701F field-emission scanning electron microscope (SEM) with ~1 nm resolution. Tungsten probe tips, etched to end radii as small as 20 nm, are coated with a variety of metals to measure different nanostructure interface properties. With fine motion control based on a piezo actuator and coarse motion via stick-slip translation stages, the probes are positioned within ~1 cm$^3$ volume with sub-nanometer precision. To facilitate manipulation, fine positioning is accomplished through a dual-joystick interface. This allows direct intuitive control while imaging with the SEM in real time. Individual nanostructures are chosen and the probe positioned precisely for contact. Electronic structure measurements are performed with high-precision current-voltage sources.

Figure 1 is a false-colored SEM image of a gold-coated tungsten probe contacting the top of a vertical GaN rod directly on the growth wafer. Current-voltage curves are plotted in Fig. 2. Current passes through the rod and is collected on the growth wafer with large area silver paint serving as the back electrode. Upon initial contact, a Schottky barrier forms at the Au-GaN interface that limits the conduction. This Schottky behavior is plotted in blue in Fig. 2. After passing a large current (> 10 μA) through the rod, the Schottky interface is destroyed and the current increases > 100-fold. The current is then limited by conduction through the rod and is best described by space-charge limited conduction (IV plotted in red in Fig. 2). This sequence of Schottky to space-charge-limited current can be repeated on any number of rods.

**S**ignificance—Measuring nanostructure properties in their as-grown configuration eliminates uncertainties due to ex-situ processing. The comparison of measurements on as-grown structures with those with processed contacts gives insight into contact and interface formation. Many nanorods can be individually addressed for comparison and properties correlated with shape and length. Adding multiple probes to this tool will enable not only direct and precise control over the placement of individual nanostructures, but also of their position with respect to each other – a currently unattainable ideal.

**Contact:**   Brian S. Swartzentruber, CINT Science, Dept. 1132
Phone:  (505) 844-6393, Fax:  (505) 284-7778, E-mail:  bsswart@sandia.gov

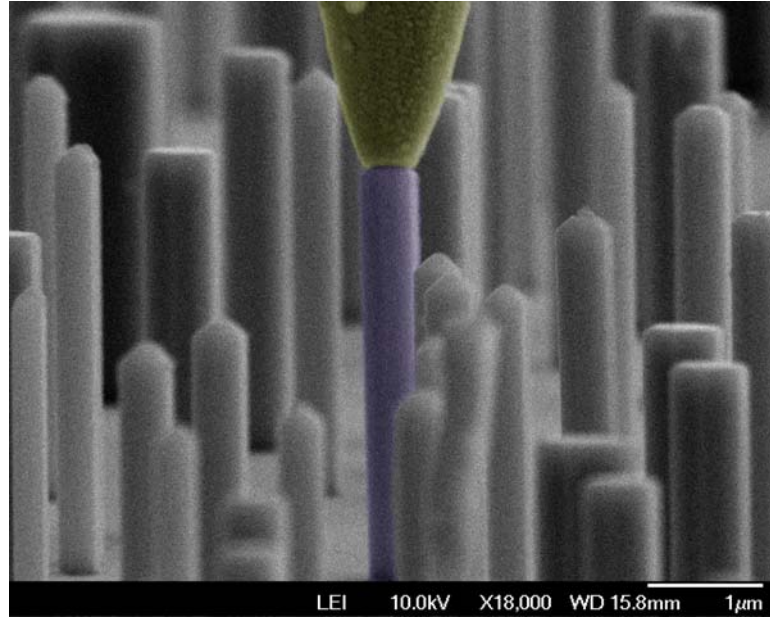**Figure 1**. False-colored SEM image of gold-coated tungsten probe contacting GaN rod for electrical characterization. Each rod can be individually addressed.
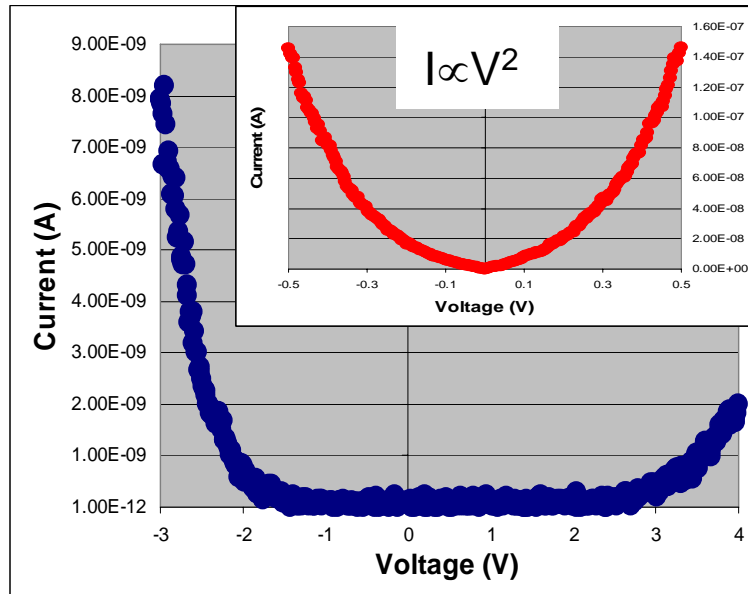


**Figure 2**. Current versus voltage curves for GaN rods. At initial contact, a Schottky barrier forms at the GaN-Au interface (blue). When the interface is disrupted by pushing harder or through high current, the conduction becomes space-charge limited (red).

# *Identifying the Origins of Heterogeneity in Ultra-thin Films by LEEM-IV Analysis*

### *by* Gary Kellogg

**M**otivation—Surface alloy formation plays a key role in many technologies. An application of current interest in the microelectronics industry is the potential use of surface alloys as a means to reduce the detrimental effect of electromigration on Cu interconnects. This process is mediated by surface diffusion, and the search is on for coating metals that reduce surface diffusion but do not increase bulk resistance – i.e., metals that do not alloy. Pd films have been shown to reduce electromigration, but since Pd and Cu are miscible, bulk alloying is a potential problem. Consequently, understanding how, and at what temperature, Pd intermixes with Cu is of considerable interest.

**A**ccomplishment—Our low energy electron microscope (LEEM) images show clearly that the growth of Pd on Cu(001) is *not* uniform (Fig. 1). The surface contains a number of single-atomic layer steps, identified by sharp changes in image contrast. In these regions, one sees dendritic-type growth outward from the advancing step and a continuous decrease in imaging intensity in the opposite direction towards the original step position. Precisely how the surface is inhomogeneous and the extent of the intermixing during growth, however, cannot be determined from the images alone. The key information needed to understand the heterogeneity that develops during surface alloying is a quantitative measure of the spatial and depth distribution of the deposited Pd. To obtain this information, we have developed a new LEEM-based technique to determine the three-dimensional composition profile of a surface with 8-nm spatial resolution. In our "LEEM-IV" analysis, we measure reflected electron intensity vs. incident energy curves (so-called "IV" curves) pixel-by-pixel for the entire LEEM image. We then analyze the reflectivity data using multiple-scattering low energy electron diffraction (LEED) calculations (in analogy with conventional LEED-IV analysis). With this new technique, we have measured the spatial and depth distribution of Pd on Cu(001) as a function of deposition time. Color-coded maps indicating how the Pd concentration varies in the vicinity of a surface step are shown in Fig. 2a. From the time-evolution of such 3-d compositional profiles, we show that the heterogeneity observed in Fig. 1 can be explained with a conceptually simple "step-overgrowth" model (Fig. 2b) in which step flow converts mobile Pd in the second layer into fixed Pd in the third layer.

**S**ignificance—Understanding how chemical heterogeneity develops at surfaces is a key challenge in the engineering of thin-films. By carefully mapping the three-dimensional compositional profile of Pd near surface steps, we have identified the exact process – step overgrowth coupled with inhibited bulk diffusion – that gives rise to heterogeneity in Pd/Cu(001) surface alloys. Although the model was developed specifically for Pd/Cu(001), step overgrowth requires only fast surface diffusion and relatively slow bulk diffusion. This state of affairs is quite common in thin-film growth, and the same mechanism should be operative generally.

**Contact:** Gary L. Kellogg, Surface & Interface Sciences, Dept. 1114
Phone: (505) 844-2079, Fax: (505) 844-5470, E-mail: glkello@sandia.gov
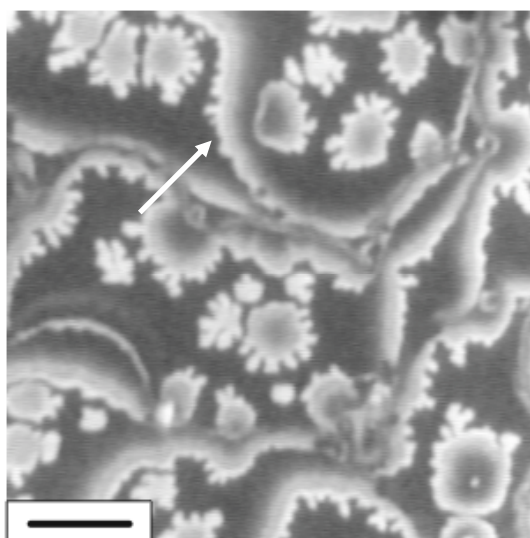
**Figure 1**. LEEM image (electron energy = 13.1 eV) recorded after the deposition of ~0.6 ML Pd on Cu(001) at 200 ºC. The gradual decrease in reflected electron intensity moving away from surface steps (white arrow) is unusual as is the dendritic-like growth along the steps. Scale bar = 1 $\mu$m.



(a)                                                                 (b)
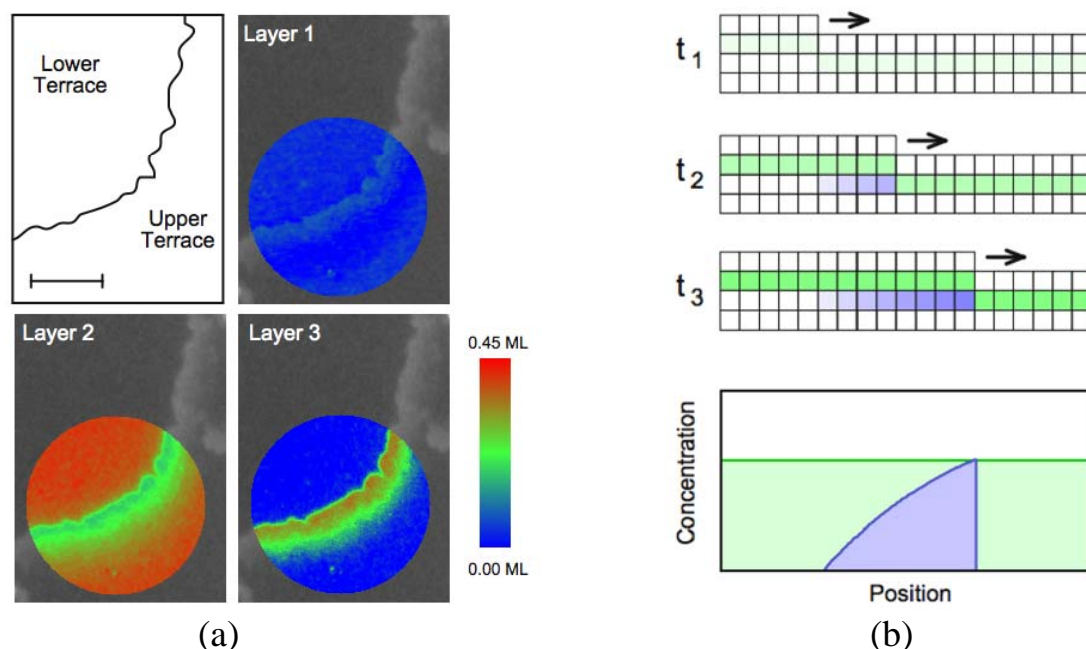
**Figure 2**.  (a) Three-dimensional maps of the Pd concentration near a surface step. The images were constructed from the analysis of 17,665 individual pixels. The maps are superimposed on the corresponding LEEM image at 13.1 eV. Scale bar = 500 nm.   (b) Schematic illustrating how heterogeneity arises during step-flow overgrowth. (top) Side views of the Cu surface. The Pd composition in the second layer is shown in green, in the third layer blue. Step flow overgrowth converts mobile Pd in the second layer into fixed Pd in the third layer. (bottom) Spatial dependence of the Pd concentration in the second (green) and third (blue) layers at the end of growth.

# Magnetic Nanoparticles for Biomedical Imaging

### *by* D. L. Huber

**M**otivation—Senior Scientific Limited Liability Company (LLC) has been developing a new approach for detecting a variety of diseases using magnetic nanoparticles. The technique requires super-paramagnetic nanoparticles of a very narrow size range to be bound to the diseased tissue of choice. The commercial unavailability of well-defined magnetic nanoparticles of the proper size and with appropriate functionality brought them to the Center for Integrated Nanotechnologies (CINT). The goal was to design and synthesize ideally suited particles for this application.

**A**ccomplishment—This technique uses magnetic sensors to detect and image a variety of diseases by using magnetic nanoparticles with antibodies to specific tissues (e.g., breast cancer and leukemia). The targeted nanoparticles bind to the cells of interest, and their presence is detected magnetically. The magnetic detection is achieved by briefly applying a modest magnetic field (~30 Gauss) and measuring the remanence field as a function of time using a number of extremely sensitive superconducting quantum interference device (SQUID) sensors. The remanence field in magnetic nanoparticles decays through two mechanisms: Brownian motion and Néel relaxation (motion of the internal magnetic moment). Decay by Brownian motion occurs extremely quickly (< 10 msec) for particles that are not bound to cells of interest, while bound nanoparticles decay over the course of hundreds of milliseconds to seconds. The slower Néel relaxation is measured and indicates the presence of the cells of interest. This extremely low background detection method has been shown to have detection limits about three orders of magnitude lower than current diagnostic methods.

Only particles within a narrow range of sizes have an appropriate rate of Néel relaxation; this size has been theoretically calculated to be 25 nm in diameter (for spheres of magnetite). Commercial suppliers exist for magnetite nanoparticles, but the material tends to be polydisperse. The most useful commercial sample found to date has only about 7% of the expected signal due to Néel relaxation. Measurements on commercial samples as part of this project have explained the lack of signal. A transmission electron micrograph of the sample (Fig. 1) shows that the particles are irregularly shaped, polydisperse, and below the optimum size. A synthesis method developed at CINT (Fig. 2) yields magnetite particles with a narrower polydispersity, roughly spherical particles, and an average size of approximately 25 nm. These particles appear to be ideal for this application, and magnetic measurements demonstrate that these particles have a signal of greater than four times the commercial sample. There is still room for improvement in the particle synthesis by optimizing for the precise size that yields the highest signal. The size calculated to yield the maximum signal was based on assumed bulk-like properties of the magnetite and is therefore expected to be imprecise.

**S**ignificance—This extremely promising medical imaging technique is completely dependent upon having nanoparticles of precisely the correct size. The materials synthesis expertise available at CINT was quickly able to design a synthesis to meet the exacting needs. Our next goals are to improve the signal, attach functional coatings to enhance the stability, and finally get FDA approval for injection into humans to commercialize this potentially revolutionary imaging technique.

---
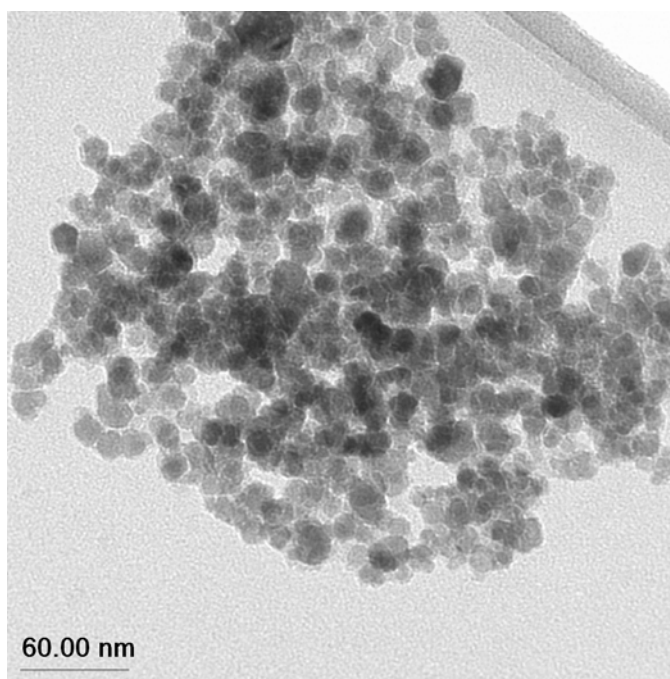
**Figure 1**. Commercial nanoparticles are agglomerated, polydisperse, oddly shaped, and smaller than the desired 25 nm.
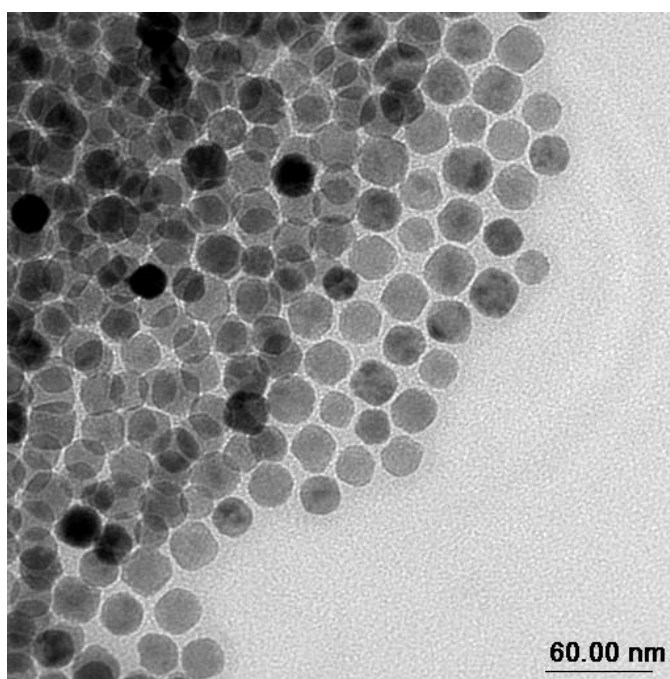


**Figure 2**. Particles synthesized at CINT are rounder, less polydisperse, and have been synthesized in the desired size range.

# *Irradiation for the Novel Radiolytic Formation of Superalloy Nanoparticles*

*by* **T. M. Nenoff, K. Leung, D. Berry, J. Knapp, P. Provencio, and  J. Jones**

**M**otivation—Superalloys are high temperature, corrosion resistant inorganic materials with both defense and civilian applications. The ability to make them nanoscale allows for a wide variety of nanotechnology applications. We are using radiolysis to develop a universal method to make nanoparticles of metals, alloys and superalloys. The combination of irradiation source, solution electrochemistry, and surface modification by ligands allows for control of size, morphology and composition.

**A**ccomplishment—We are synthesizing metallic and alloy nanoparticles in a novel way that allows for (1) exploration of metastable phase space not accessible by traditional alloy synthesis methods (i.e., melting), (2) synthesis of ultrafine/nanoparticles that enables uniform sintering as opposed to cast melting that grows in defects, and (3) possible controlled anisotropic nanoparticle growth through selective capping. We are combining basic research and an iterative feed-back loop of density functional theory (DFT) modeling, which is then applied directly to variables of materials synthesis. We have successfully designed, built, and utilized reaction setups for both the gamma irradiation facility (GIF) source (dose rate $\approx$ 75 rads/sec) and ion beam reactors (dose rate is $\approx$ 4400 rad/sec). Synthetic reaction procedures have also been developed for both irradiation set-ups. In this first year, we tested a number of experimental variables and their effects on nanoparticle formation. They include the role of (1) dose rate, (2) radical inhibitor, (3) dose, (4) irradiation exposure time, and (5) organic type. Our initial studies were on gold; we then began experimentation on Ni, Pd, Ag, Ag/Ni, Pd/Ni metals of interest for both superalloys and metal-alloy hydrogen membranes. All the variables play a role in determining shape, size, and composition of nanoparticles (Figs. 1 & 2).

Concurrently we are running *ab initio* molecular dynamics (AIMD), which treats the valence electrons of all species quantum mechanically, and is capable of describing chemical reactions and electron transfer events. We have applied AIMD to examine the hydration of mono- and diatomic Ag and Ni species in water. Ag and Ni are found to behave very differently in water. Ag behaves like a hydrophobic sphere, while Ni is highly hydrated (Fig. 3). This helps explain initial synthetic results of nonuniform stoichiometry in nanoparticle-organic cluster formation (Fig. 2).

Modeling combined with experimentation aids in the understanding of critical science issues related to nucleation, alloy formation, and metal clusters-organics binding in water.

**S**ignificance—The possibility of synthesizing a wide variety of metastable superalloy phases that can be made only by sintering rather than melting is very exciting. We expect that our successes will be broadly useful in structural applications requiring high strength:fracture ratios.

**Contact:**    Tina M. Nenoff, Surface & Interface Sciences, Dept. 1114
        Phone:  (505) 844-0340, Fax:  (505) 844-5470, E-mail:  tmnenof@sandia.gov
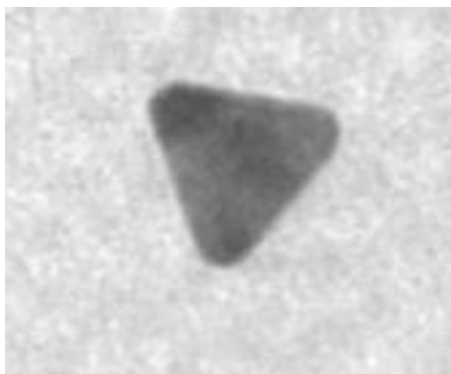
**Figure 1**. Metal nanoparticles can be synthesized in various shapes based on dose rates and growth time. Gold prism ≈ 30 nm in size.
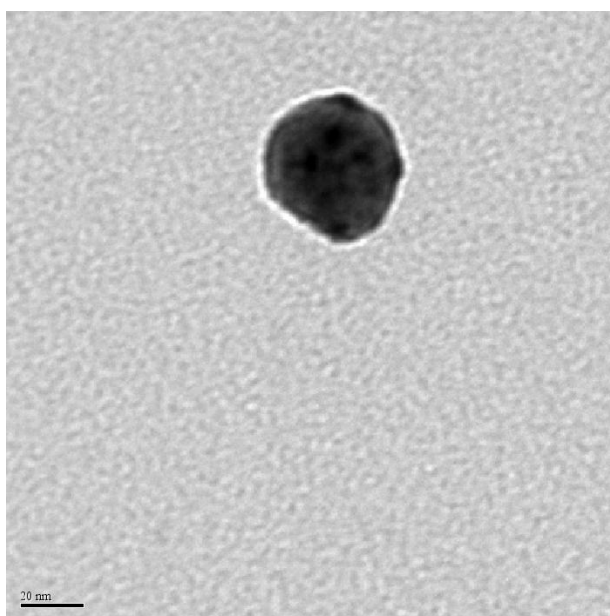
**Figure 2**. TEM of Ag/Ni/polymer cluster. Dark/light contrast in image suggests nanoparticles of elemental difference. Electron diffraction suggests nanodomains of crystallographic difference.
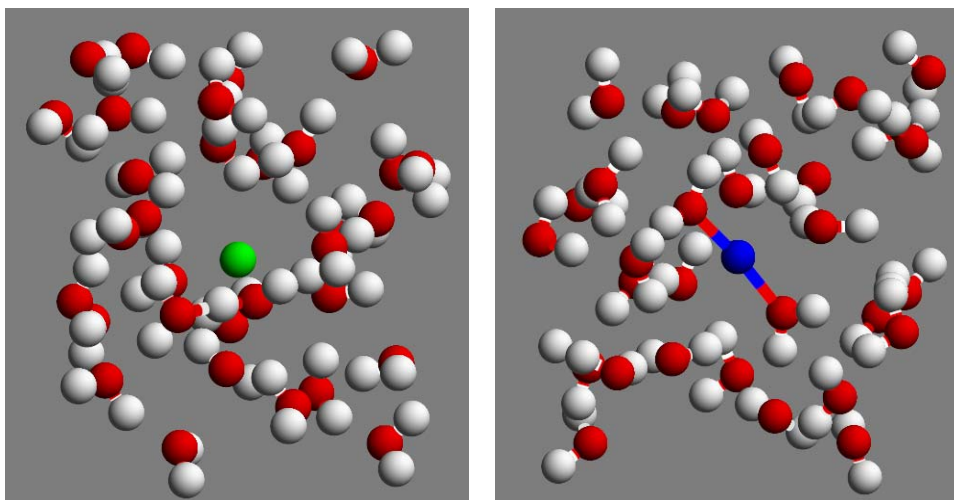


**Figure 3**. Ag/Ni AIMD snapshots of Ag (green) and singlet Ni (blue) atoms in liquid water. The red and white circles in the ball-and-stick models depict the oxygen and hydrogen sites of $H_2O$ molecules.

# *Holey Sheets: Durable Dendritic Platinum Catalysts for Fuel Cells*

## *by* **Y. Song, F. van Swol, J. Miller, and J. Shelnutt**

**M**otivation—Polymer electrolyte membrane (PEM) fuel cells are an energy efficient and environmentally benign energy conversion technology for portable, stationary, and automotive applications. However, the poor durability of fuel cell components such as the membrane electrode assembly (MEA) impedes their successful commercialization. A major factor determining the lifetime of the MEAs is the loss of surface area and thus activity of the platinum-based electrocatalysts. Currently, platinum nanoparticles are supported on electrically conductive materials such as carbon black or carbon nanotubes where they are vulnerable to the processes of corrosion, dissolution, ripening/sintering, and migration and coalescence. The introduction of Sandia-developed methods for nanostructuring the Pt electrocatalyst offers novel new approaches for the enhancement of electrocatalyst stability.

**A**ccomplishment—Recently, we reported nanostructures composed of dendritic platinum sheets, including flat nanosheets, spherical nanocages, nanowire networks, and foam-like nanospheres. We have now found that some of these Pt nanostructures show remarkable stability as electrocatalysts in PEM fuel cells (Fig. 1). Moreover, our studies suggest that the high stability of these dendritic Pt catalysts is due to the formation of persistent nanopores in the sheets. The conversion of the dendritic sheets to holey sheets was found to preserve much of their initially very high surface area. Our experiments and simulations demonstrate that the novel topography of the holey sheets renders them extraordinarily resistant to loss of surface area. Specifically, Monte Carlo simulations (Fig. 2) show that the holey sheets are resistant to sintering, hole migration, and coalescence processes that could drastically reduce surface area. The simulations also elucidate the rapid conversion of the dendritic sheets to holey sheets, with most of the holes having sizes near a critical 3-nm diameter. These holes are persistent, while larger or smaller holes are unstable. TEM images of flat dendritic sheets, taken at 2-minute intervals during heating by the electron beam, verify the predicted stability of the holes that form near the critical size and verify that the conversion from a dendrite to a holey sheet is fast and that the sheet thickness is persistent and near optimum.

An interesting parallel can be drawn between two alternative methods of preventing surface area losses due to sintering and ripening. For supported nanoparticles on carbon, small particles dissolve, allowing larger particles to grow, and resulting in lower surface area. Similar ripening occurs for the holes in nanosheets, but because of their optimum hole size they are metastable and thus preserve surface area. In addition, corrosion at the Pt-carbon interface frees particles to migrate to other particles where they rapidly coalesce, giving a large decrease in surface area. In contrast, holes can migrate and coalesce only by slow diffusion within the Pt sheets.

**S**ignificance—Materials nanoengineering is providing new opportunities for major improvements in conventional technologies such as fuel cells. Our demonstration of the possibility of sintering-resistant morphologies for metal nanostructures offers exciting possibilities for efficient, long-lived fuel cells. The simulations elucidate the principles that lead to such structures and point the way to further improvements and new applications.
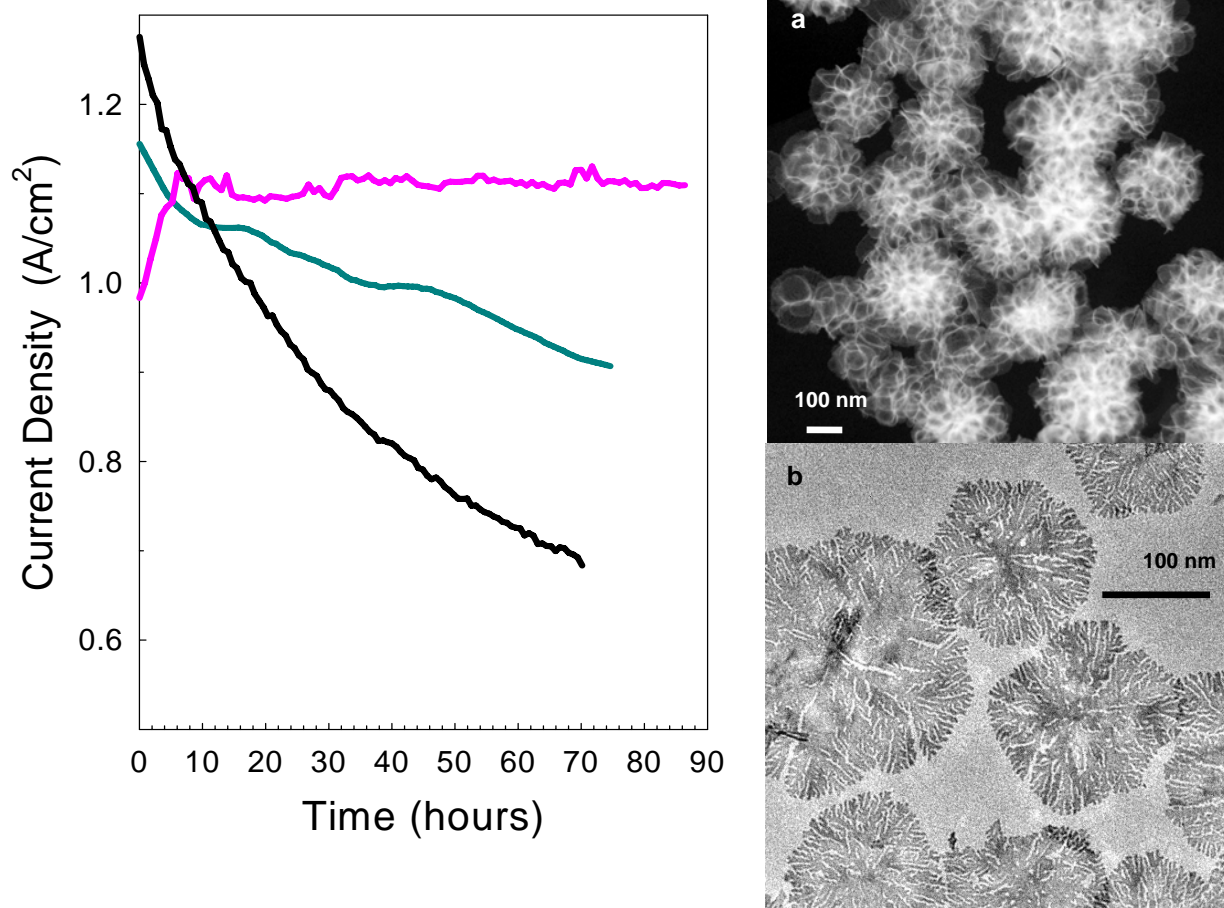
**Figure 1**. Durability tests of MEAs at 0.5 V for the dendritic Pt nanospheres (magenta) shown in (a), nanosheets (cyan) shown in (b), and platinum black (black). Dark field TEM images of the Pt nanospheres (a) and bright field images of the flat nanosheets (b).
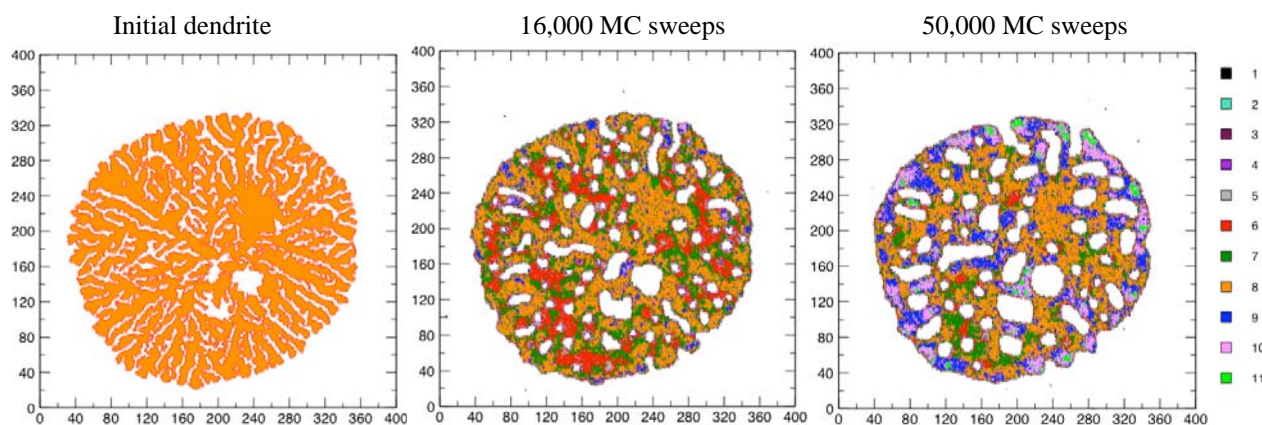


**Figure 2**. Monte Carlo simulations provide color-coded thickness maps of the dendrites that elucidate the dendrite-to-holey sheet conversion and some of the other unique properties of the holey sheet structures such as hole-hole interactions and specific areas of thickening and thinning.

# The Role of Collisions in Aligned Nanowire Growth

*by* **George T. Wang, Qiming Li, and J. Randall Creighton**

**M**otivation—The epitaxial growth of vertical nanowire arrays with controlled properties is of interest for reasons of density, uniformity, anisotropy, coupled interactions, and device integration. However, a population of tilted, non-vertical nanowires is often inevitable due to competition from nanowires with different growth directions (including symmetrically equivalent directions within the family).

**A**ccomplishment—We report here that collisions between tilted and vertical nanowires during growth can have a dramatic impact on the final alignment of nanowire arrays. We previously demonstrated the epitaxial growth of dense, highly aligned arrays of single crystalline, vertical GaN nanowires on unpatterned r-plane $(1\bar{1}02)$ sapphire substrates via Ni-catalyzed metal-organic chemical vapor deposition (MOCVD). Scanning electron microscope (SEM) and transmission electron microscopy (TEM) analysis indicate that the nanowires share a common $[11\bar{2}0]$ growth direction and have aligned facets.

An investigation of the initial growth process indicates that, in addition to vertically aligned nanowires, a significant fraction of tilted nanowires also nucleate, the density of which sharply decreases with growth time. Thus, the vertically aligned growth is not dominant initially but becomes so as the growth proceeds. Interestingly, we were able to observe collisions between tilted and vertical nanowires experimentally during the initial growth period, as shown in Fig. 1. We attribute this decay in the density of tilted nanowires during growth to these collisions with vertical nanowires, which are observed to terminate the growth of tilted

nanowires but not vertical nanowires.

Based on this collision mechanism, we created a Monte Carlo model to simulate the decrease in the density of non-terminated tilted nanowires due to collisions with vertical nanowires. By normalizing the distribution of minimum collision lengths for a tilted nanowire growing in a field of vertical nanowires obtained after 2000 simulations, a decay curve can be plotted to show the percentage drop in non-terminated tilted nanowire density versus nanowire length. Figure 2 shows the tilted nanowire decay curves simulated for nanowire array densities from 0.5 $\mu m^{-2}$ to 80 $\mu m^{-2}$. It is seen that the vertical nanowire density has a very large effect on the collision (decay) rate. At a vertical nanowire density of 1 $\mu m^{-2}$, the model predicts that approximately 90 percent of tilted nanowires are terminated by the time they reach ~5.27 $\mu m$ in length, whereas at a higher density of 80 $\mu m^{-2}$, 90 percent of tilted nanowires are terminated by only ~0.25 $\mu m$ in length. Thus, dense nanowire arrays are especially effective at rapidly filtering out the growth of tilted nanowires. However, the model shows that the effect of collisions is significant even at lower densities.

**S**ignificance—We have found that nanowire collisions play a critical role in the evolution of aligned, vertical epitaxial nanowire growth by terminating the growth of tilted nanowires, as seen for the case of epitaxial GaN growth on r-plane sapphire. A Monte Carlo model developed to simulate the collision process shows that at high nanowire densities, these collisions become a highly effective mechanism for filtering out the growth of titled nanowires, allowing vertical nanowire growth to dominate.

**Contact:** George T. Wang, Advanced Materials Sciences, Dept. 1126
Phone: (505) 284-9212, Fax: (505) 844-3211, E-mail: gtwang@sandia.gov
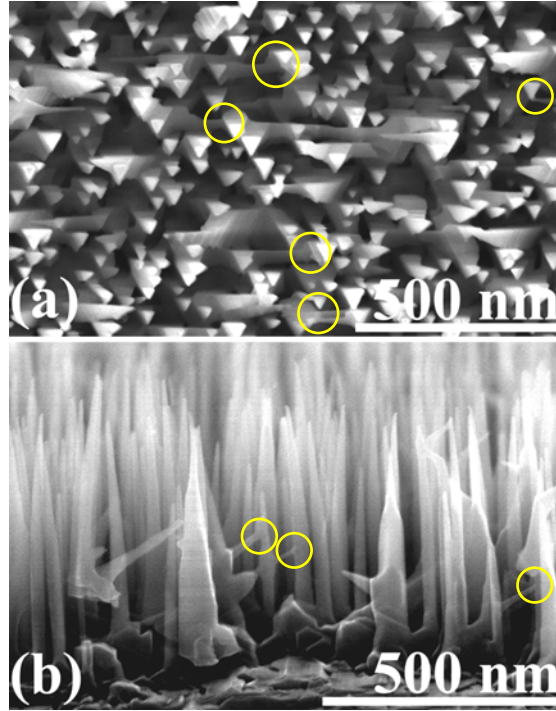
**Figure 1**. (a) Plan-view and (b) cross-sectional view SEM images of aligned, vertical GaN nanowires at 60 s growth. Vertically aligned nanowires appear as triangles with aligned facets in plan-view. Both plan-view and cross-section images capture collisions between tilted nanowires and vertically aligned nanowires (indicated by circles), which terminates further tilted nanowire growth.
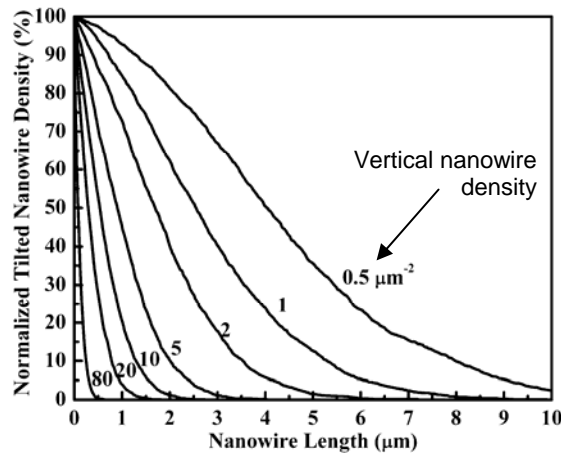


**Figure 2**. A Monte Carlo model shows the decrease of the non-terminated tilted nanowire density as a function of the tilted nanowire length at varying vertical nanowire densities. A high vertical nanowire density, e.g., 80 $\mu m^{-2}$, causes a rapid decrease in the non-terminated tilted nanowire density due to a high nanowire collision rate.

# Broadband Microwave AC Conductance of Silicon Nanowire Arrays

### *by* M. Lee and C. Highstrete

**M**otivation—Semiconductor nanowires are thought to have novel electrodynamic properties that are relevant to both fundamental nanomaterial physics and applications in high-speed electronics and sensors. Recent reports of ballistic transport characteristics in Ge/Si and InAs nanowires suggest that such materials may have extremely fast, very low dissipation microwave response beyond the limit of conventional Drude diffusion-based electronic response. The sensitivity of the DC electrical properties of nanowires to molecules adsorbed on their surface also raises the question of whether similar AC conductance changes exist and can be exploited for chemical sensor purposes. Although there is a large body of research on DC electrical properties, little is known about the microwave electrodynamic response of any type of nanowire. One reason for this is that an individual nanowire presents a very small scattering cross-section to a 1 cm wavelength microwave field, so the interaction between a nanowire and the field usually produces a signal below instrumental background. Extracting the small nanowire signal from the background gives rise to large systematic uncertainties in microwave experiments on single or few nanowires.

**A**ccomplishment—We have successfully measured broadband microwave conductance spectra of silicon nanowires (SiNWs) assembled into arrays spanning the electrode gaps of coplanar waveguides (CPWs). Using a relatively large number of SiNWs and guiding the electromagnetic field using the CPW maximized overlap with the nanowires yielded excellent signal levels and a very high degree of reproducibility. This allowed us to accurately extract the conductance spectra of the SiNWs from the combined CPW/SiNW system across a broad frequency range of 0.1 to 50 GHz.

Doped (n- and p-type) and undoped SiNWs were synthesized by vapor-liquid-solid growth by collaborators at Penn State. Using SiNWs suspended in deionized water or ethanol, arrays consisting of $10^3$ to $10^4$ SiNWs of each doping type were assembled by AC dielectrophoresis (ACDEP) across the electrode gaps of several CPWs (the "test" CPWs) on a wafer, as shown in Fig. 1, while at least one CPW remained bare (the "control" CPW). Using a vector network analyzer, the complex reflection and transmission coefficients on the CPW were measured before and after assembly of the SiNWs. The change in these coefficients was due to scattering and absorption by the SiNWs and was used to deduce their AC conductance as a function of frequency.

The complex AC conductance of the SiNW arrays exhibited a sub-linear power law increase with frequency as shown in Fig. 2. Such frequency dependence is inconsistent with ordinary Drude conductivity, but is consistent with a theory of universal AC transport in disordered electronic systems.

**S**ignificance—This is the first quantitatively reliable and reproducible data on the fundamental AC conductivity properties of any semiconductor nanowire. The finding that the AC conductance is not describable by standard Drude theory and is dominated by disorder is of major importance to both scientific understanding and potential applications of such nanomaterials in high-frequency applications.

**Contact:**   Mark Lee, Semiconductor Material & Device Sciences, Dept. 1123
Phone:  (505) 844-5462, Fax:  (505) 844-1197, E-mail:  mlee1@sandia.gov
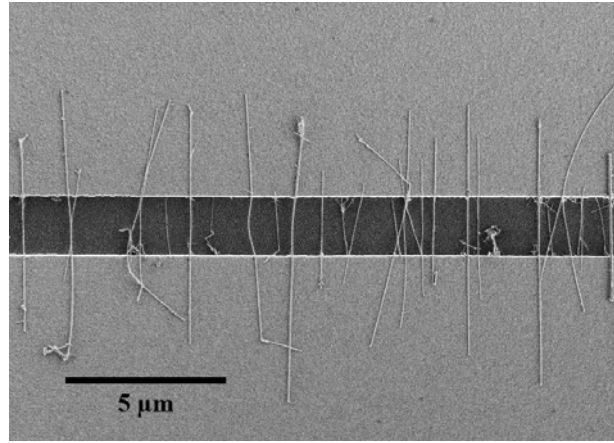
**Figure 1**. Scanning electron microscope image of an array of n[+] doped silicon nanowires assembled via the ACDEP process across the gaps of a broadband microwave co-planar waveguide.
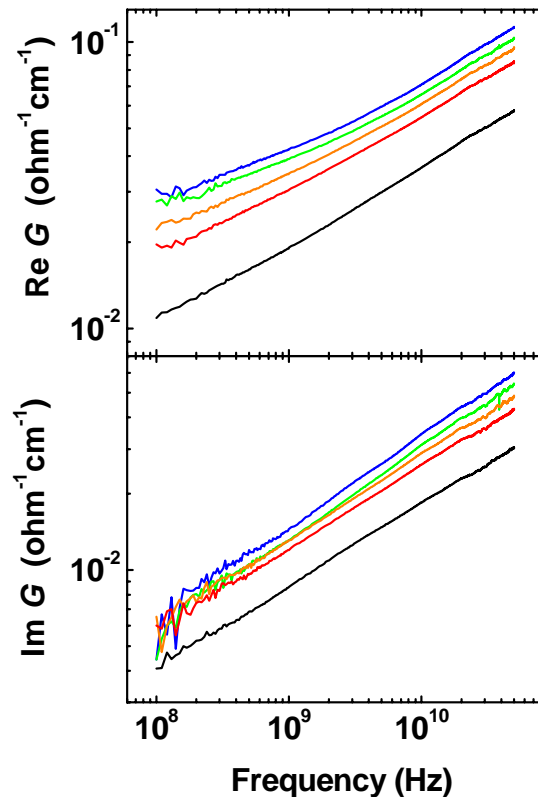


**Figure 2**. Real and imaginary parts of the SiNW array conductance spectrum at several temperatures for an n[+] doped sample. The top four curves are data taken in vacuum of $10^{-5}$ Torr at 4 K (blue), 100 K (green), 200 K (orange), and 293 K (red), from top to bottom. The bottom curve (black) represents data taken at 293 K in atmosphere.

# *Large-Area 3D Nanostructures by Proximity-field nanoPatterning (PnP)*

## *by* **K. H. A. Bogart, I. El-Kady, R. K. Grubbs, K. Rahimian, and F. B. McCormick**

**M**otivation—Three-dimensional (3D) nano-structures are vital for emerging technologies such as photonics, sensors, fuel cells, catalyst supports, and data storage. Conventional fabrication (repeated cycles of standard photolithography with selective material removal) is costly, time-consuming, and produces limited geometries. Unconventional methods (colloidal self assembly, template-controlled growth, and direct-write or holographic lithography) have uncertain yields, poor defect control, small areas, and/or complicated optical equipment. The Proximity-field nanoPatterning (PnP) method overcomes these limitations by generating complex 3D nanostructures using a simple optic and one lithographic exposure and development cycle. The optic is an elastomeric "rubber phase mask" patterned in x, y, and z with dimensions roughly equal to the exposure wavelength. Exposure through this mask generates a complex 3D light intensity distribution due to diffraction (Abbe theory) and the Talbot effect (self-imaging). The underlying photoresist is thus exposed in certain regions, baked, and developed, producing a 3D network of nanostructures with one lithography cycle. Our goal is to scale this method to 150mm and create full models of the process.

**A**ccomplishment—We have developed a model that generates the phase mask required to generate a specific nanostructure. This "inverse" approach is much more complex than the simplistic modeling of the diffraction pattern produced by passing light through a phase mask. The integrated tool starts with a desired pattern and an initial guess on the PnP mask parameters. Next, the interference pattern is simulated using the mask information and filtered to reveal the expected photoresist burn image, which is then evaluated against the desired pattern. An integrated optimizer makes improvements to the mask parameters and cycles again with a simulation using the new mask parameters. The simulation engine is a high performance, OpenMP (Message Passing) parallelized FDTD (finite difference time domain) simulator optimized to run on SMP (shared memory symmetric multiprocessor) systems. Examples of the unique structural images predicted are shown in Fig 1. We have successfully developed the PnP fabrication process and scaled-up the processed area from $490mm^2$ to $>2000mm^2$. We tested photopolymer additives designed to reduce resist shrinkage and identified those compatible with 3D structure generation. We use atomic layer deposition (ALD) to coat the 3D patterned resist with $Al_2O_3$, ZnO (Figs. 2a-b), $TiO_2$, and Pt. We have also generated quasicrystal-patterned phase masks and 3D nanostructures that are interesting for photonics and electronics. We used near-field scanning optical microscopy (NSOM) to characterize the light patterns generated by the quasicrystal phase mask (U. Illinois, NINE) and produced the resist structures here at SNL. An SEM image of the quasicrystal-patterned resist, an image of 532nm light diffracted through this structure, and NSOM images of light intensity at 0.3 µm and 2.4µm above the mask surface are in Figs.2c-f.

**S**ignificance—Fabrication of large-area 3D nanostructures within a single lithography cycle is an important capability for future microsystems.

**Contact:** Katherine H. A. Bogart, Advanced Materials Sciences, Department 1126
Phone: (505) 844-6323, Fax: (505) 844-3211, E-mail: khbogar@sandia.gov
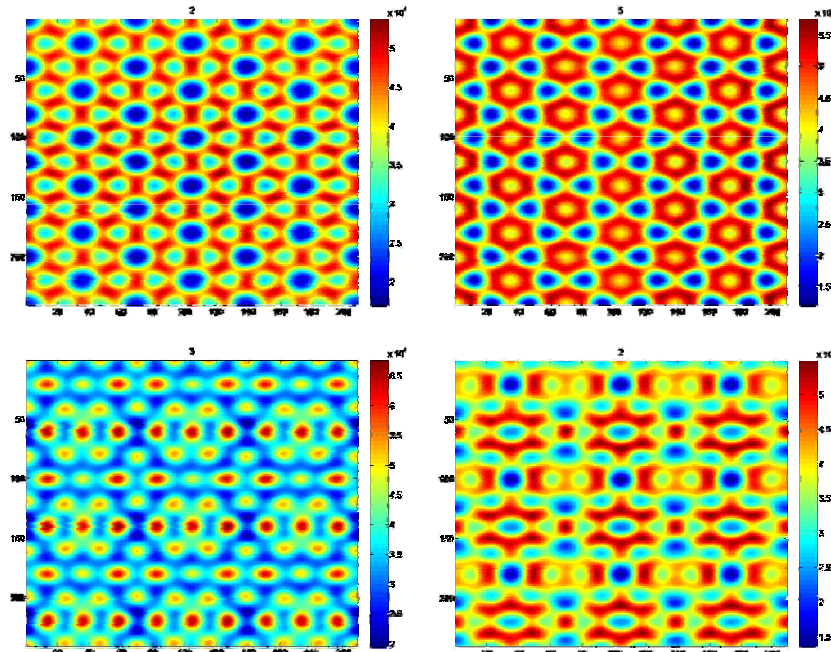
**Figure 1**. Predicted intensity patterns for an hexagonal array of phase mask features showing the burned resist structures (red) and open (developed away) areas (blue).
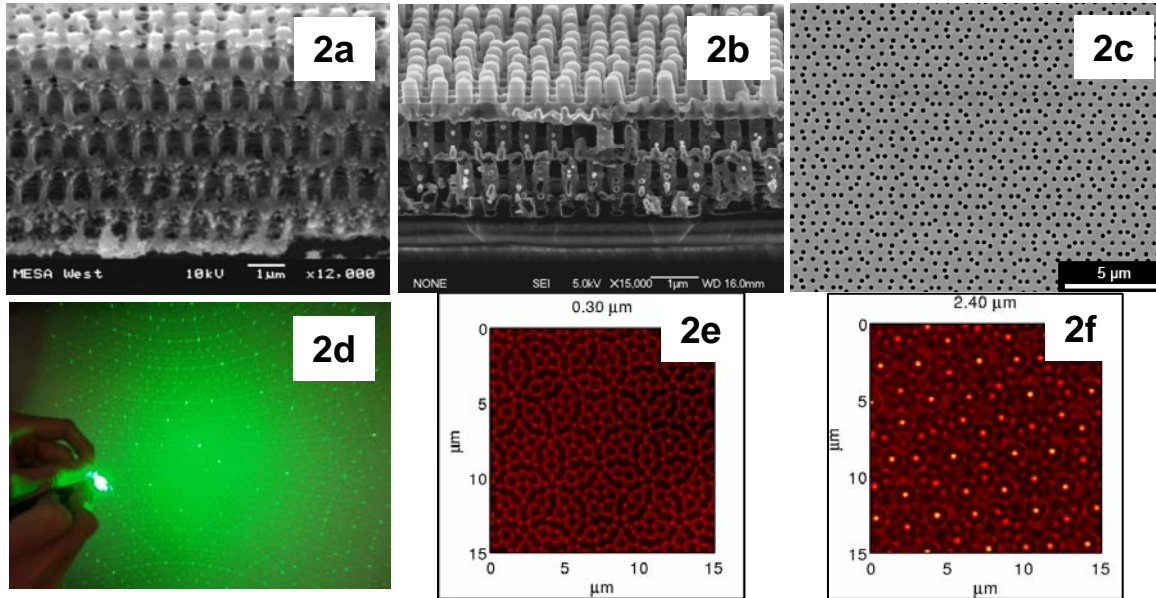


**Figure 2**. SEM image of PnP 3D resist structure (2a), 3D resist structure fabricated in MESA µFab coated with $Al_2O_3$ and ZnO by ALD (2b), SEM image of the quasicrystal-patterned resist (2c), image of 532nm light diffracted through the resist quasicrystal (2d), and NSOM images of light intensity 0.3 µm (2e) and 2.4 µm (2f) above the mask surface

# Compound Semiconductor Materials and Devices

## *Nitride Semiconductor Materials Research in Sandia's Physical, Chemical, & Nano Sciences Center:  Overview*

### *by* **J. Y. Tsao**

**M**otivation—III-V compound semiconductor materials in which nitrogen occupies the column V position have been of intense interest over the past decade and a half.  They promise unique performance: in electronic devices (particularly those driven at high frequencies and high powers); in optoelectronic devices (particularly those spanning the visible and ultraviolet wavelengths); and in micro-optoelectro-mechanical systems (particularly those that require high mechanical strength).

Many aspects of these materials are now understood well enough for active devices to be fabricated and used in commercial and national security applications.  However, many aspects are only now being explored, with the expectation that the span of usefulness for these materials will be expanded significantly: into microwave communications, into solid-state lighting, and into ultra-miniature and ultra-reliable opto-mechanical components.

**A**ccomplishment—Exploration of nitride semiconductor materials is a challenge that requires sophisticated capabilities and expertise in semiconductor epitaxy, nano- and micro-fabrication, materials characterization, optical physics, and device modeling and design. A critical mass of these capabilities and expertise has been developed within Sandia's Physical, Chemical, & Nano Sciences Center, in collaboration with other Sandia organizations.

This critical mass of capabilities and expertise has enabled a number of advances in recent years, the sum of which have led to widespread recognition of Sandia as one of the world's premier laboratories for one of the most important applications for nitride semiconductor materials: solid-state lighting.  Indeed, Sandia was recently named the lead laboratory for the National Center for Solid-State Lighting, as detailed in the Brief by Mike Coltrin and Jerry Simmons.

Many examples of nitride semiconductor materials research could be given.  Some are illustrated in Figure 1; two we report on as Briefs for this year.
.
Dave Follstaedt and co-workers report on the mechanisms underlying a synthesis technique in which AlGaN epitaxy occurs on lithographically pre-patterned GaN material.  This technique has the potential to reduce the density of extended defects, a huge current problem with AlGaN materials and their application to ultraviolet light emitters.   The work made use of semiconductor epitaxy by metal-organic chemical vapor deposition (MOCVD), and materials analysis at the nanoscale through focused ion beam (FIB) sample preparation and transmission electron microscopy (TEM).

George Wang and co-workers report on the mechanisms underlying a synthesis technique in which GaN epitaxy occurs in a dense array of nanowires.  This technique has the potential to eliminate extended defects entirely, and to provide novel one-dimensional geometries for transport and confinement of electrons/holes and for emission of photons.  The work makes use of vapor-solid-liquid (VLS) synthesis of epitaxial nanowires, Monte Carlo simulations, and scanning electron microscopy.

**Contact:**    Jeffrey Y. Tsao, Semiconductor & Optical Sciences, Dept. 1120
Phone:  (505) 844-7092, Fax:  (505) 844-4045, E-mail:  jytsao@sandia.gov
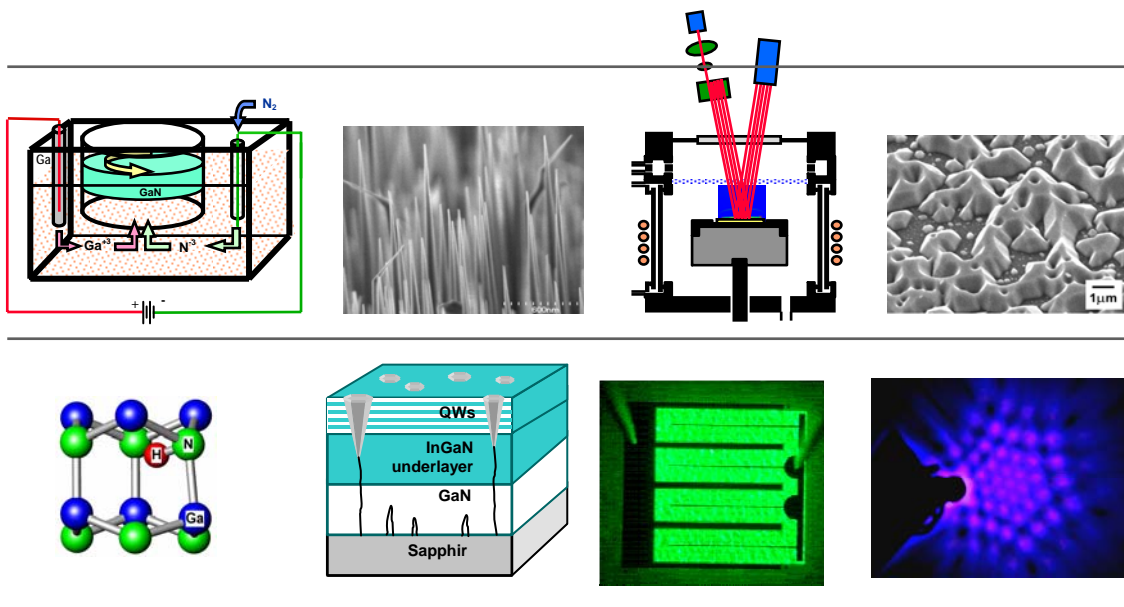
**Figure 1**. Vignettes of research in nitride semiconductor materials at Sandia National Laboratories and in the Physical, Chemical, & Nano Sciences Center. Clockwise from upper left: bulk nitride growth using electrochemical methods; epitaxial nitride nanowires; nitride metal-organic chemical vapor deposition reactor with advanced in-situ optical diagnostics; nanostructurally engineered nitride nucleation layers; photonic lattice light-emitting diode; green light-emitting diode; defect formation during GaN and InGaN epitaxy; and atomic model for H in GaN.

# *National Center for Solid-State Lighting*

*by* **M. E. Coltrin and J. A. Simmons**

**M**otivation—Solid-State Lighting (SSL) uses semiconductor-based inorganic or organic light-emitting diodes (LEDs) to produce white light for general illumination. The Center for Integrated Nanotechnologies (CINT), jointly operated by Sandia National Laboratories and Los Alamos National Laboratory, has been selected as headquarters for the National Center for Solid-State Lighting (NCSSL), with Sandia as lead Lab. The NCSSL is a virtual, multi-lab center which incorporates multiple R&D projects from the five DOE Nanoscale Science Research Centers (NSRCs).

**A**ccomplishment—The purpose of the NCSSL is to stimulate and enable the rapid transition of fundamental nanoscience discoveries into energy efficient SSL technologies. Technical projects for the NCSSL were selected by a competitive proposal process, with Sandia capturing 4 of the 7  (and CINT 5 of the 7) projects awarded in FY07, consisting of:
"Investigation of Surface Plasmon Mediated Emission from InGaN LEDs using Nano-patterned Metal Films," (PI: A. Fischer) to develop a high efficiency LED structure taking advantage of surface plasmons, which are electromagnetic waves at the interface between a metal and dielectric which have demonstrated improve light emission by as much as 90 times in specialized, optically pumped LED structures.

"Nanostructural Engineering of Nitride Nucleation Layers for GaN Substrate Dislocation Reduction," (PI: D. Koleske) to develop growth methods to reduce GaN dislocation densities on sapphire that inhibit device efficiencies. This study will establish the correlation between the nucleus density and dislocation density, then develop methods to reduce the nucleus density — while maintaining the ability to fully coalesce the GaN films.

"Nanowire Templated Lateral Epitaxial Growth of Low Dislocation Density GaN," (PI: G. Wang) to develop decreased defect density GaN substrates enabling higher efficiency LEDs. We will develop growth techniques for GaN nanowires that are then induced to grow laterally and coalesce into a high quality planar film.

"Development of White LEDs using Nanophosphor InP Blends," (PI: L. Rohwer) to develop oxide nanophosphors and semi-conductor quantum dots (QDs) in encapsulants to produce high conversion efficiency white-emission. The ultimate goal of this research is to produce white LEDs containing nanophosphor-QD blends that are superior to LEDs made with QDs or traditional phosphors alone.

**S**ignificance—In the next decade or two, solid-state lighting promises to reach energy efficiencies that are ten times as high as incandescent bulbs and twice as high as fluorescent lamps. If SSL at that efficiency were to replace all the incandescent and fluorescent lamps in the nation, the nation's electrical energy use would fall by 10%. Reaching the ultimate efficiency and cost targets of SSL requires breakthroughs in understanding the nanoscale science of LED materials that the NCSSL seeks to provide.
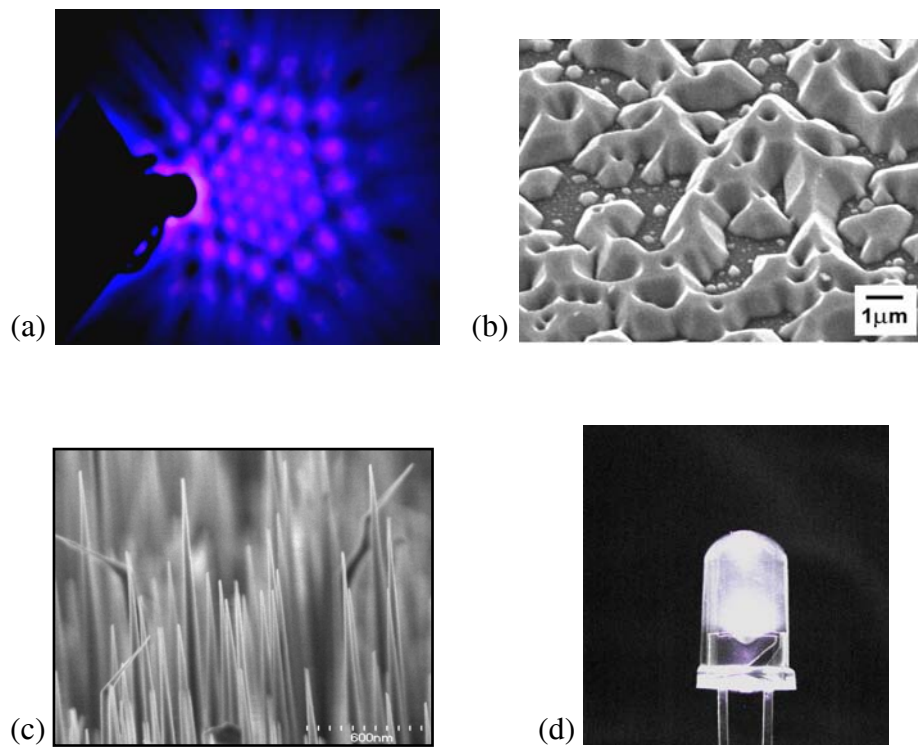
**Figure 1**. Sandia is working on four projects as part of the NCSSL to enhance materials performance at the nanoscale: (a) improving light-extraction efficiencies through surface plasmon creation, (b) improvement of GaN material quality through manipulation of the growth process of the initial nucleation layer, (c) development of arrays of highly aligned GaN nanowires and subsequent coalescence into low defect-density substrates for LEDs, and (d) production of high conversion efficiency white-emission from blends of special nanophosphors.

# Reducing Dislocations in AlGaN Grown on Patterned GaN
*by* **D. M. Follstaedt, A. A. Allerman, S. R. Lee, J. R. Michael,**
**K. H. A. Bogart, M. H Crawford, and N. A. Missert**

**M**otivation—The development of methods to grow GaN with good crystalline quality has allowed this light-emitting semiconductor to be used as a template for laser diodes and light-emitting diodes (LEDs) operating at blue to near-ultraviolet (UV) wavelengths. Alloying GaN with AlN increases its bandgap to give emission further into the UV. Devices emitting at 340 nm are needed to fluoresce biomaterials in order to detect and identify biotoxins. This wavelength requires $Al_xGa_{1-x}N$ alloys with x = 0.25-0.35; however, emission is very weak from such alloys. The high level of dislocation defects ($\sim 10^{10}/cm^2$) in the alloys is widely thought to limit their light output. Therefore, we have examined AlGaN grown on patterned GaN as a method to achieve lower dislocation densities, as suggested in some reports [see Bell, et al., Appl. Phys. Lett. <u>85</u>, 3417 (2004)].

**A**ccomplishment—The substrate pattern used was 10 µm-wide, 1 µm-deep trenches along the [1-100] direction, formed by inductively coupled plasma etching into GaN grown on c-axis sapphire. Growth was done by metal-organic vapor phase epitaxy. A 30 nm-thick AlN interlayer was first grown to strain-relax the subsequently grown $Al_{0.26}Ga_{0.74}N$ alloy and thus prevent its cracking. During growth of AlGaN to 15 µm thickness, the growth was periodically interrupted and the surface examined with scanning electron microscopy (SEM). The images showed that growth proceeded with inclined surfaces emerging from the corners on each side of the trench.

Focused ion beam milling was used to prepare thin cross-section specimens extending down to the sapphire to investigate the growth modes using transmission electron microscopy. Several adjoining sections with different types of growth and distinct microstructures appeared, as seen in Fig. 1. First, on the flat trench bottom, vertical growth occurs with vertical dislocation lines. Second, horizontal growth and disloca- tions emerge from the sidewalls of the trench and intersect the vertical growth. Third, over the horizontal mesa surface next to the trench, growth and dislocations are again vertical.

Fourth, angled-growth sections emerge from the corners of the mesa on each side of the trench. These overgrow the vertical growth from the bottom of the trench. The cross-section image also shows that the surface at the time of a growth interruption contains a tilted section, just as seen with SEM. With continued growth, the two angled growths meet above the trench centerline. Most dislocations in these sections remain within them and are directed toward the center. Figure 2 shows that when the vertical dislocations from the trench bottom contact the angled growth section, they are bent toward the center and are annihilated. These dislocation interactions produce a fifth type of growth with low dislocation density above the angled growths. These two sections on either side of the trench centerline continue to the top surface with a dislocation density of only $\sim 1.5 \times 10^8/cm^2$.

**S**ignificance—Microscopy shows the top surface has low dislocation-density areas 4 µm wide, extending for 10's of microns on either side of the trenches. This indicates that the growth modes and dislocation removal seen in Fig. 1 are typical of this material. These areas are sufficiently wide for UV laser diodes. This growth scheme may therefore become important for producing AlGaN with low dislocation densities as needed for efficient UV light emission.

**Contact:** Andrew A. Allerman, Advanced Materials Sciences, Dept. 1126
Phone: (505) 845-3697, Fax: (505) 844-3211, E-mail: aaaller@sandia.gov

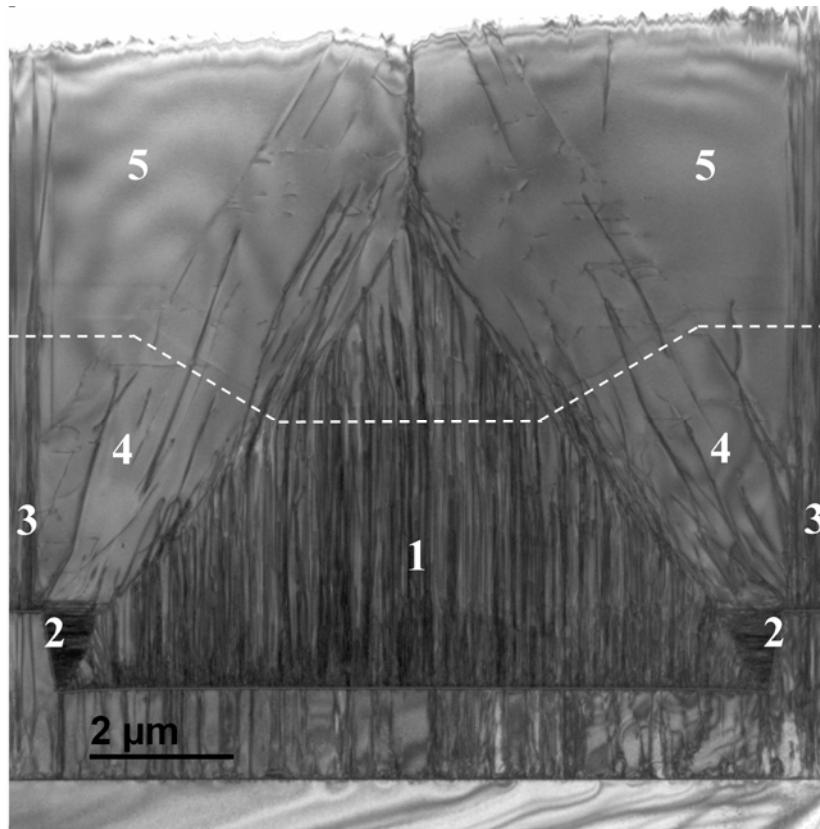**Figure 1**. Cross-section TEM image showing the five growth areas discussed (numbered as introduced in the text) and the interrupted growth surface (dashed line) with tilted sections on each side of the trench.
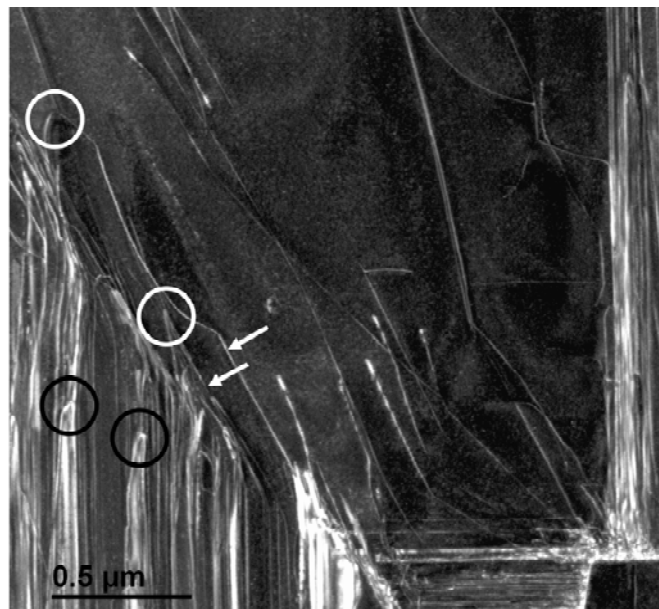


**Figure 2**. Enlarged, weak-beam TEM image from left corner of Fig. 1 showing vertical dislocations bending upon reaching the angled growth section (arrowed) and dislocation annihilations (circled).

# Enhanced Luminescence of InGaN Quantum Wells Grown on InGaN Underlayers

*by* **M. H. Crawford, D. D. Koleske, S. R. Lee, N. A. Missert, D. M. Follstaedt, and K. H. A. Bogart**

**Motivation**—The luminescence efficiency of InGaN quantum well (QW) structures depends on a number of factors that are not well understood. Recently, a dramatic enhancement of the luminescence efficiency of InGaN QWs has been observed with the addition of a lower-growth-temperature $In_xGa_{1-x}N$ epilayer between the QWs and the higher-growth-temperature GaN template layer (Fig. 1a). The focus of this work is to elucidate the mechanisms that drive this luminescence enhancement.

**Accomplishment**—Several hypotheses have been tendered to explain the impact of underlayers on luminescence; we focus here on two prominent examples. First, it has been proposed that underlayers reduce the density of nonradiative recombination centers [Akasaka, *et al.*, APL (2005); Son, *et al.*, Journal of Crystal Growth (2006)]. Second, the low growth temperatures of InGaN underlayers contribute to the formation of hexagonal pit defects ("V-defects") that decorate threading dislocations. Both Takahashi, *et al.* (JJAP (2000) and Hangleiter, *et al.* (PRL (2005) have proposed a novel screening mechanism related to such V-defects that could lead to luminescence enhancement. In the case of Hangleiter, *et al.*, QWs on the inclined facets of V-defects (Fig. 1b) are shown to be thinner, of lower indium composition, and therefore of higher bandgap than basal plane QWs. Thus, V-defects may enable an energy barrier around threading dislocations, preventing carrier capture and nonradiative recombination.

To evaluate these hypotheses, we have grown a number of different blue-emitting InGaN QW-on-underlayer samples and have evaluated their optical and structural properties. Temperature-dependent photoluminescence (PL) shows that QW internal quantum efficiency (IQE) indeed rises when V-defect-containing underlayers are added underneath the QWs (Fig. 1c). The increase in IQE varies from ~2X up to a remarkable ~18X and depends on the underlayer thickness, composition, and layer sequence – even though similar V-defects are present in all samples. To confirm the surprisingly non-dominant behavior of the V-defects, we developed underlayers of similar composition and thickness, but either *with* (Fig. 2a) or *without* (Fig. 2b) V-defects through control of underlayer growth temperature. Comparing the temperature-dependent PL of QWs on these two underlayers with the PL of QWs grown without an underlayer, we see that V-defects actually have *no influence* on the improved IQE (Fig. 2c), refuting the recent V-defect models. We instead see a critical dependence on the presence of indium in the underlayer (Fig. 1c). In addition, scanning cathodoluminescence images (not shown) reveal that the *increase* of luminescence with the addition of indium to the underlayers is relatively uniform across the samples, with no clear spatial correlation to V-defects. These characteristics support a model whereby indium containing underlayers reduce nonradiative centers associated with an underlying point-defect or impurity population.

**Significance**—With direct bandgaps that span the entire visible spectrum, InGaN semiconductor alloys have tremendous potential as efficient light-emitters for solid-state white lighting. The present studies on luminescence mechanisms help provide the fundamental knowledge needed to make this revolutionary, energy-efficient technology a practical reality.

**Contact:** Mary H. Crawford, Semiconductor Material & Device Sciences, Dept. 1123
Phone: (505) 284-9380, Fax: (505) 844-3211, E-mail: mhcrawf@sandia.gov
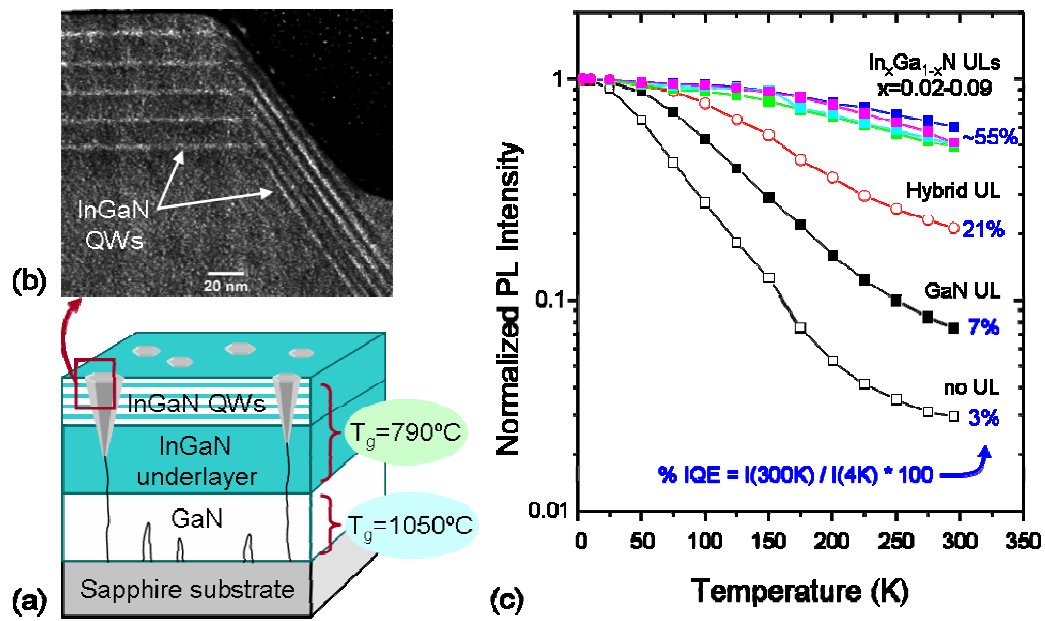
**Figure 1.** (a) Schematic diagram of an InGaN QW structure with an InGaN underlayer; (b) Z-contrast STEM image of the upper corner of a V-defect showing InGaN QWs on the inclined facets of the V-defect pit; (c) temperature-dependent photoluminescence of blue-emitting InGaN QWs grown on 200-nm-thick underlayers of varying indium composition. The hybrid underlayer (UL) is a 180-nm-thick GaN/ 20-nm-thick $In_{0.02}Ga_{0.98}N$ bilayer. Internal quantum efficiency (IQE) is defined as the ratio of integrated PL intensity at 300K and 4K. All underlayers shown are grown at 790 ℃ and have V-defects decorating threading dislocations.
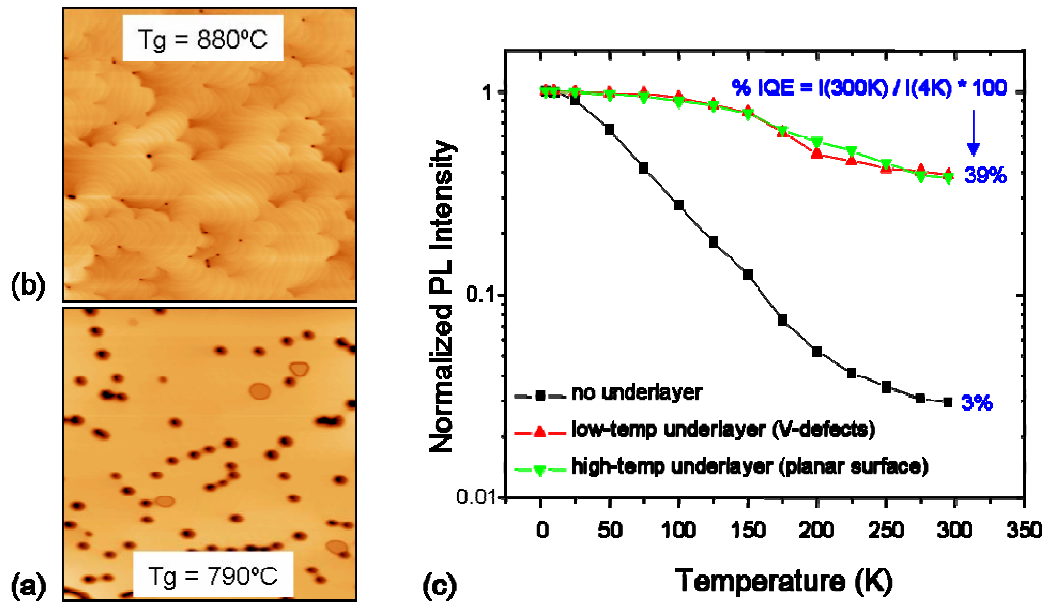


**Figure 2.** 3 μm x 3 μm atomic force microscopy (AFM) images of 200-nm-thick $In_{0.02}Ga_{0.98}N$ underlayers grown at (a) 790 ℃ to induce V-defect formation, or at (b) 880 ℃ to induce a more planar surface with no V-defects; (c) temperature-dependent photoluminescence of blue-emitting InGaN QWs grown on these underlayers compared to QWs grown directly on high-temperature-grown GaN without an underlayer.

# Mid-Infrared Doping-Tunable Extraordinary Transmission from Sub-Wavelength Gratings

*by* **E. A. Shaner, J. G. Cederberg, and D. Wasserman (Princeton University)**

**M**otivation—It has been known for some time that metallic gratings formed on dielectrics can exhibit unique transmission properties. More recently, Ebbessen et al., studied such structures and demonstrated the phenomenon of extraordinary transmission (ET), where, at certain wavelengths, more light passes through the sample than predicted by aperture theory. This effect has been ascribed to surface plasmon (SP) enhancement of the transmission process. There has been significant interest in utilizing such structures for a variety of photonic devices, the majority of which are designed to function in the visible and near-IR.

**A**ccomplishment—We have demonstrated doping tunable extraordinary transmission from sub-wavelength apertures in a periodic two-dimensional metallic grating deposited upon n-doped GaAs. A general expression for the SP resonance condition is given by:

$$\lambda = a_0 \sqrt{\frac{\varepsilon_s \varepsilon_m}{\varepsilon_s + \varepsilon_m}} \approx a_0 \sqrt{\varepsilon_s} \text{ for } |\varepsilon_m| >> |\varepsilon_s| \quad (1)$$

Here, $\lambda$ is the free space wavelength, $a_o$ is the grating period, $\varepsilon_s$ is the real part of the dielectric constant of the semiconductor, and $\varepsilon_m$ is the real part of the dielectric constant of the metal. For commonly used metals in the mid-IR, the condition $|\varepsilon_m| >> |\varepsilon_s|$ holds, allowing the approximation to be used. A typical grating structure is shown inset in Fig. 1.

The free electrons in bulk semiconductors can exhibit well known collective charge oscillations, or plasmons, where the natural resonance frequency ($\omega_p$) is directly proportional to the carrier concentration. For semiconductors the background dielectric function can be tuned by varying the free-carrier density. Neglecting scattering, the frequency dependent effects of free-carriers can be incorporated into the dielectric function of the semiconductor using:

$$\varepsilon(\omega) = \varepsilon_s \left(1 - \omega_p^2 / \omega^2 \right) \quad (2)$$

Figure 1 displays the frequency dependent dielectric function for various doping concentrations in GaAs. A vertical line drawn on Fig. 1 at a wavelength of 8 μm (the design wavelength for the structures studied in this work) shows the large dielectric contrast obtained as the carrier concentration varies by more than an order of magnitude. By coupling the ET and the doping tunable dielectric function we have demonstrated wavelength tunability in the mid-infrared of ~23 cm^{-1}, or approximately 0.15μm, around the 8 μm design wavelength. We have achieved transmission peaks as narrow as 17 cm^{-1}.

**S**ignificance—The tunablity and narrow linewidth of the transmission peaks suggests that such gratings could be used in external cavity structures for Quantum Cascade laser systems. Such systems would have applications in chemical and biological sensing. The sensitivity of the device to the carrier density suggests that electrically tunable grating structures should be possible, enabling tunable filters or modulators for mid-infrared applications. Surface plasmon gratings also have the potential for amplifying chemical IR signatures as molecules adsorb onto metal surfaces.
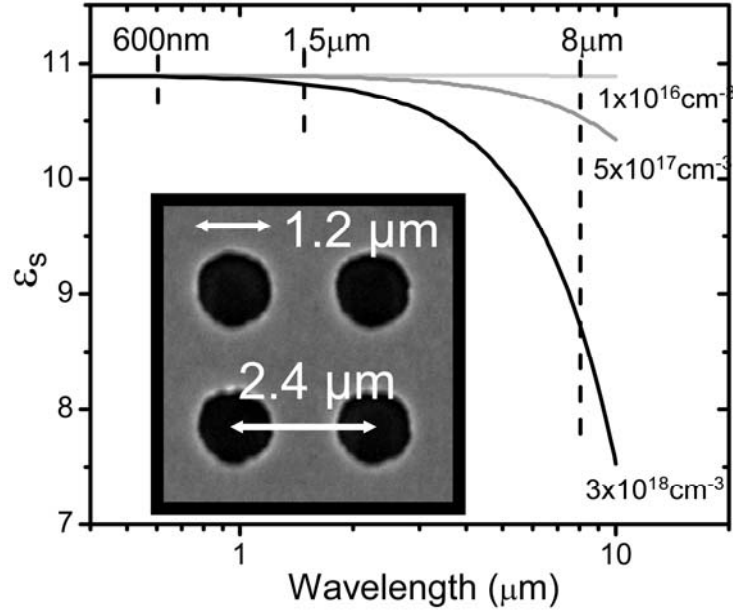
**Figure 1**. The dielectric function of GaAs has large free-carrier variation in the mid-infrared. Inset: Scanning electron micrograph of an extraordinary transmission grating structure. The grating period is 2.4 μm, and the individual hole diameters are 1.2 μm.
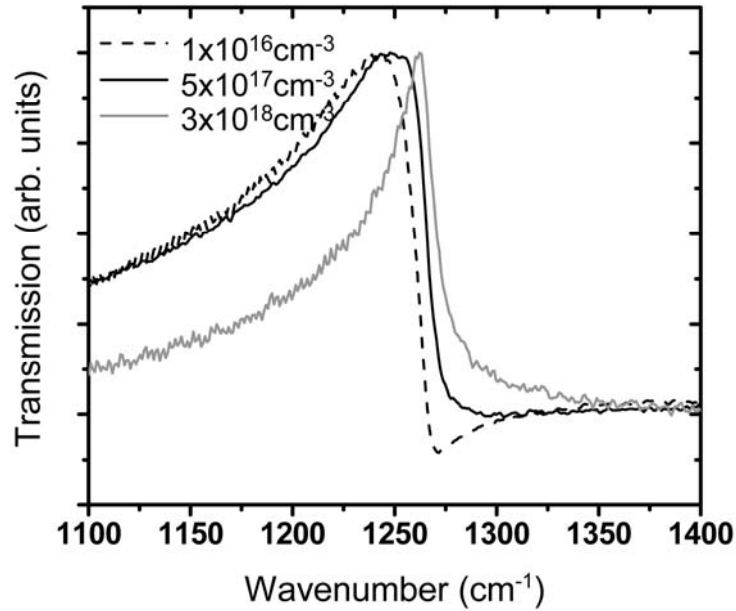


**Figure 2**. Unpolarized transmission spectra for all three samples at normal incidence. The transmission peaks show a distinct shift as the doping of the epitaxial layer increases.

# *Electrically Pumped InAs Quantum Dot Mid-IR Emitters*

*by* **E. A. Shaner, J. G. Cederberg, S. K. Lyo, and D. Wasserman (UMass Lowell)**

**M**otivation—Quantum Cascade Lasers (QCLs), the product of *Band Gap Engineering*, have been revolutionary in transforming the mid-infrared (mid-IR, 3μm - 12μm) into an accessible region for semiconductor based sources. These have seen continuous improvement in power, wavelength coverage, and operating temperature. One way to further expand the capabilities of semiconductor mid-IR semiconductor sources is to use self assembled quantum dots (SAQDs) as the active region in place of the quantum wells. The possible advantages of doing so are increased efficiency and the potential for devices that can naturally emit light normal to the growth direction.

**B**ackground—For many years, InAs SAQDs have been noted to have desirable optical properties due to their atomic-like quantum states (0D density of states). However, in the mid-IR, we have yet to see useful light emitters utilizing SAQDs even though quantum well (2D density of states) QCL technology has progressed rapidly. The primary reason for this gap is the lack of knowledge pertaining to engineering SAQD electronic states in a manner analogous to that employed in QCLs.

In QCLs, injector and collector filter stages are used to pump conduction electrons into custom designed active regions where photons are emitted. Engineering of an injector stage can provide current injection into an upper (p) SAQD state; however, to increase the likelihood of an optical transition, the lower (s) SAQD states must be depopulated faster than p-states. This situation is readily achieved in QCLs, however, the key difference between QCL and

SAQD based devices is the nature of electronic tunneling (2D-2D as opposed to 0D-2D). To succeed in creating electrically pumped SAQD active material, the understanding of this 0D-2D tunneling must be developed.

**A**ccomplishment—Our initial approach to creating mid-IR SAQD devices was to tunnel electrons into bulk semiconductor material (3D density of states). We had hoped to use the matrix of semiconductor material surrounding the dots and wavefunction distributions of excited and ground SAQD states to control the tunneling times. Theory determined that this situation was untenable using any reasonable combination of materials. As a result, the 0D-2D tunneling problem was reopened. We found that, by properly designing injector and filter stages and understanding the momentum selection rules introduced by using SAQDs, it was possible to create the condition where the s-state of the dot could be depopulated faster than the p-state (simplified and shown in Fig. 1). Light emission tests of the materials based on these principles showed significantly improved characteristics over previous designs, and one iteration emitted mid-IR light at room temperature (Fig. 2).

**S**ignificance—By varying the injector and collector stages in electrically injected SAQD material, and seeing significant changes in both I-V characteristics and light emission, it is now known that we are controlling the tunneling in and out of SAQDs. Once useful mid-IR SAQD material has been developed, through improved understanding of the processes involved, we see a path towards efficient, arrayable, wavelength tunable surface emitting devices.

---

**Contact:** Eric A. Shaner, Semiconductor Material & Device Sciences, Dept. 1123
Phone: (505) 284-5356, Fax: (505) 844-1197, E-mail: eashane@sandia.gov
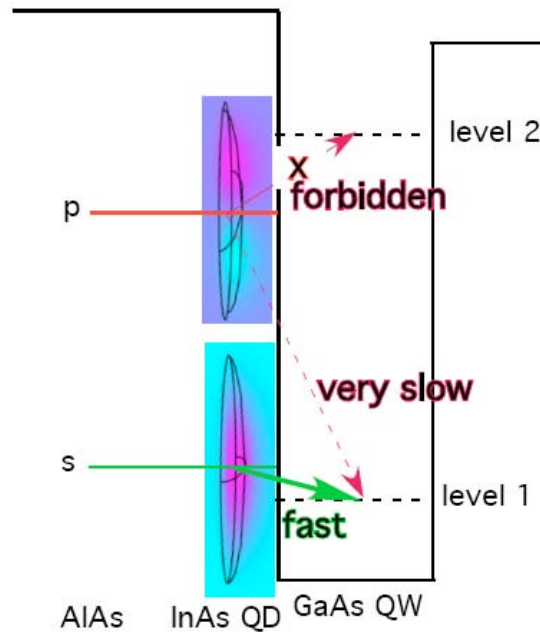
**Figure 1**. Conceptual diagram of the energy level structure desired for efficient depopulation of the s-state and tunneling blockage from the p-state. The energy level of the s-state should be slightly higher than the tunneling state (level 1), while the p-state should be energetically below level 2. For s-tunneling, the excess "vertical" energy is dissipated into the lateral 2D motion in the QW with the 2D momentum less than the momentum uncertainty determined by the QD size. Energy conservation prohibits p-tunneling. This differs from the approach of QCL engineering where an envelope approximation and energy level alignment are primarily considered.
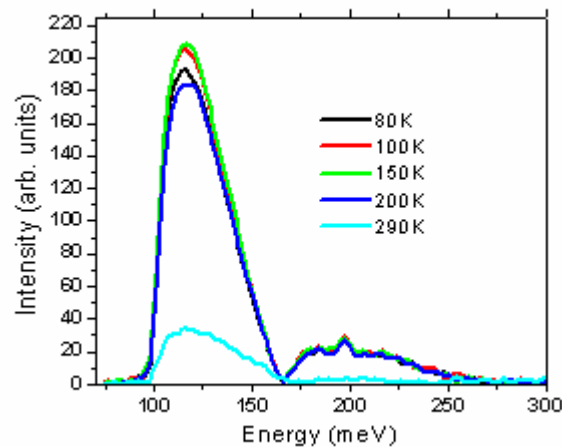


**Figure 2**. Electrically pumped emission from newly designed SAQD material. The conduction electron excited (p) to ground (s) state transition is centered around 10μm wavelength (120meV). Relatively strong emission is observed up to a temperature of 200K, and emission persists to room temperature.

# *High Temperature Quantum Cascade Lasers*

## *by* **I. Waldmueller, M. C. Wanke, and W. W. Chow**

**M**otivation—Quantum cascade lasers (QCLs) and the underlying physics of intersubband quantum-well transitions have been intensely investigated during the last decade. More recently, significant focus has been on the development of QCLs in the THz regime, because of important spectroscopic applications, including several involving homeland security. The present operating temperature for THz QCLs is below 150 K for continuous-wave (cw) operation. The low operating temperature is necessary to mitigate carrier thermalization effects, which are more detrimental to lasing when subband energy separations correspond roughly to that of a THz photon. Clearly, higher temperature operation is required for practical THz QCL applications.

**A**ccomplishment—We have analyzed an optically-pumped electrically-driven quantum cascade laser (OPED) as an approach for THz generation. The scheme involves four quantum-well subbands (Fig. 1). A mid-IR laser field excites electrons from levels 1 to 2. The THz photon is created by transition 2-3, and its energy is derived from a forward electrical bias as in a conventional QCL. Lastly, the mid-IR pump field is coherently recovered via transition 3-4. Calculations based on a microscopic semiconductor laser theory show high optical conversion efficiency for temperatures up to 300 K (Fig. 2). The predicted efficiencies can exceed the Manley-Rowe quantum limit, with as much as a 1:3 mid-IR to THz photon conversion ratio. The study also uncovered interesting physics: the presence of quantum coherence which significantly reduces the threshold requirement for coherent THz generation.[1]

**S**ignificance—The OPED approach can be both a promising source for THz generation at high temperature and a practical experimental platform for studying and engineering quantum coherence effects such as electromagnetically induced transparency (EIT), lasing without inversion (LWI), and group-velocity reduction (slow light).

**Contact:**    Weng Chow, Semiconductor Material and Device Sciences, Dept. 1123
Phone:  (505) 844-9088, Fax:  (505) 844-3211, E-mail:  wwchow@sandia.gov
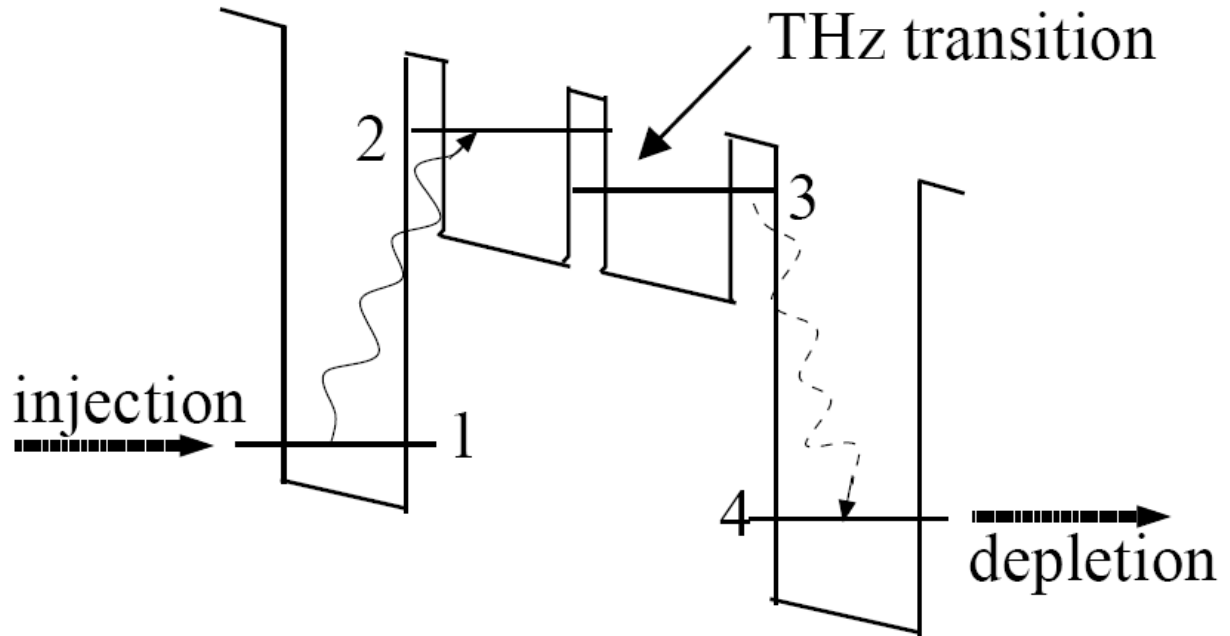
**Figure 1**: Single stage of proposed optically-pumped electrically-driven QCL. Without pump recovery (dashed transition), the scheme reverts to a conventional THz optical conversion configuration.

# Physical and Chemical Sciences

## *Development of THz Photomixing Spectrometer for Gas Phase Spectroscopy*

*by* **K. M. Fortier, T. A. Barrick, and I. Brener**

**M**otivation—In the rapidly developing Terahertz (THz) region of the electromagnetic spectrum, from 100 GHz to 10 THz, there is need for tunable, compact and spectrally narrow sources that operate at room temperature. Conventional THz sources produce discrete frequencies of radiation and often require cryogenic temperatures and/or a large physical footprint to operate. Conversely, a photomixer THz source can be constructed of compact, inexpensive diode lasers that provide a narrow source of tunable THz radiation and operate at room temperature.

An important application of THz is the spectroscopic identification of molecules. A photomixing based spectrometer can achieve frequency resolution of ~ 1 MHz, making it approximately 1000 times more sensitive than time domain spectrometers which are the workhorses of THz spectroscopy. With this increased resolution, compact design, and frequency flexibility, a spectrometer based on THz photomixing is an important tool for identification of explosives, biological pathogens, and other signature applications that are of national interest.

**A**ccomplishment—We have developed a compact THz spectrometer to perform gas phase spectroscopy that is completely contained on a 2' x 4' portable optical breadboard. This THz source is based on the principal of optical heterodyning in which two lasers with different frequencies are spatially overlapped on a beam splitter, generating a beatnote at the difference frequency. Stabilizing the frequency of one laser to an atomic reference, the output beatnote can be tuned by changing the frequency of the second laser with respect to the first. In this configuration, THz radiation can be generated between 0 – 2THz, limited only by the bandwidth of the THz emitter.

The experimental setup can be seen in Fig. 1, where the heart of the spectrometer is two external cavity diode lasers which are coupled to the same single mode optical fiber to ensure spatial overlap. At the output of the fiber the lasers are tightly focused onto a THz emitter structure using a 20x microscope objective. The beatnote modulates the conductance of the emitter, producing continuous wave THz radiation which is coupled to free space via a Si lens. After a sample region, the THz beam is focused onto a Golay cell which detects the THz radiation.

Figure 2 depicts the output spectrum of the THz photomixer. The black curve is the output of the emitter in a nitrogen purged environment with relative humidity of 0.2%. The blue curve depicts the emitted radiation in ambient conditions with 45.0% relative humidity. The absorptions are due to well documented water lines. This initial measurement of the water vapor spectrum has been used to calibrate the system, and future work will focus on measuring spectrum of other molecules in the gas phase.

**S**ignificance—The THz photomixing spectrometer provides a system to measure high resolution spectra of molecules. This system adds a flexible, tunable source of THz that can be used throughout Sandia's developing THz research program.

**Contact:** Kevin M. Fortier; Lasers, Optics, & Remote Sensing, Dept. 1128
Phone: (505) 844-4206, Fax: (505) 844-5459, E-mail: kfortie@sandia.gov
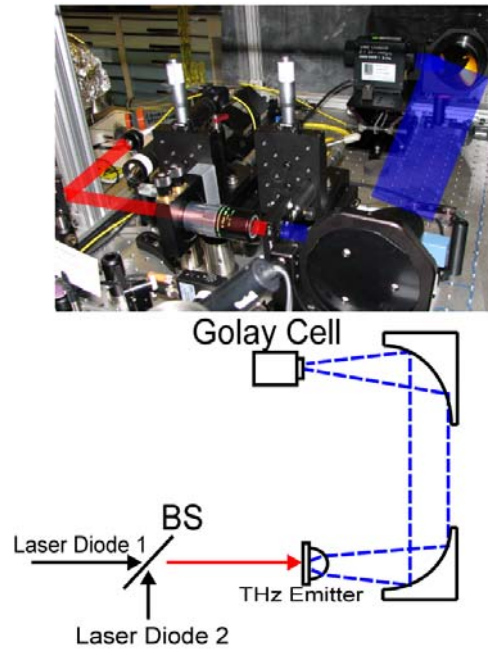
**Figure 1**. A schematic for generating THz radiation via photomixing. Two laser diodes are combined on a beam splitter and then focused onto a THz emitter. The emitted beam is collimated for 20 inches before it is refocused onto a Golay cell detector. A photograph of the experiment where the paths of the lasers that generate the THz beatnote are highlighted in red and the emitted THz beam is highlighted in blue.
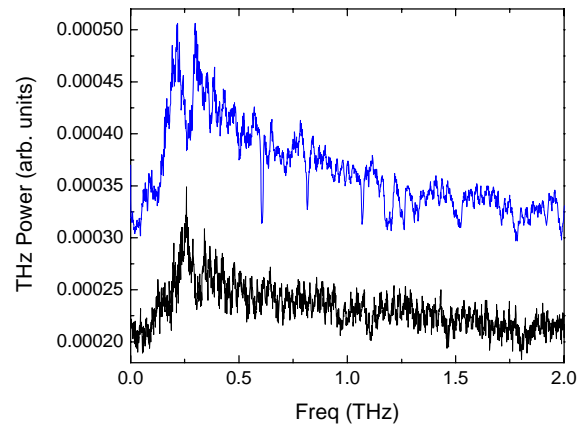


**Figure 2**. Water vapor spectrum measured by the THz photomixing spectrometer. The black curve shows the output of the THz emitter which can generate radiation from 0 to 2 THz. This spectrum was measured in a nitrogen purged environment that removes water vapor. The blue curve shows the spectrum measured in ambient conditions of 45 % RH where water vapor absorbs the THz. For clarity the spectra are offset.

# On the Structure of Magnetized Sheaths in Radiofrequency Discharges

*by* **E. V. Barnat and P. A. Miller**

**M**otivation—Reactive ion etching is a critical process employed in the manufacturing of semiconductor devices. Etching of various materials occurs via a combination of chemical and physical processes on a surface being etched. Considerable effort is made to independently control both the excitation of species in the plasma and the energetics of the species extracted from the plasma to the surface being processed. One such method to do just this is through the application of a magnetic field to the discharge.

**A**ccomplishment—In recent studies, we examined the impact a magnetic field has on the behavior of an rf discharge similar to those employed in etching applications. Particular emphasis was placed on how the magnetic field influences the distribution of electric fields in the discharge and how changes in the electric fields influenced the excitation in the discharge.

A pair of coils, placed in a Helmholtz configuration generated magnetic fields across a discharge region generated by a 100 mm diameter electrode driven at 13.56 MHz. Laser induced fluorescence-dip spectroscopy, a two laser technique, was used to spatially and temporally measure the electric fields present in the discharge. Figure 1 compares the spatial structure and temporal evolution of these electric fields for the case with no applied magnetic field (0 gauss) and for the case with applied magnetic field (120 gauss). Without an applied magnetic field, the electric fields present in the sheath have peak values approaching 700 V/cm, and the spatial extent of the sheath extends more than 5 mm above the powered electrode (defined as a height of 0 mm). On the other hand, when a magnetic field is applied to

the discharge, peak electric fields approach 1400 V/cm (twice that of the unmagnetized sheath) while the spatial extent of the sheath is only about 3 mm above the electrode. Furthermore, during the portion of the rf phase in which the electric fields above the powered electrodes are small, a second sheath forms above the grounded electrode (22 mm above the powered electrode).

The distribution of argon excited into the $1s_5$ state (measured by laser-induced fluorescence) in planes parallel and perpendicular to the magnetic field are shown in Fig. 2 for increasing magnetic field strength. While some change in the distribution is observed in the "North-South" plane parallel to the magnetic field, considerable change in the distribution of excitation is observed in the "East-West" plane. In particular, the plasma becomes skewed with an augmentation in the direction of $\mathbf{E} \times \mathbf{B}$ (East to West). Furthermore, at higher magnetic fields an additional region of excitation becomes evident just below the grounded electrode, consistent with the higher voltage sheath observed in Fig. 1.

**S**ignificance—The coupling between the plasma and a given surface are moderated by the electric fields that are (mostly) present in the sheath. Various 2-D models present in the literature have predicted behavior of the electric fields different from those measured here. The differences may stem from treating a 3-D system with a 2-D model, which suggests that different models may be needed to accurately capture the impact of magnetic field on the structure of the rf discharge.

**Contact:** Edward V. Barnat; Lasers, Optics, & Remote Sensing, Dept. 1128
Phone: (505) 284-9828, Fax: (505) 844-5459, E-mail: evbarna@sandia.gov
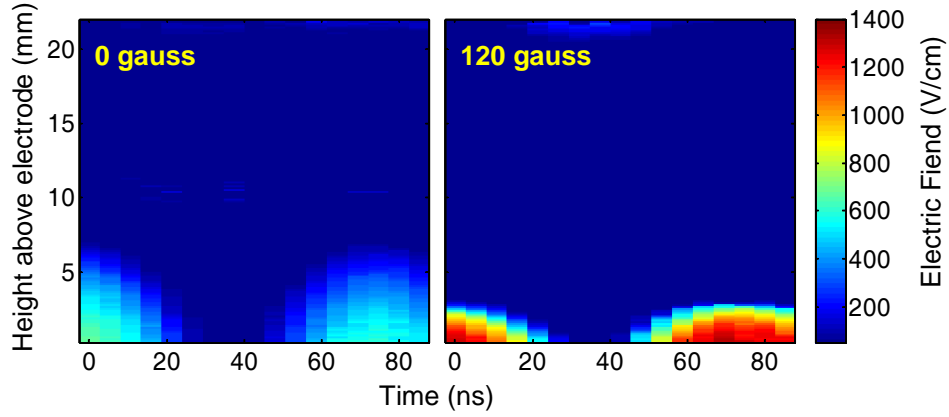
**Figure 1**. Spatial and temporal evolution of electric fields over an rf cycle in the center of the discharge for a 0 gauss case (left image) and a 120 gauss image. Not only does the sheath collapse at higher magnetic field, but a second sheath forms below the grounded electrode.
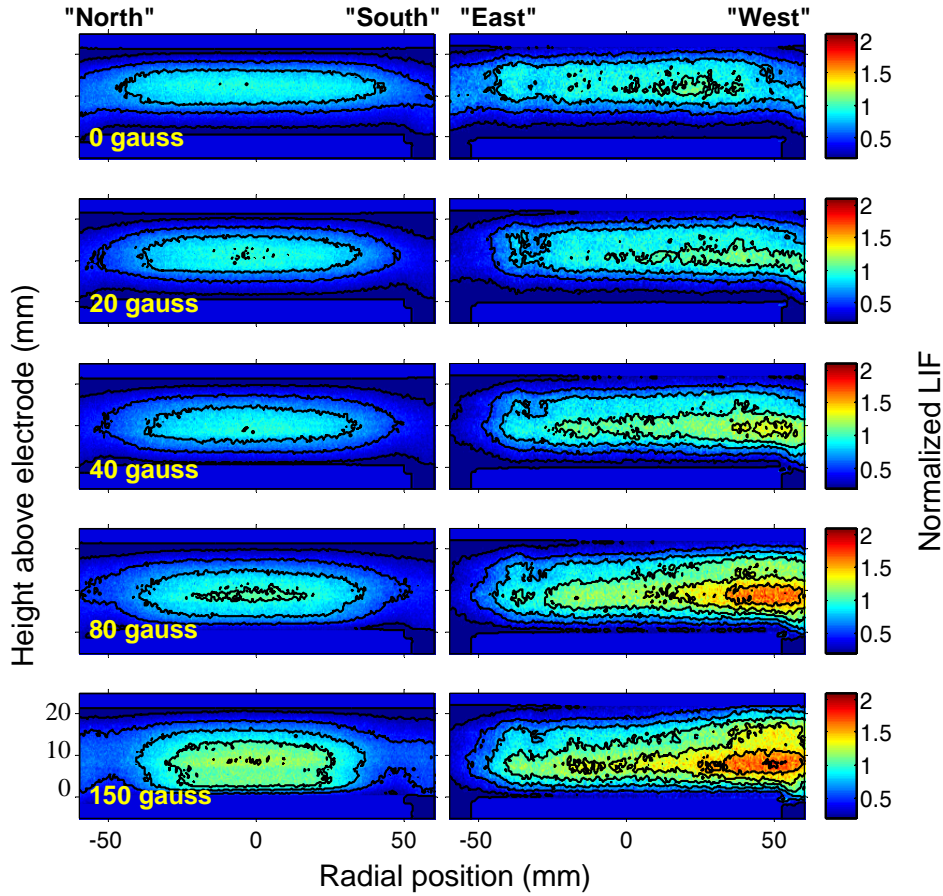


**Figure 2**. Spatial distribution of argon excited in the $1s_5$ state as measured by laser-induced fluorescence in a plane parallel to the magnetic field ("North"-"South", left) and a plane perpendicular to the magnetic field ("East"-"West", right) for various magnetic field strengths.

# *Stress Gradients in Annealed Tetrahedral Amorphous-Carbon Films*

## *by* T. A. Friedmann and J. P. Sullivan

**M**otivation—We have fabricated simple tetrahedral amorphous-carbon (ta-C) Micro-ElectroMechanical Systems (MEMS) devices where the components were made wholly from ta-C – not just as a coating. One critical issue in materials for MEMS technologies is out-of-plane bending caused by stress gradients through the thickness of the device. Indeed, we have found that released ta-C devices can show out-of-plane bending for films that have zero average biaxial stress. This indicates that non-zero stress gradients are embedded in ta-C films. Yet, little is known about the origin of these stress gradients and how to control them. These gradients cannot be measured during growth because the final stress state is determined by a post-growth anneal. Furthermore, the through-thickness stress profile may be nonlinear due to nonuniform processing conditions and/or intrinsic interfacial stresses.

**A**ccomplishment—We have integrated a laser based wafer curvature technique (Fig. 1) into a commercial etch tool to record continuous measurements of curvature versus etch time. Stress gradients were measured during etch-back of as-grown as well as annealed (stress relieved) ta-C thin films deposited by pulsed-laser deposition. Figure 2a shows a representative data set for an annealed sample. The curvature data were converted into average and instantaneous stress curves versus thickness (Fig. 2b), assuming that the etch rate was linear with time.

The as-grown compressively stressed films display a uniform, constant (~6 GPa) stress profile (not shown) through the bulk of the film. At the silicon interface, the stress increases quickly from zero to the bulk value, but at the film surface there is a thin layer (~20 Å) with a large tensile (5-10 GPa) stress.

The data for the annealed film (Fig. 2a) show a complicated stress profile, even though the nominal in-plane average stress is near zero (no net change in curvature from start to finish in Fig. 2a). The bulk film stress is actually 78 MPa tensile, the silicon/ta-C interface is in compression (1 – 5 GPa), and the ta-C growth surface remains in tension (5-10 GPa). Clearly, the stress relaxation dynamics (that relieves the bulk film stress) are not the same at the silicon interface and the top surface of the film. Annealing relaxes the stress near the Si interface only partially and has almost no affect on the surface tensile stress.

**S**ignificance—The information we have obtained on stress gradients in ta-C thin films now allows us to control out-of-plane bending in released devices, mainly by depositing compensating stressed layers on devices. This technique is generally useful for other materials systems where knowledge of stress gradients is important.

For ta-C thin films, it has been generally known that the surface layer is not the same as the bulk due to the growth energetics. Molecular dynamics simulations of film growth have predicted a tensile surface layer. We have now provided the first experimental confirmation of that result.
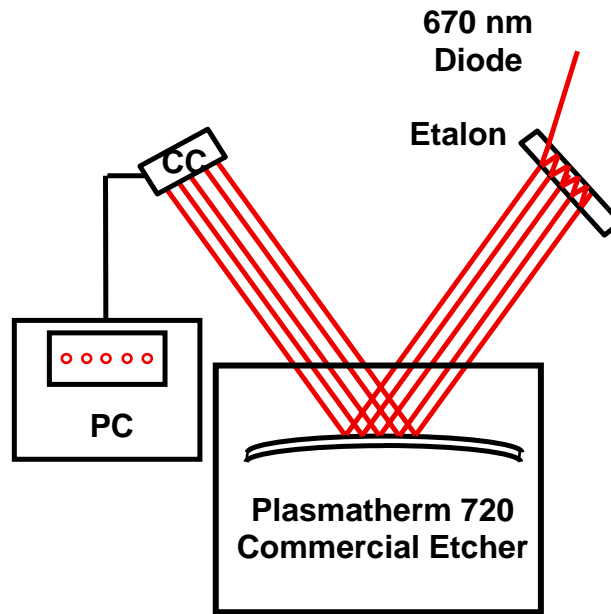
**Figure 1**. Schematic of the apparatus used to measure radius of curvature *in situ* during etch-back. The system is capable of measuring a change in radius of curvature of 5 km, corresponding to a stress change of ± 5 MPa for the 250 µm thick silicon substrates.
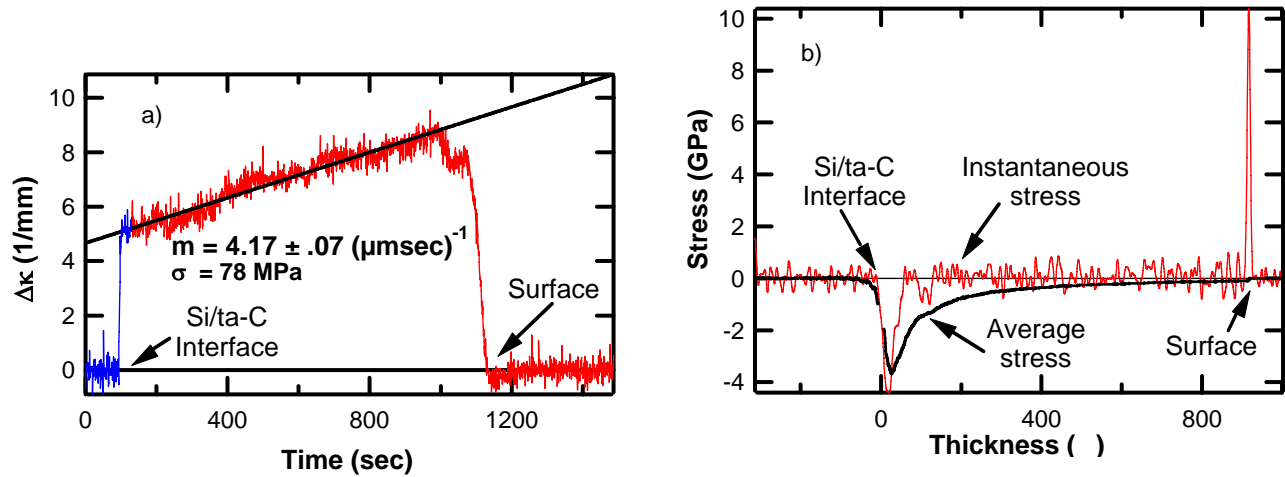


**Figures 2a & 2b.** Figure 2a shows change in curvature versus etch time for a sample with nominal zero-average stress as determined by conventional wafer curvature measurements. Note the large excursions both at the sample surface and ta-C/silicon boundary associated with interfacial stresses. The slope of the curvature change versus time corresponds to a bulk stress of 78 MPa tensile. In Fig. 2b the average and instantaneous stress derived from the curvature data in Fig. 2a are plotted versus sample thickness. Note the high surface stress (~10 GPa tensile) and the high interface stress (-4 GPa compressive).

# Theory of Strong Intrinsic Mixing of Magnetic Particle Suspensions in Vortex Magnetic Fields

### *by* **J. E. Martin**

**M**otivation—Although there are countless methods of fluid mixing, none of these has proven successful on the microscale. Even simple mixing cells have proven unsuccessful because it is difficult to create flow rates large enough to initiate turbulence. We have discovered that strong magnetic mixing occurs when magnetic particle suspensions are subjected to a "vortex" magnetic field - a rotating field in combination with a dc field normal to the rotating field plane, Fig. 1.

Experimental work in our laboratory shows that vortex field mixing has surprising properties. The mixing torque is *independent* of the field frequency and liquid viscosity, and proportional to the field squared. Mixing with a magnetic stir bar is quite different: the torque is proportional to the field frequency and liquid viscosity, and independent of the field strength. Of course, in each case there are stagnation conditions where mixing does not occur, such as an inadequate field, or a field frequency that is too high.

Our challenge is to develop a microscopic model of vortex field mixing that agrees with experimental observations, and predicts the dependence of the torque on particle size. If the torque is independent of the particle size, then a new technology can be scaled to any size.

**A**ccomplishment—From the details of our experimental observations we deduced that the mixing in vortex fields is due to the formation of particle chains that have a precessional motion. These chains are held together by the dipolar interactions between particles. The field creates a torque on a chain because it lags behind the field. A Brownian Dynamics code we developed confirms the existence of these chains.

Our theoretical analysis, summarized in Fig. 2, shows that the orbits of these chains lie on the surface of a cone. The chain cone angle $\theta$ is the vortex field angle for short chains, but becomes progressively smaller for longer chains, which lag the field by a greater phase angle $\phi$. If chains grow without limit, then eventually the cone angle will vanish, and mixing will not occur.

Whether or not this mixing catastrophe occurs is dependent on the vortex field angle. For vortex field angles greater than 45° chains cannot grow without limit because they become unstable or metastable. These instabilities, shown Fig. 2, are associated with the competition between the dipolar and hydrodynamic torque, as well as the fact that the radial dipolar interaction between enchained particles can become repulsive for large chain phase lags. We have confirmed these instabilities with single-chain simulations. The overall physical picture is one in which volatile chains grow to their stability limit, regardless of field frequency, strength, or liquid viscosity. This theory accounts for all of the experimental observations, and predicts that the mixing torque is independent of the particle size.

**S**ignificance—Mixing in a vortex magnetic field is a very simple and powerful method of mixing on the microscale, such as in irregular microfluidic devices. The mixing torque is independent of particle size, and the mixing is uniform throughout even complex volumes. This quantitative theory identifies the factors that optimize torque, and gives quantitative predictions for any given conditions.

**Contact:**   James E. Martin, Nanomaterials Sciences, Dept. 1112
Phone: (505) 844-9125, Fax: (505) 844-4045, E-mail: jmartin@sandia.gov
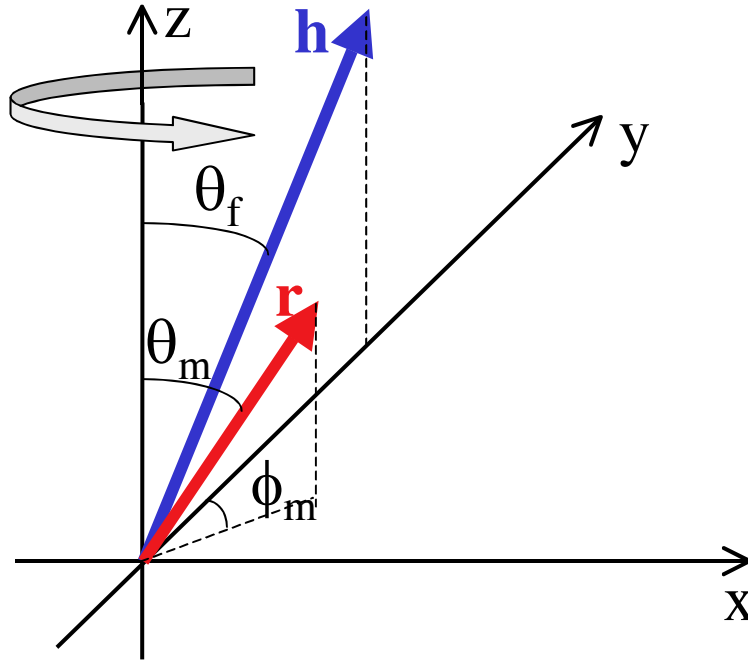
**Figure 1**. The field **h** rotates around the z axis at a vortex (or cone) angle $\theta_f$. The chain, indicated by the vector **r**, follows the field at some phase lag angle $\phi_m$, and at cone angle $\phi_m < \theta_f$.
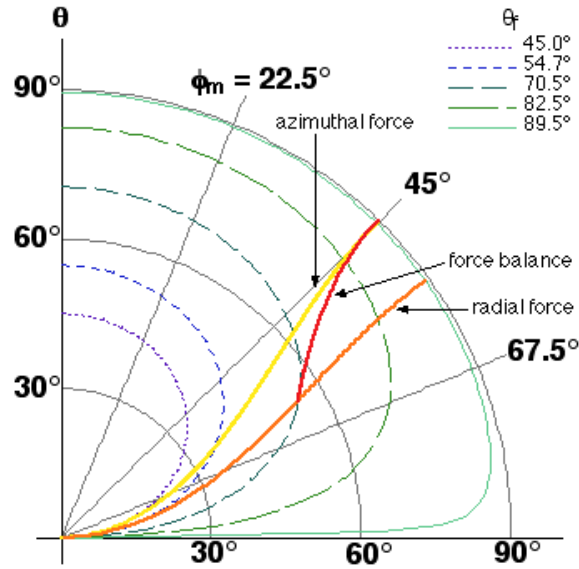


**Figure 2**. A polar plot of the stationary orbits of chains following a vortex field. (The radial distance is the polar angle $\theta$ and the phase lag $\phi_\mu$ is the standard polar azimuthal angle.) This polar plot has a direct physical interpretation: Each point on the locus of stationary orbits can be thought of as the point at which the chain vector intersects an x-y plane with z=1 at the instant at which the applied field is in the y-z plane. In yellow, orange and red are the various instabilities that can occur.

# Awards
# and Prizes

# Awards and Prizes

## National and International Awards

2005 — **American Academy of Arts and Sciences:** "For outstanding contributions in her profession." (Julia Phillips)

2004 — **National Academy of Engineering (NAE):** "For leadership and distinguished research in the epitaxy of dissimilar materials." (Julia Phillips)

## Other Awards

2008 — **American Physical Society (APS) George E. Pake Prize:** "For leadership and pioneering research in materials physics for industrial and national security applications." (Julia Phillips)
— **American Physical Society (APS) Aneesur Rahman Prize:** "For his ground-breaking development of computational methods and their application to the study of soft materials, including polymers, colloids, and granular systems." (Gary Grest)

2007 — **American Physical Society (APS) Division of Atomic and Molecular Physics (DAMOP) Fellow Appointment:** "For investigations of, and contributions to, the science of atomic and molecular processes in plasmas through development of innovative optical, microwave, and rf diagnostics." (Greg Hebner)
— **American Association for the Advancement of Science (AAAS) Fellow Appointment:** "For efforts on behalf of the advancement of science." (Julia Hsu)

2005 — **American Physical Society (APS) Fellow Appointment:** "For experiments advancing the understanding of electron correlation and electrodynamic response in oxide superconductors, ferromagnets, Coulomb glasses and nonlinear optical polymers." (Mark Lee)
— **Materials Research Society (MRS) "Science as Art" Competition First Prize Award:** "For Garden of ZnO Nano-Yuccas." (Julia Hsu, Tom Sounart, Neil Simmons, Jim Voigt, and Jun Liu)
— **R&D100 Award:** "For the development of Ion Photon Emission Microscope (IPEM)." (Barney L. Doyle, Michael Mellon, Floyd D. McDaniel, and Paolo Rossi)

2004 — **American Vacuum Society (AVS) Fellow Appointment:** "For developing innovative optical, microwave, and electrical diagnostics of plasma sources." (Greg Hebner)
— **Optical Society of America (OSA) Fellow Appointment:** "For contributions to the field of nonlinear optics." (Arlee V. Smith)
— **R&D100 Award**: "Cantilever Epitaxy and Growth of Low-Dislocation Gallium Nitride." (Inventors: C. I. H. Ashby, D. M. Follstaedt, C. C. Mitchell and J. Han; Developers: A. A. Allerman, K. H. A. Bogart, K. Cross, A. J. Fischer, K. Fullmer, L. Griego, D. D. Koleske, N. A. Missert, M. P. Moran, A. K. Norman, A. Ongstad, G. M. Peake, P. Provencio, and J. Sergeant)

— **Wilbur Lucius Cross Medal Recipient** – highest award of the Yale University Graduate School Alumni Association:  Cited for "scientific achievements, leadership in research management, outstanding service to the nation, and inspiration as a role model for young women in science and engineering."  (Julia Phillips)

## Sandia National Laboratories Awards

2007 — **Laboratory Directed Research & Development Award for Excellence:**  *"For Nanolithography Directed Materials Growth and Self-Assembly."*  (Julia Hsu)
— **Laboratory Directed Research & Development Award for Excellence:** *"For Microwave to Millimeter Wave Electrodynamic Response and RF Applications of Semiconductor Quantum Nanostructures."*  (Mark Lee)

2006 — **Laboratory Directed Research & Development Award for Excellence:**  *"Elucidating the Mysteries of Wetting."*  (Gary Grest)

## Patents Awarded

### 2007
— **Patent 7,248,397**
Title:  Wavelength-Doubling Optical Prametric Oscillator
Originators:  Darrell J. Armstrong and Arlee V. Smith
— **Patent 7,223,474**
Title:  Heteroporphyrin Nanotubes and Composites
Originators:  John A. Shelnutt, Craig J. Medforth, and Z. Wang

### 2006
— **Patent 7,148,974**
Title:  Method for Tracking the Location of Mobile Agents Using Stand-Off Detection Technique
Originators:  Susan F. A. Bender, Philip J. Hargis, Jr., Mark S. Johnson, Philip J. Rodacy, and Randal L. Schmitt
— **Patent 7,132,163**
Title:  Hereroporphyrin Nanotubes and Composites
Originators:  John A. Shelnutt, Craig J. Medforth, and Z. Wang
— **Patent 7,122,164**
Title:  Niobate-Based Octahedral Molecular Sieves
Originators:  Tina M. Nenoff and May D. Nyman
— **Patent 7,119,245**
Title:  Synthesis of an Un-supported, High-Flow ZSM-22 Zeolite Membrane
Originators:  Steven G. Thoma and Tina M. Nenoff

**— Patent 7,064,817**

Title: A Method to Determine and Adjust the Alignment of the Transmitter and Receiver Fields of View of a LIDAR

Originators: Philip J. Hargis, Jr., Tammy D. Henson, Leslie J. Krumel, and Randal L. Schmitt

**— Patent 7,041,616**

Title: Enhanced Selectivity of Zeolites by Controlled Carbon Deposition

Originators: Mutlu Kartin, Tina M. Nenoff, and Steven G. Thoma

## 2005

**— Patent 6,980,354**

Title: A Self-Seeding Ring Optical Parametric Oscillator

Originators: Darrell J. Armstrong and Arlee V. Smith

**— Patent 6,964,936**

Title: Method of Making Maximally Dispersed Heterogeneous Catalysts

Originator: Dwight R. Jennison

**— Patent 6,866,560**

Title: Method for Thinning Specimen

Originators: David M. Follstaedt and Michael P. Moran

**— Patent 6,844,378**

Title: Method of Using Triaxial Magnetic Fields for Making Particle Structures

Originators: James E. Martin, Robert Anderson, and Rodney Williamson

## 2004

**— Patent 6,790,476**

Title: Method of Adhesion Between an Oxide Layer and a Metal Layer

Originator: Dwight Jennison

**— Patent 6,775,314**

Title: Distributed Bragg Reflector Using AlGaN/GaN

Originators: Stephen Lee, Karen Waldrip, and Jung Han

**— Patent 6,775,054**

Title: Image Rotating 4-Mirror Ring Optical Parametric Oscillator

Originators: Arlee Smith and Darrell Armstrong

**— Patent 6,718,821**

Title: Laser Interferometry Force-Feedback Sensor for an Interfacial Force Microscope

Originators: Jack E. Houston and William L. Smith

**— Patent 6,716,275**

Title: Gas Impermeable Glaze for Sealing a Porous Ceramic Surface

Originators: Tina M. Nenoff, Scott T. Reed, Ronnie G. Stone, Steven G. Thoma, and Daniel E. Trudell

**— Patent 6,627,048**

Title: Laser Interferometry Force-Feedback Sensor for an Interfacial Force Microscope

Originators: Jack Houston and William L. Smith

# Advisory Boards and Professional Service

# Advisory Boards and Professional Service

## Department of Energy, Office of Basic Energy Sciences
— Solar Energy Program; Julia Hsu, panelist; 2007
— Council of the BES Division of Materials Sciences & Engineering; Julia Phillips, member; 2006-2008
— BES Advisory Committee Subcommittee on Grand Challenges in BES; Julia Phillips, member; 2006-2007
— Workshop on Basic Research Needs for Solid State Lighting:  Julia Phillips, Workshop Chair; Jerry Simmons, Panel Chair; Mary Crawford, Panel Member; 2006
— Scientific User Facilities Division Committee of Visitors; Julia Phillips, member; 2004
— Review of Nanoscience Research Center Operational Plans; Julia Phillips, member; 2004

## Los Alamos National Laboratory
— BES Materials Capability Site Review; Tina Nenoff, participant; 2007

## National Academy of Engineering
— Peer Committee, Materials Section:  Julia Phillips, member, 2007-2009; Chair, 2009
— U. S. Frontiers of Engineering Program:  Julia Phillips, Chair, 2005-2008; Mary Crawford, participant, 2005
— Draper Prize Committee; Julia Phillips, member; 2005-2007

## National Research Council
— Committee on Nanophotonics Assessability and Applicability; Jerry Simmons, member; 2006-2007
— Review Panel, National Research Council Associateship Program:  Diane Peebles, Neal Shinn, and Greg Hebner, members; 2006-2007
— Committee on Benchmarking the Research Competitiveness of US Chemical Engineering; Julia Phillips, member; 2006
— Committee to Assess the Impact of the MRSEC Program; Julia Phillips, BPA liaison; 2005-2006
— Board on Chemical Sciences & Technology; Bob Hwang, member; 2004-2007
— National Materials Advisory Board; Julia Phillips, Chair; 2002-2004
— Board on Physics and Astronomy; Julia Phillips, member; 2000-2006

## New Mexico State University
— New Mexico Nanoscience Education Initiative, Advisory Board; Neal Shinn, member; 2007
— Physics Advisory Board:  Neal Shinn, member, 2004-2007; Alan Wright, member, 2002-2004, 2006-2007

## Oak Ridge National Laboratory
— BES Chemical Sciences Site Review; Tina Nenoff, participant; 2007
— BES Site Review; Gary Kellogg, participant; 2006

## Texas State University
— Materials Science & Engineering Advisory Board; Carlos Gutierrez, member; 2006-2008

**Wessex Institute of Technology (UK)**
— Scientific Committee; Frank Van Swol, member; 2006-present

# Professional Societies/International Committees/Journals

**Air Force Office of Scientific Research (AFOSR)**
— Plasma-assisted Combustion AFOSR Review Panel; Greg Hebner and Paul Miller, members; 2004

**American Association for Crystal Growth**
— 20th American Conference on Crystal Growth and Epitaxy; Sean Hearne, Symposium Chair; 2006
— Executive Committee; Bob Biefeld, member; 2005-present

**American Association for the Advancement of Science (AAAS)**
— Council; Julia Phillips, member; 2003-2005
— Physics Section; Julia Phillips: Chair-elect, Chair, Past Chair; 2003-2005
— Physics Section Nominating Committee: Julia Phillips, member, 2003-2004; Chair, 2005

**American Chemical Society (ACS)**
— Committee on Science; Tina Nenoff, associate; 2007
— COLL Division; Tina Nenoff, councilor; 2006-2008

**American Physical Society (APS)**
— March Meeting Program Committee, Workshop on Energy for Young Physicists; Julia Hsu, member; 2008
— McGroddy Prize Committee; Julia Hsu, member; 2007-2008
— March Meeting Focused Session; Julia Hsu, organizer; 2007
— Division of Condensed Matter Physics (DCMP): Julia Phillips, Vice-Chair, 2005; Chair-Elect, 2006; Chair, 2007
— Forum on Industrial & Applied Physics (FIAP): Mark Lee, Vice-Chair, 2005; Chair-Elect, 2006; Chair, 2007
— Committee on Minorities; Carlos Gutierrez, Chair; 2006
— Bouchet Prize Committee; Carlos Gutierrez, member; 2005-2006
— Division of Materials Physics (DMP) Executive Committee; Julia Hsu, member-at-large; 2004-2006
— Symposium; Brian Swartzentruber, organizer; March 2004
— Committee on Meetings; Mark Lee, member; 2003-2006

**American Vacuum Society (AVS)**
— Neal Shinn, President; 2007
— 53rd International Symposium; Neal Shinn, Vice Chair; 2006
— Distinguished Lecture Series Committee; Neal Shinn, Chair; 2004-2006
— Board of Directors; Neal Shinn, member; 2003-2006

**ASM International - The Materials Information Society**
— Events Committee; Dan Barton, member; 2003-present

## Professional Societies/International Committees/Journals Cont'd

— Electronic Device Failure Analysis Society (EDFAS):  Dan Barton, Board of Directors member, 1998-present; Vice-President, 2005

**Chemistry of Materials**
— Editorial Board; Tina Nenoff, member; 2006-2009

**Conference on Magnetism and Magnetic Materials**
— Scientific Advisory Board; Carlos Gutierrez, member; 2005-2007

**Electrochemical Society**
— Symposium;  Nancy Missert, organizer; 2006
— Corrosion Division, Nancy Missert:  Student Travel Grant Coordinator, 2005-2008; executive committee member and member-at-large, 2006-2008
— Nash Miller Award Committee; Nancy Missert, member; 2005
— Individual Membership Committee; Nancy Missert, member; 2003-2006

**Fifteenth International Conference on Crystal Growth**
— Bob Biefeld, Program Co-Chair; 2006-2007

**Gaseous Electronics Conference (GEC)**
— 56th Annual Meeting; Greg Hebner:  Chair-elect, Chair, Past Chair; 2003-2006

**Gordon Conference**
— Zeolite Gordon Conference; Tina Nenoff, Vice-Chair; 2008

**Institute of Electrical and Electronics Engineers (IEEE)**
— *Transactions on Plasma Science*, 4th issue on Images in Plasma Science; Greg Hebner, guest editor; 2004-2005
— *Transactions on Device and Materials Reliability (TDMR)*; Dan Barton, guest editor; 2002-present
— International Reliability Physics Symposium, Management Committee; Dan Barton, member; 2001-present

**International Conference on Applications of Accelerators in Research and Industry**
— Barney L. Doyle, Chairman; 2004, 2006

**International Conference on Defects in Semiconductors**
— International Advisory Board, Alan Wright:  Co-organizer, 2005-2007; Co-Chair, 2007

**International Conference on Low Energy Electron Microscopy/Photoemission Electron Microscopy (LEEM/PEEM)**
— International Advisory Committee; Gary L. Kellogg, member; 2000-present

**International Conference on Nuclear Microscopy Technology and Applications**
— International Committee, Barney L. Doyle; 1990-2004

## Professional Societies/International Committees/Journals Cont'd

**International Conference on Particle-Induced X-Ray Emission and its Analytical Applications**
— International Committee; Barney L. Doyle, member; 2005

**International Conference (4th) on Porphyrins and Phthalocyanines (ICPP)**
— Symposium; John Shelnutt, organizer and Chair; 2004, 2006, 2008

**International Electron Devices Meeting**
— Session; Tom Friedmann, organizer; 2007

**International Journal of PIXE (IJPIXE)**
— Editorial Board, Barney Doyle; 1996-present

**International Union for Vacuum Science, Technique, and Applications (IUVSTA)**
— 17th International Vacuum Congress; Neal Shinn, Program Committee member; 2007
— 16th International Vacuum Congress; Neal Shinn, Program Committee member; 2004
— Surface Science Electoral College; Neal Shinn, United States Representative; 2001-2007
— Surface Science Division:  Neal Shinn, Chair, 2004-2007; secretary, 2001-2004

**International Zeolite Association (IZA)**
— Commission on Synthesis Committee; Tina Nenoff, member; 2004-2007

**Journal of Chemical Physics**
— Editorial Board; Jim Martin, member; 2003-2006

**Journal of Crystal Growth**
— *Journal of Crystal Growth* for subject areas:  "Epitaxial Growth and Nanostructures"; Bob Biefeld, Associate Editor; 2004-present

**Journal of Materials Research**
— Editorial Advisory Board; Julia Phillips, member; 2004-present

**Materials Research Society (MRS)**
— Surface Electron Microscopy Symposium; Gary Kellogg, lead organizer; Spring 2008
— Information Services Committee; Sean Hearne, Chair; 2007
— Operational Oversight Committee; Julia Hsu, treasurer and member; 2006-2007
— *MRS Bulletin*:  H2 Production; Tina Nenoff, co-editor; October 2006
— Symposium:  Neal Shinn and John Sullivan, organizers, Spring 2006; Barney Doyle, Organizer, Fall 2005; Julia Hsu, lead organizer, Fall 2007
— Board of Directors; Julia Hsu, member; 2005-2007
— Technical Program Committee; Julia Phillips, Chair; 2005-present
— Web Advisory Sub-Committee:  Sean Hearne, member, 2005-2006; Chair, 2006
— Electronic Services Task Force; Sean Hearne, member; 2005
— Membership Committee; Sean Hearne, member; 2004-present
— Meetings; Julia Hsu, Chair; Fall 2004

## Professional Societies/International Committees/Journals Cont'd

— Public Affairs Committee/Women in Materials Science and Engineering; Tina Nenoff, member and semi-annual organizer; 2001-2004

**Microelectronics Reliability (Elsevier Journal)**
— Editorial Advisory Board; Dan Barton, member; 2000-present

**Nanotechnology**
— Editorial Advisory Board; John Shelnutt, member; 2005-2007

**Nuclear Instruments and Methods in Physics Research, Section B: Beam Interactions with Materials and Atoms**
— Editorial Board; Barney Doyle, member; 2003-2006

**Pacifichem (Honolulu)**
— Symposium; John Shelnutt, organizer and Chair; 2005

**Physical Review E**
— Gary Grest, senior editor; 2002-present

**Solid State Communications**
— Julia Hsu, Editorial Board; 2005-present

**The Minerals, Metals, and Materials Society (TMS)**
— Electronic Materials Conference:  Nanoscale Characterization, Zinc Oxide, and Organic/Hybrid Photovoltaics Symposium; Julia Hsu, organizer; 2007
— Electronic Materials Committee:  Bob Biefeld, member, 2002-present; secretary, 2002-2004; Vice Chair, 2005-2007; Chair, 2007-2009; Past Chair, 2009-2011; Julia Hsu, member, 2000-2006
— Symposium; Sean Hearne, organizer; March 2004

**Thirteenth US-Organometallic Vapor Phase Epitaxy Workshop**
— Organizing Committee; Bob Biefeld, member; 1991-present

# Resources and Capabilities

## Resources and Capabilities
## Physical, Chemical, and Nano Sciences Center

**— Diagnostics and Characterization —**

### Atomic-Level Imaging and Spectroscopy

We have developed technical capabilities in the following areas:

- Atomic Force Microscopy (AFM) for imaging, force profiling, electrical measurements, and manipulation of individual biomolecules in fluid environments with simultaneous fluorescence detection.
- Atom Probe Microscopy (APM) with pulsed laser desorption capability.
- Interfacial Force Microscopy (IFM), with ultra-sensitive laser-interferometer deflection sensing and capacitive electrostatic force feedback, which represents the first scanning probe technique available with quantitative and independent 2D force sensing. This capability allows detailed studies at the nano-meter level of adhesion, friction, and mechanical properties. The force-feedback feature enables the IFM sensor to be non-compliant, eliminating the serious "snap to contact" problems found in all present interfacial-force techniques (e.g., the AFM and the Surface Forces Apparatus).
- Piezoelectric force microscopy (PFM) for measuring spatial variation in piezoelectric properties, determining the piezoelectric coefficient and piezoelectric crystal orientation, and for imaging ferroelectric domains with lateral resolution in the range of tens of nanometers. The high-resolution PFM is also useful for inferring the crystal orientation on the surface of nanostructured piezoelectric materials.
- Scanning Tunneling Microscopy (STM) capabilities with the ability to track the diffusion of single atoms on surfaces.
- Nanomanipulator in a SEM for imaging and characterization of individual nanostructures.
- Low Energy Electron Microscopy (LEEM) with nanometer spatial resolution and real-time spectroscopic imaging capability at sample temperatures from 125K to over 1750K, with UHV access to joint Scanning Tunneling Microscopy (STM) capability.
- Field Ion Microscopy (FIM) with single atom resolution and accurate temperature control to 1 Kelvin.

### Center for Integrated Nanotechnologies (CINT)

The Center for Integrated Nanotechnologies (CINT) is a Department of Energy/Office of Science Nanoscale Science Research Center (NSRC) operating as a national user facility devoted to establishing the scientific principles that govern the design, performance, and integration of nanoscale materials. CINT is a partnership of Sandia and Los Alamos National Laboratories.

CINT is one of five NSRCs throughout the U.S. that form an integrated national program, affiliated with major facilities at the DOE's National Laboratories, to cover the diverse aspects of nanoscience and technology. This complex aspires to become a cornerstone of the nation's nanotechnology revolution, contributing to DOE's principal missions in national defense, energy, and the environment while providing an invaluable resource for universities and industries.

Through its core facility in Albuquerque with gateways to both Los Alamos and Sandia national laboratories, CINT provides open access to tools and expertise needed to explore the continuum from scientific discovery to the integration of nanostructures into the micro- and macro world. (Additional information is available at: http://cint.lanl.gov/

### Chemical Vapor Deposition (CVD)

Our experimental tools for investigating CVD

include optical probes (such as reflectance-difference spectroscopy and emissivity correcting pyrometry) for gas-phase and surface processes, a range of surface analytic techniques, molecular beam methods for gas/surface kinetics, and flow visualization techniques. These tools are integrated in a unique manner with research CVD reactors and with advanced chemistry and fluid models.

## Electrochemical Scanning Probe Microscopy

We have developed the ability to study nanoscale changes at surfaces during oxidation and dissolution of metal surfaces under electrochemical control using scanning tunneling microscopy and atomic force microscopy. These studies can be performed in a variety of electrolytes in order to determine the mechanisms governing passive film growth and dissolution.

## Inorganic Porous Materials Characterization Laboratory

Laboratory characterization capability relevant for inorganic porous materials relevant for catalysis, separations and energy research is available. Structural studies are performed with a $\theta\text{-}2\theta$ powder x-ray diffractometer with ICDD-PDF database search capability. Additional complementary characterization capabilities include a BET (Brunauer-Emmett-Teller) measurement system (Quantachrome Autosorb 6B), TGA/DTA system (TA Instruments SDT 2960), a transmittance and reflectance FTIR spectrometer (Perkin Elmer Spectrum GX), an atomic absorption spectrometer (Perkin Elmer 5100PC), a chemisorption analyzer (Micromeritics AutoChem II 2920), and a Temperature Programmed Desorption (TPD) unit (Quantachrome ChemBET 3000 TPR/TPD). Additionally, computer software needed to support this research is available. This includes the REACT and EQ#/6 codes for reaction path and solution equilibria calculations. Also available are FITEQL (the state of the art code for fitting surface chemical titra-

tions) and HYDRAQL (a surface speciation code).

## Interfacial Force Microscopy Materials and Microsystems Metrology

We have developed a unique wide-field scanning Interfacial Force Microscope (IFM) with calibrated force detection for the independent dynamic measurement of normal and lateral forces of micro-electrical-mechanical system (MEMS) components in operation. The IFM's force-feedback detection feature enables the IFM sensor to be non-compliant, eliminating the serious "snap to contact" problems found in all other present scanning probe and interfacial force techniques (e.g., the AFM and the Surface Forces Apparatus). IFM measurements permit studies of static and dynamic friction behavior, contact compliance, and wear. In addition, it is capable of independent normal and lateral force versus displacement measurements of microsystem components. The IFM has been recently upgraded with an enhanced sensitivity laser interferometer-based sensor (US Patent No. 6,085,581), Field-Programmable Hybrid Instrumentation, and an improved user-friendly software interface.

## Ion Beam Analysis

Two accelerator facilities in the Center are used for quantitative high-energy ion beam analysis of materials. These are the 2.5 MV Van de Graaff and the 6.5 MV Tandem Pelletron. Light elements (hydrogen to fluorine) are depth concentration profiled using heavy ion elastic recoil detection (ERD) and nuclear reaction analysis (NRA), while heavier elements are measured using backscattering spectrometry (e.g. RBS) and proton induced x-ray emission (PIXE). An external Micro Ion Beam Analysis (X-MIBA) capability enables multi-elemental analysis and ion irradiation of samples, which are vacuum incompatible or extraordinarily large and are currently a main component of the Center's Homeland Security program where it is being used to detect radioactive particulates and

measure compositional signatures. The Nuclear Microprobe is used to study materials with 1 micron lateral resolution.

## KMAP X-ray Diffractometer

Based on double crystal x-ray diffractometry in combination with position sensitive x-ray detection, our KMAP x-ray diffraction analysis is used to determine the lattice constant, strain relaxation, composition, layer orientation, and mosaic spread for a large variety of advanced epitaxial semiconductor material systems.

## Lasers and Optics

We provide characterization and advanced understanding in the area of solid-state lasers and non-linear optics, especially as coherent sources of broadly tunable light in rugged, compact geometries. We also have established expertise in long-term and transient radiation effects characterization of optical materials. Capabilities include the widely used (approximately 2000 users worldwide) SNLO (Sandia Non-Linear Optics) code, which is a lab-tested code for predicting the performance of non-linear optical components. In the area of integrated optical materials, our laboratories produce new types of photosensitive materials (processing patent applied for) for directly-writeable waveguides and reconfigurable optical interconnects.

## Low-Temperature Plasma Analysis

We have state-of-the-art capabilities for the analysis of low-temperature plasmas as found in commercial processing reactors. These include emission spectroscopy, electrical characterization, laser and microwave-based measurements of species concentrations, *in situ* electric field measurements, and others. Sandia is the only lab that combines new diagnostics, relevant process chemistries (complex mixtures), and massively parallel (MP) computer models for simulation of continuous and transient plasmas.

## Magnetic Characterization

We can characterize the static and dynamic (0.001 Hz - 1 kHz) magnetic response of mate-

rials using a Superconducting Quantum Interference Device (SQUID) Magnetometer. Our Magnetic Property Measurement System (MPMS) from Quantum Design is capable of producing fields from 0 - 7 T and can vary the temperature of the sample chamber from 1.9 - 400K, detecting signals as low as $1 \times 10^{-7}$ emu. The MPMS is also suitable for determining the critical current density ($J_c$) of superconducting materials).

## Materials Microcharacterization

Our capabilities in this area include optical microscopy, scanning, electron microscopy, analytical transmission electron microscopy, double crystal x-ray diffraction, ion beam analysis of materials (RBS, channeling, ERD, PIXE, NRA), Hall measurements, microcalorimetry, photoluminescence, light scattering, electronic transport, deep level spectroscopy, magnetization, and dielectric and magnetic susceptibilities.

## MEMS-based Tensile Testing

We have developed the capability to perform pure uni-axial loading of metal MEMBS test structure *in situ* and *ex situ* of a TEM. The technique has been demonstrated using Al, Ni and Cu, but is applicable to a wide range of other materials.

## MESA

Sandia's compound semiconductor clean room operations and associated characterization laboratories moved into new facilities in 2006 and 2007. These facilities are part of the new $450 million MESA (Microsystems and Engineering Sciences Applications) complex. The MESA project included a budget for upgrading equipment as well as new facilities and new, enhanced capabilities. This complex is completed and now enables a quick turnaround for innovative compound semiconductor device prototypes at Sandia. The arrangement of this facility is meant to encourage collaboration among diverse organizations to enable a more efficient working environment.

## Nanoelectronics Laboratory

We have the capabilities for fabrication of nanoscale quantum device structures, together with capabilities for ultra-low-noise measurement of transport from 25 m Kelvin to ambient at high magnetic fields.

## Optical Spectroscopy

Our capabilities in characterizing semiconductor materials by photoluminescence and magnetoluminescence extend down to low temperatures by optical laser imaging and laser microscopy, by laser excitation spectroscopy, and by the time-resolved measurements of optical emission. We also have developed a high lateral resolution, near-field scanning optical microscopy (NSOM) capability with time and frequency resolution.

## Photovoltaic Device Characterization Laboratory

We have developed characterization capabilities in support of prototyping photovoltaic research. Capabilities include spectrally resolved photocurrent and photocapacitance measurements and a solar simulator for device characterization.

## Radiation Effects Microscopy

We have facilities for nuclear microscopy and radiation effects microscopy based on a 6.5 MV tandem Pelletron ion accelerator and 1.9 MeV/amu Radio Frequency Quadrupole LINAC Booster. We generate ion species from hydrogen to gold for radiation effects research. The Sandia Nuclear Microprobe with micrometer size high-energy ion beams is used to microscopically study radiation effects in devices ranging from discrete transistors to state-of-the-art integrated circuits. Three advanced diagnostic techniques were invented at Sandia: Single-Event-Upset Imaging, Ion-Beam-Induced-Charge-Collection Imaging (IBICC), and time-resolved IBICC. A recent development is the Ion Electron and Ion Photon Emission Microscopes (2001 and 2005 R & D-100 Award winners), which can perform radiation microscopy using very highly ionizing particles without focusing the ion beam. Most recently we have developed a dedicated endstation to expose discrete transistors to intense pulses of high energy heavy ions (e.g., 40 MeV Si ions) to simulate and study neutron damage effects using *in situ* Deep Level Transient Spectroscopy (DLTS).

## Scanning Cathodoluminescence Microscopy

We have developed the ability to measure and image cathodoluminescence from insulators and semiconductors on the submicron scale in order to understand how defects influence the emission of light from the ultraviolet to the visible. Individual spectra are also obtained at controlled locations in order to identify heterogeneities. A new system is now operational in the MESA Microfab, allowing spectral imaging at high resolution using a field emission SEM.

## Simultaneous Measurement of H, D, and T in Materials

We have designed and implemented a new ion beam analysis (IBA) system to simultaneously measure the absolute quantities of H, D, and T in materials using an elastic recoil detection (ERD) technique. The technique uses an E-dE detector arrangement, or particle telescope, to provide for accurate separation of the H, D, and T signals. The system can also simultaneously acquire information about medium and high -Z elements in the sample using Rutherford backscattering spectrometry (RBS). Measurement of other light elements is possible using the nuclear reaction analysis (NRA) technique, which is isotope specific. The system will have an accuracy of $< 2\%$ for measuring the composition of solids.

## — Synthesis and Processing —

### 400 keV and 300 keV Ion Implanters

These systems are equipped with a variety of sources (gas, sputter, and metal vapor). This facility provides ion species from hydrogen to bismuth that can be used for studying fundamental irradiation mechanisms and selective chemical doping in semiconductors, metals, ferroelectrics, and superconductors. The 300 keV implanter is capable of both ambient and high temperature implants up to 600°C and ion currents up to 50 micro-A.

### Crystal and Thin Film Growth

Capabilities in this area include pulsed laser deposition chambers, a high vacuum metal deposition chamber, a thin film oxide deposition chamber, a diamond-like carbon deposition chamber, a hot filament chemical vapor deposition chamber, microwave plasma deposition of diamond chamber, and various apparatus for single crystal growth. Our capabilities for stress relief of diamond-like carbon films and structures produced by pulsed laser deposition are not available elsewhere.

### Metal-Organic Chemical Vapor Deposition (MOCVD)

We maintain research facilities with capabilities in MOCVD of III-V compound semiconductor materials including GaN-based materials and self-assembled quantum dots. These capabilities include research reactors designed specifically for studies of CVD chemistry, fluid dynamics, the development of advanced in situ diagnostics, and the development of advanced semiconductor heterostructures and devices.

### Soft Nanolithography

Soft nanolithography refers to patterning techniques that complement UV and electron beam lithography. These approaches avoid the chemical and radiation exposure often used in conventional lithography processing, making soft nanolithography particularly useful for bio, organic, and molecular materials. Current capabilities include micro-contact printing, nano-transfer printing, and dip-pen nanolithography.

### Stress Evolution During Electrodeposition

We have developed the capability to measure stress evolution during thin film electrodeposition and have used it to measure stress during patterned and unpatterned film growth. Our studies range from fundamental mechanisms that create stress during island coalescence to materials-specific systems, such as electrodeposited Ni, Cu, Sn, Ag, and their alloys.

### Stress Evolution During Etching

We have developed a capability to measure stress evolution during etching of thin films in a commercial etch tool. We have used this capability to measure through thickness stress profiles in thin films. This information is particularly useful for characterization of materials for microelectromechanical systems as nonlinear and interfacial stresses can cause unwanted out-of-plane bending in released devices.

### Synthetic Organic Laboratory

Novel surfactants and other small molecules are prepared in this laboratory via synthetic organic techniques. The laboratory is also capable of forming and characterizing self-organized structures (e.g., micelles and self-assembled monolayers) generated with the newly synthesized molecules in pure or mixed molecular systems.

## — Theory and Simulation —

### Ab-Initio Molecular Dynamics (AIMD)

We have custom-modified versions of existing AIMD codes that have been used to perform some of the largest scale free energy calculations of chemical reactions in the aqueous phase and in water-filled nanopores.

### Chemical Processes

We have extensive capabilities, including massively-parallel computation, to model complex chemically reacting flows such as occur in chemical vapor deposition manufacturing processes. Our numerical simulations

can include the coupled gas-phase and gas-surface chemistry, fluid dynamics, heat, and mass transfer to provide predictive models of a chemical process.

## Low-Temperature Plasmas

We have extensive  capabilities in massively parallel codes to simulate the time and space evolution of low-temperature plasmas, focusing on new theoretical techniques for achieving rapid convergence and on direct comparisons with experimental results.

## Molecular Dynamics Simulation

Large scale, classical molecular dynamics simulations using the massively-parallel code LAMMPS (Large-scale Atomic/Molecular Massively Parallel Simulator) are being used to model a wide variety of systems. These classical simulations cover the length and time scale intermediate between quantum and continuum calculations. Systems of current interest include adhesion and friction in self-assembled monolayers, nanoparticle flow,  ordering and self assembly, granular materials and transport in polymer membranes for fuel cells. Recent modifications of LAMMPS include the introduction of non-equilibrium molecular dynamics (NEMD) capability to determine the shear viscosity as a function of shear rate and colloid pair interactions to model nanoparticle suspensions.  We have also custom-modified versions of existing Ab-Initio Molecular Dynamics (AIMD) codes that have been used to perform large scale free energy calculations of chemical reactions in the aqueous phase and in water-filled nanopores.

## Monte Carlo Simulations

We have classical force field-based Monte Carlo capabilities for atomistic simulations that predict phase equilibria and the permeation of molecular species into nanopores.

## Optical and Wave Propagation

We have developed advanced simulation codes for understanding wave propagation in optical parametric oscillators and amplifiers for the purpose of designing highly efficient, tunable laser sources.  We also have capabilities in novel optical designs, including resonators for compact laser geometries.  These capabilities are coupled to in-house micro-optics construction facilities and state-of-the-art optics testing.
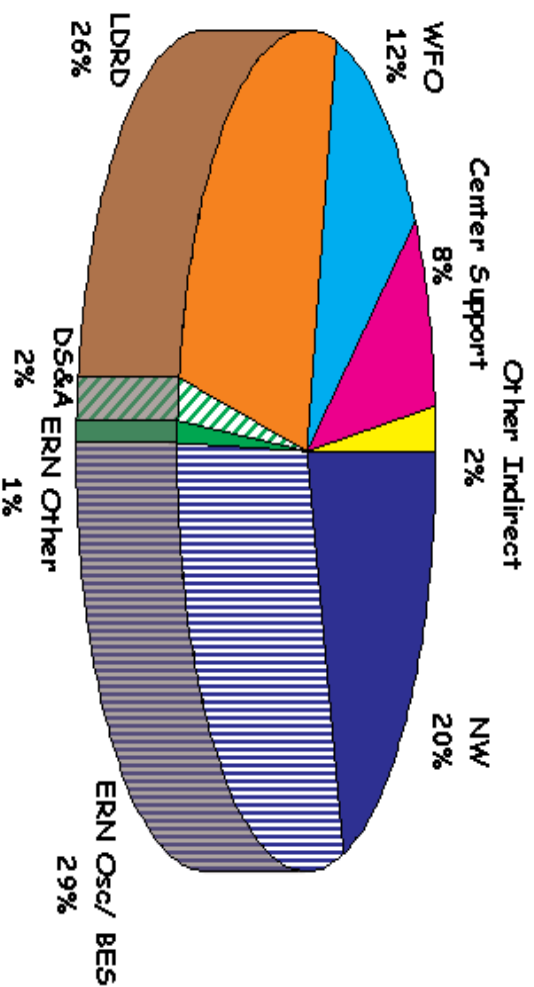
## Quantum Mechanics

We have developed a state-of-the-art massively parallel quantum mechanics density-functional-theory code that utilizes a plane wave basis set and either norm-conserving pseudopotentials or projector-augmented wave functions. These codes are used to develop fundamental understanding of physical phenomena and atomic processes in materials. Specific areas of interest include point defects and impurities in silicon and compound semiconductors, adsorbate interactions on surfaces, bonding at metal-oxide interfaces, and enhanced reactivity of nanoparticles. Recent advances include implementation of exact exchange via an optimized effective potential that is determined iteratively within density-functional theory. Other areas of interest for more general density-functional-theory applications include adsorbate interactions on surfaces, bonding at metal-oxide interfaces, and enhanced reactivity of nanoparticles.
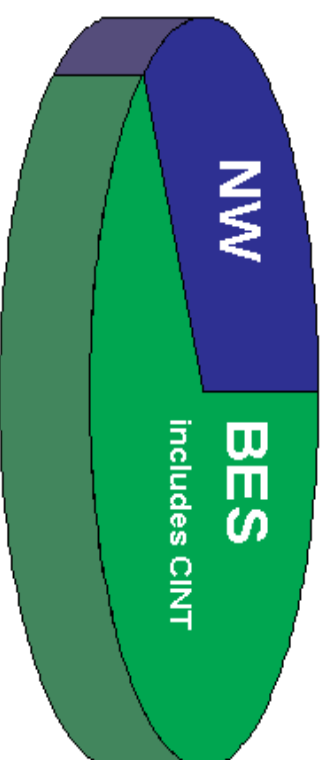
# Physical, Chemical, and Nano Sciences Center - FY07 Budget

# Physical, Chemical and Nano Sciences Center
## FY07 Budget - by Customer

## Operating ($45.9M)

WFO
12%

Center Support
8%

Other Indirect
2%

NW
20%

ERN Osc/ BES
29%

ERN Other
1%

DS&A
2%

LDRD
26%

## Capital ($2.2M)

NW

BES
includes CINT

| | | | |
|---|---|---|---|
| NW | Nuclear Weapons | ERN | Energy, Resources & Nonproliferation | DS&A | Defense Systems & Assessments | WFO | Work for Others |
| | | OSc/BES | Office of Science/Basic Energy Sciences | LDRD | Laboratory Directed Research & Development | | |